UCLouvain
Institute for Information
and Communication Technologies,
Electronics and Applied Mathematics

Design and characterization of SERS substrates based on porous silicon membranes infiltrated with gold nanoparticles

Clémentine GEVERS

Thesis submitted in partial fulfillment
of the requirements for the degree of
Doctor in Applied Sciences

Dissertation committee:

Prof. Laurent FRANCIS (UCLouvain, Supervisor)
Prof. Benoît MACQ (UCLouvain, Chair)
Prof. Denis FLANDRE (UCLouvain, secretary)
Prof. Sophie HERMANS (UCLouvain)
Prof. Luc HENRARD (UNamur, Belgium)
Prof. Michael SAILOR (UCSD, USA)

October 2026

When the Lord closes a door, somewhere He opens a window - The sound of music

Abstract

ANTIMICROBIAL resistance (AMR) is increasingly recognized as one of the major global health threats of the 21st century. According to the World Health Organization, new resistance mechanisms are continuously emerging and spreading worldwide, compromising the treatment of common infectious diseases and leading to prolonged illness, disability, and death. The rapid development of resistant pathogens is strongly accelerated by the misuse and overuse of antibiotics, which are often linked to the absence of rapid and reliable diagnostic tools. In clinical practice, the lack of fast pathogen identification frequently leads to the empirical administration of broad-spectrum antibiotics as an immediate response to infection, further contributing to the spread of AMR.
To address this challenge, significant research efforts are currently focused on the development of rapid, sensitive, and selective biosensing platforms for pathogen detection. Within this context, porous silicon (PSi)-based optical biosensors have emerged as promising candidates due to their large specific surface area, tunable morphology, and compatibility with microfluidic integration. Previous work conducted in our laboratory demonstrated that the implementation of a membrane-based flow-through configuration significantly improves bacterial capture within the porous structure, enabling a limit of detection of 10^3 CFU/mL. However, even lower detection limits are required for practical clinical applications, where bacterial concentrations may fall below 100 CFU/mL, for example in cases of sepsis or virulent urinary tract infections.

One promising strategy to further improve sensitivity is to replace the reflectometric readout with Surface-Enhanced Raman Scattering (SERS)-based detection. By decorating the porous silicon matrix with plasmonic nanoparticles, highly localized electromagnetic "hotspots" can be generated, leading to a strong amplification of the Raman signal.

The objective of this thesis is therefore to design and study a porous silicon-based SERS substrate as a proof of concept. Rather than focusing solely on achieving record sensing performances, this work aims at better understanding the relationship between porous silicon morphology and the SERS response, and to identify the key design parameters governing both sensitivity and signal reproducibility.

To achieve this objective, several contributions are developed throughout this work. In Chapter 1, numerical simulations are combined with an analytical model in order to calculate the SERS enhancement factor in liquid suspensions. While the original analytical model is limited to spheroidal nanoparticles, the proposed approach enabled the investigation of more complex geometries and allows direct comparison with experimental measurements.
In Chapter 2, a new fabrication strategy for freestanding porous silicon membranes is proposed, enabling a rapid and simple process adaptable to a wide variety of porous structures. The membrane release is achieved through a short electropolishing step optimized using numerical simulations, leading to mechanically stable membranes compatible with microfluidic integration and nanoparticle decoration.
In Chapter 3, a versatile decoration method is developed by flowing colloidal suspensions of plasmonic nanoparticles through the porous membranes inside a microfluidic setup. This approach enables homogeneous decoration throughout the entire membrane thickness without clogging the pores and is successfully demonstrated for several porous architectures. The influence of the porous substrate on the SERS response is then investigated, highlighting the combined role of porous silicon morphology, optical properties, and nanoparticle loading on the Raman enhancement.
Overall, this work provides a better understanding of the interplay between plasmonic nanoparticles and porous silicon structures, and proposes valuable design guidelines for the development of efficient and reproducible porous silicon-based SERS substrates.
This work is further strengthened by the collaboration with Louise Lejeune, whose expertise in the synthesis of plasmonic nanoparticles with controlled shapes and sizes provided valuable experimental support throughout this research.

Acknowledgements

Je tiens d'abord à remercier mon promoteur, **Laurent A. Francis**, pour sa vision de ce projet, parfois plus claire que la mienne. Merci pour la confiance que tu m'as accordée, pour la grande liberté de recherche, et pour ta disponibilité, même pour les relectures de dernière minute.
Un grand merci au Pr. **Sophie Hermans**, qui a toujours cru en cette recherche et su nous remotiver quand il le fallait. Vos mots justes et vos conseils ont été précieux pour nous guider et trouver de l'aide au bon moment.
I would like to thank Pr. **Mike Sailor** for the opportunity to attend your Summer School in San Diego. That's where we acquired the fundamentals of our research. Thank you for your warm welcome, for this wonderful adventure, and for your wise advice.
Je remercie également le Pr. **Denis Flandre** et le Pr. **Luc Henrard** pour leur guidance et pour m'avoir aidé à développer une rigueur scientifique. Denis, merci de m'avoir accueillie dans ton groupe de recherche, me permettant de partager mes avancées avec les collègues les plus proches.
Merci au président de mon jury, le Pr. **Benoît Macq**, pour son enthousiasme pour ma recherche et pour l'organisation de ma défense.
Merci aussi au Pr. **Annika Gillis** pour sa collaboration, sa confiance en notre travail, et pour nous avoir ouvert les portes de son laboratoire de biologie.
Je remercie le FNRS pour la bourse FRIA, qui a financé ma recherche pendant quatre ans.

Après les professeurs, il y a une personne sans qui ce projet n'aurait jamais abouti: **Louise Lejeune**. Merci pour ta présence, ton aide, et pour ces deux mois à San Diego qui ont consolidé notre recherche. Merci pour toutes ces heures de travail, de doute, d'espoir, de désespoir, et de rigolade. Merci pour nos petites réunions et nos messages qui nous ont motivées l'une l'autre. Un immense merci, et j'espère que nous continuerons à nous

soutenir, même si nos chemins se séparent.

Merci à **Pascal Simon** et **Valeriya Kilchytska** pour leur gestion de WELCOME et leur soutien précieux, ainsi qu'à **Benoît Hubert** et **Souley Djadjandi** pour leur aide au quotidien.
Un grand merci à toute l'équipe de Winfab, sans qui cette recherche n'aurait pas été possible: **Christian Renaux**, **Sébastien Faniel**, **Miloud Sitout** et **Nicolas André**. Merci aussi pour nos discussions toujours sympathiques à la cafétéria. Merci au personnel administratif, qui a rendu mon travail plus serein malgré la complexité des démarches de l'UCL et du FNRS. Un merci particulier à **Anne Gillet**, **Isabelle Dargent**, **Florence Van Dievoet**, **François Hubin**, **Émilie Brichart**, **Christel Derzelle**, **Brigitte Dupont** et **Rémi Dekimpe**. Je me souviendrai aussi de nos moments de rigolade à la cafétéria.

Merci à tous mes collègues qui ont égayé mes journées : **Ottilie**, **Tom**, **Eléonore**, **Antoine**, **Clara**, **Martin**, **Margo**, **Ramy**, **Justine**, **Nicolas**, **Jeremy**, **Manon**, **Cécile**. Merci pour tous les moments de discussion et de rire partagés.
Merci à ceux qui sont déjà docteurs et qui m'ont aidée à me former et à trouver ma place, notamment **Nicolas R.**, **Nicolas M.**, **Romain S**. et **Karim**.
Merci à **Elia Colomer Clavel** pour ton enthousiasme quotidien pendant ton stage. J'ai eu la chance de t'encadrer, et grâce à ta motivation, nous avons bien avancé dans notre recherche.
Merci à **Noémie**, qui m'a accueillie dans son bureau et avec qui j'ai pu discuter de nombreuses heures. Merci pour ton engagement, qui a su me motiver.
Merci à **Rose**. Sans toi, ces quatre ans n'auraient pas existés. J'ai toujours trouvé aide et conseils auprès de toi, même après ton départ. Je te suis grandement reconnaissante et sais que je pourrai toujours compter sur tes précieuses recommandations.

Merci à **Loïc**, **Brieuc** et **Anne-So**. Je ne sais pas comment résumer en quelques phrases tout ce que vous m'avez apporté, mais sans vous ces 4 années auraient été bien moins colorées. Merci de m'avoir fait sortir de ma zone de confort en organisant faire toutes nos sorties plus uniques les unes que les autres. Sachez que nos étoiles brilleront à jamais.

Merci à tous mes amis pour votre motivation et votre intérêt pour mon

travail. J'espère que ma défense publique vous éclairera un peu plus sur ce que j'ai pu faire. Merci aussi à la chorale BBR de m'avoir changé les idées. Enfin, merci à ma famille pour tout son encouragement et son soutien pendant ces quatre années. Et surtout, merci à toi, Louis. Tu as suivi de près toutes les évolutions de ma thèse, dans les moments de joie comme dans ceux de doute et de stress. Tu as toujours été ma constante, m'encourageant et m'apaisant. Courage à toi maintenant pour ta dernière ligne droite.

Acronyms

AMR	Antimicrobial resistance
AR	Aspect ratio
Au NPs	Gold nanoparticles
BJH	Barrett-Joyner-Halenda
CNC	Computer Numerical Control
DBR	Distributed Bragg reflectors
EF	Enhancement factor
EOT	Effective optical thickness
FDTD	Finite-difference time-domain
FEM	Finite element method
FSM	Freestanding membrane
LFIEF	Local field intensity enhancement factor
LoD	Limit of detection
LSPR	Localized surface plasmon resonance
MACE	Metal-Assisted Chemical Etching
MGITC	Malachite Green isothiocyanate
NRs	Nanorods
PSi	Porous silicon
RIFTS	Reflective Interferometric Fourier Transform Spectroscopy
SERS	Surface-Enhanced Raman Scattering
SLIM	Spectroscopic liquid infiltration method
TMM	Transfer matrix method
WHO	World Health Organization

Author's publication list

Related journal papers

JP1. C. Gevers, L. Lejeune, E. Masarweh, S. Hermans and L. A. Francis, "Freestanding Porous Silicon Membranes for Sensing Enabled by Flow-Through Decoration of Gold Nanoparticles", *ACS Appl. Nano Mater*, vol. 8, no. 44, pp. 21285-21293, 2025. DOI: 10.1021/acsanm.5c03632

JP2. R. Vercauteren, C. Gevers, J. Mahillon and L. A. Francis, "Design of a porous silicon biosensor: Characterization, modeling and application to the indirect detection of bacteria", in *Biosensors*, vol. 14, no. 2, p. 104, 2024. DOI: 10.3390/bios14020104

Related conference oral presentations

CO1. C. Gevers, L. Lejeune, S. Hermans and L. A. Francis, "Increase of the SERS signal from Gold Nanospheres in porous Silicon", in *6th SCOPe National Conference, Belgium*, 2023.

CO2. C. Gevers, L. Lejeune and L. A. Francis, " Modelling the reflectance of Porous Silicon thin films by transfer matrix approach", in *Measuring By Light, Netherlands*, 2025.

CO3. C. Gevers, L. Lejeune, S. Hermans and L. A. Francis, "Modeling the Reflectance of Porous Silicon Decorated with Plasmonic Nanoparticles Using the Transfer Matrix Method", in *Congrès Géneral de la Société Française de Physique, France*, 2025.

CO4. C. Gevers, L. Lejeune, S. Hermans and L. A. Francis, "Modeling the Reflectance of Porous Silicon Decorated with Gold Nanoparticles", in *SCOPe National Conference, Belgium*, 2025.

Related conference posters

CP1. C. Gevers, L. Lejeune, R. Vercauteren, S. Hermans and L. A. Francis, "Implementation of a numerical model for the computation of the electric field enhancement of nanodumbbells", in *SPIE Nanoscience + Engineering, San Diego, California, USA*, 2023.

CP2. C. Gevers, L. Lejeune, S. Hermans and L. A. Francis, "Computation and Experimental Validation of the Electric Field enhancement of Nanodumbbells", in *Belgian Photonics Online Meetup*, 2024.

CP3. C. Gevers, L. Lejeune, S. Hermans and L. A. Francis, "Increase of the SERS Signal by Plasmonic Nanoparticles in Porous Silicon", in *Porous Semiconductors - Science and Technology, Czech Republic*, 2024.

In preparation

FP1. L. Lejeune, C. Gevers, A. Verdin, A. Engel, C. Malherbe, L. A. Francis, S. Hermans , "Influence of gold nanorods aspect ratio on electromagnetic enhancement and its potential for surface-enhanced Raman scattering in colloidal suspension", 2026, Physical Chemistry Chemical Physics, submitted.

FP2. C. Gevers, L. Lejeune, S. Hermans and L. A. Francis, "Impact of Bragg Mirror Architectures on Surface-Enhanced Raman Scattering in Porous Silicon Freestanding Membranes", 2026.

FP3. L. Lejeune, C. Gevers, L. A. Francis, S. Hermans , "Higher understanding on electromagnetic enhancement of gold nanodumbbells prepared by an easy seed-mediated protocol for surface enhanced Raman scattering application", 2026.

Contents

Abstract i

Acknowledgements iii

Acronyms vii

Author's publication list ix

Contents xi

Introduction 1

1 Understanding the SERS effect of a single Au nanoparticle . . 9

1.1 Background on SERS 10

1.1.1 Principles of Raman scattering 10

1.1.2 Principles of plasmon resonance 12

1.1.3 Principles of SERS 14

1.2 Related work 16

1.3 Quantification of the SERS effect 17

1.3.1 Analytical approach 18

1.3.2 Numerical electromagnetic modeling 20

1.3.3 COMSOL model for electromagnetic response 21

1.3.4 A simple comparison example: the metallic nanosphere 22

1.4 Nanorods 23

1.4.1 Influence of the nanorod AR and size 25

1.4.2 Dimer configuration 30

1.4.3 Comparison with experimental measures 33

1.4.4 SERS modelisation of nanorod suspensions 41

1.4.5 Discussion 44

1.5 Nanodumbbells 45

1.5.1 Results . . . 46
1.5.2 SERS modelisation of nanodumbbell suspensions . . . 48
1.5.3 Discussion . . . 48
1.6 Environment . . . 50
1.6.1 Coating . . . 50
1.6.2 Optimal effective medium . . . 53
1.7 Key message . . . 54

2 Understanding the porous silicon material . . . 57
2.1 Background of PSi . . . 58
2.1.1 Fabrication . . . 59
2.2 Characterization of porous silicon . . . 61
2.2.1 Porosity & etch rate . . . 62
2.2.2 Pore size . . . 64
2.2.3 Nanostructures . . . 65
2.2.4 Sacrificial layer . . . 67
2.2.5 Modeling . . . 70
2.3 Freestanding membranes . . . 75
2.3.1 Related work . . . 75
2.3.2 Fabrication . . . 77
2.3.3 Controlled release of the FSM . . . 80
2.3.4 Microfluidic integration . . . 83
2.4 Bragg mirror FSM . . . 85
2.4.1 Tuning of the stopband . . . 87
2.4.2 Fabrication of Bragg FSM . . . 88
2.5 Key message . . . 91

3 Decoration of PSi with Au Nanoparticles for SERS application 93
3.1 Related work . . . 94
3.2 Porous silicon as SERS substrate . . . 96
3.2.1 Simulation of the pore effect . . . 98
3.3 Decoration of the FSM . . . 101
3.3.1 NPs synthesis protocol and characterization . . . 101
3.3.2 Methodology . . . 102
3.3.3 Quantification of the decoration . . . 105
3.3.4 Reflectance shift . . . 107
3.4 SERS measurement on PSi . . . 112
3.4.1 Instrumental characterization . . . 112
3.4.2 Sensing layer . . . 112

3.4.3 Bragg mirror 114
3.4.4 Discussion 118
3.5 Key message 119

Conclusions and Perspectives **121**

Appendix **131**

Bibliography **133**

Introduction

Thesis motivation

Antimicrobial resistance (AMR) is increasingly recognized as one of the major global health threats of the 21st century [1, 2]. According to the World Health Organization (WHO) new resistance mechanisms are emerging and spreading globally, threatening our ability to treat common infectious diseases and resulting in prolonged illness, disability and death [1]. The rapid emergence of resistant pathogens is strongly accelerated by the misuse and overuse of antibiotics, often resulting from the absence of rapid and reliable diagnostic tools [3]. In clinical practice, the lack of fast pathogen identification frequently leads to the empirical administration of broad-spectrum antibiotics as an immediate response to infection, which further contributes to the development of AMR [1, 3].

To help address this challenge, significant research efforts are currently focused on the development of rapid, sensitive, and selective biosensing platforms for pathogen detection [4, 5, 6]. Within the laboratory of Pr. Laurent Francis, research has been dedicated to the development of porous silicon (PSi)-based optical biosensors for bacterial detection, in collaboration with Pr. Jacques Mahillon and Pr. Annika Gillis at UCLouvain.

Numa Couniot [7] started the research with CMOS readout interfaces for capacitive biosensors. Jonathan Rasson [8] then demonstrated a proof of concept for the selective optical detection of bacteria using porous silicon sensors combined with the in situ lysis of bacterial cells. His work showed that the use of lytic enzymes enabled bacterial detection without requiring complex surface functionalization or extensive sample pre-treatment. However, the sensitivity of the platform remained limited, with detection

achieved for bacterial concentrations between 10^7 and 10^8 CFU/mL. Building upon these results, Roselien Vercauteren [9] further improved the sensing strategy by introducing a membrane-based flow-through configuration. By forcing the bacterial suspension through the porous silicon membrane, a significantly larger number of lysed bacterial cells could be retained within the sensing structure, leading to a substantial enhancement in sensitivity. This approach reduced the limit of detection (LoD) by four orders of magnitude, from 10^7 CFU/mL to 10^3 CFU/mL.

Despite the significant improvement achieved through the implementation of the membrane-based flow-through configuration, further reduction of the LoD remains necessary for practical clinical applications, where bacterial concentrations can be lower than 100 CFU/mL in the case of sepsis [10, 11, 12], or virulent urinary tract infections containing E. coli strains with concentrations only 10^2 CFU/mL [13]. Several strategies can therefore be considered to further enhance the sensitivity of PSi-based biosensors.

A first approach consists in optimizing the surface chemistry of the porous silicon matrix in order to improve bacterial capture efficiency. The functionalization of the PSi surface with selective bioreceptors such as antibodies [14], aptamers [15], bacteriophages, or antimicrobial peptides [16] could significantly increase the number of bacteria immobilized within the pores [17].

Another strategy to further decrease the limit of detection of PSi-based biosensors consists in integrating electrochemical sensing approaches alongside or in place of purely optical transduction mechanisms [18]. While optical PSi sensors rely on refractive index variations induced by bacterial capture or lysis, electrochemical detection enables the direct measurement of charge transfer, impedance, or redox reactions occurring at the sensor surface, often resulting in significantly higher sensitivities. Recent studies have demonstrated that electrochemical PSi platforms can achieve detection limits in the pico- to nanomolar range for biological targets due to the exceptionally large internal surface area of PSi and its tunable surface chemistry [19, 20, 21].

One of the most promising method to improve the sensitivity consists in replacing or complementing reflectometric readout with Surface-Enhanced Raman Scattering (SERS)-based detection [22]. The decoration of the PSi matrix with plasmonic nanoparticles creates highly localized electromagnetic "hot

spots" that amplify Raman signals by several orders of magnitude [23]. A broad SERS-based biosensing platform combining antibody-functionalized gold nanoparticles linked with a Raman reporter and a silver-coated porous silicon microarray as the SERS transducer demonstrated limits of detection as low as 3 CFU/mL for E. coli, [24]. Similarly, a silver-coated nanoporous silicon substrate functionalized in an immunosensor format for E. coli detection in milk achieved a sensitivity of 2 CFU/mL [25].
These performances represent an improvement of three orders of magnitude compared to the 10^3 CFU/mL currently achieved in our laboratory. These results strongly suggest that transitioning our platform toward a SERS readout, while preserving the PSi architecture, constitutes a technically feasible and highly impactful upgrade. Several studies have already demonstrated the advantages of combining PSi with SERS techniques [26, 27]. In addition, SERS has also been shown to benefit from membrane-based architectures [28] or filter-based enhancements [29], further highlighting the relevance and potential of the present work.

Another important motivation behind this work originates from the collaboration established between the laboratory of Pr. Laurent Francis and the laboratory of Pr. Sophie Hermans from the Institute of Condensed Matter and Nanosciences at UCLouvain, and more specifically with the PhD candidate Louise Lejeune, whose research is closely related to the present study. This collaboration creates the opportunity to combine the expertise developed within the laboratory on porous silicon membranes, flow-through architectures, and numerical modeling with the knowledge of plasmonic nanoparticles synthesis and their Raman properties. The intersection of these two research fields naturally leads to the investigation of SERS substrates based on porous silicon structures.

Thesis objectives

The objective of this work is therefore to design and study a porous silicon based SERS substrate as a proof of concept. Following this methodology, the aim is to link the porous silicon morphology to the SERS response, and to identify the design parameters influencing the signal sensitivity and its reproducibility. Instead of focusing on achieving record performance, this

thesis aims to give a clearer insight into the design of efficient and robust porous silicon SERS substrates. To achieve this objective, three fundamental building blocks must first be understood before designing the final SERS substrate:

Research block #1 The first aspect of SERS is not directly related to the substrate itself, but rather to the enhancing element, namely the plasmonic nanoparticles. It is now well established that metallic nanoparticles can strongly enhance the surrounding electromagnetic field through localized surface plasmon resonance effects. With our background in electrical engineering, there is a strong interest in accurately modeling and simulating this plasmonic behavior. This interest is further reinforced by the collaboration with Louise Lejeune, which provides the opportunity to synthesize nanoparticles with a wide variety of shapes and sizes. In addition, since porous silicon will ultimately serve as the SERS substrate, it is important to understand how the surrounding environment affects the plasmonic response of the nanoparticles. Therefore, the following question is addressed:

RQ1: How can a plasmonic nanoparticle be tuned to enhance the electromagnetic field?

Research block #2 Before investigating the SERS response itself, it is essential to understand and optimize the porous silicon substrate. The material parameters must be tuned to fabricate porous silicon membranes, as previous work has shown that flow-through configurations provide better performance than flow-over systems. With this in mind, the objective is to design a porous substrate that can be integrated into a microfluidic setup and subsequently decorated with plasmonic nanoparticles. This leads to the following question:

RQ2: How can a porous substrate be fabricated to enable efficient decoration with plasmonic nanoparticles?

Research block #3 The third step of this work focuses on the homogeneous decoration of porous silicon with plasmonic nanoparticles. Several approaches have already been proposed in the literature, but they often result in pore clogging or excessive nanoparticle aggregation at the surface of the pores. The advantage of the present work lies in the possibility to simultaneously tune both the plasmonic nanoparticles (Block #1) and the porous silicon membranes integrated within a microfluidic setup (Block #2). This motivates the following question:

RQ3: How can porous silicon be decorated to enable the integration of various types of nanoparticles, and how are these nanoparticles distributed within the porous structure?

Bringing it all together Once these three fundamental building blocks are understood, it becomes possible to investigate the influence of porous silicon on the SERS response itself. Multiple parameters related to both the nanoparticles and the porous substrate can then be tuned in order to study their impact on the SERS signal. The final objective is therefore to understand how these different building blocks interact and contribute to achieving the highest possible SERS enhancement while maintaining good reproducibility. This leads to the final research question:

RQ4: What is the effect of the decorated porous substrate on the SERS signal?

Thesis outline

To address these four main research questions, this thesis is structured as follows: Chapter 1 introduces the fundamentals of SERS and plasmonic nanoparticles (RQ #1). Chapter 2 focuses on porous silicon and membrane fabrication (RQ #2), while Chapter 3 combines the findings of the two previous chapters to investigate the decoration of porous silicon and its influence on the SERS response (RQ #3 and #4). Each chapter begins with a brief introduction presenting the necessary background and related work relevant to the topics discussed.

Chapter 1 investigates the influence of nanoparticle shape and size on their plasmonic properties. The main objective of this chapter is to develop a comprehensive understanding of the parameters governing the optical response of plasmonic nanoparticles, such as their resonance wavelength and extinction cross-section. To achieve this, a numerical simulation model is first developed and compared with analytical solutions in order to validate the numerical approach. Once validated, the model is applied to different nanoparticle geometries, including nanorods and nanodumbbells. The obtained results are compared with experimental measurements to further understand the mechanisms responsible for electromagnetic field enhancement. It is shown that additional calculations must be performed

to account for light extinction in colloidal suspensions. In this work, however, the analysis is extended to nanoparticle geometries beyond spherical particles. Finally, the chapter investigates the influence of the surrounding environment on the plasmonic response, highlighting the potential of high refractive index materials such as porous silicon for SERS applications.

Chapter 2 first focuses on the fabrication of porous silicon. Understanding the fabrication parameters and their influence on the resulting material properties is essential, particularly regarding porosity, etch rate, and pore size. We demonstrate that large pore sizes can be achieved, enabling the future integration of plasmonic nanoparticles within the porous structure. The fabrication of porous silicon membranes is then investigated. Previously developed membrane fabrication methods within the laboratory required numerous fabrication steps and up to one week of processing time. In this work, a new fabrication approach is proposed, reducing the total fabrication time to approximately 25 minutes. This rapid fabrication process enables fast optimization of the membrane parameters for subsequent decoration experiments. One of the most critical fabrication steps is the membrane release, which is studied using a numerical model to identify the optimal fabrication conditions. Finally, the fabricated membranes are characterized within a microfluidic cell in order to understand the influence of pore size on fluid flow and prepare the membranes for nanoparticle decoration.

Chapter 3 begins by combining the two previous building blocks and proposes a simple method for decorating porous silicon with plasmonic nanoparticles. The membranes fabricated in Chapter 2 are integrated into a microfluidic cell, through which a colloidal suspension of plasmonic nanoparticles is flowed. This approach enables homogeneous decoration of the porous structure without clogging the pores and allows the integration of various colloidal nanoparticle suspensions. In this work, the membranes are decorated with gold nanorods, and cross-sectional analyses are performed to verify that the nanoparticles are distributed throughout the entire membrane thickness. Reflectance measurements of the decorated membranes are also carried out to further support the successful decoration of the porous structure.

The second part of this Chapter 3 addresses RQ4. The objective is to demonstrate that porous silicon is not only interesting due to its surface roughness, as often emphasized in the literature, but also because of the optical prop-

erties of the porous medium itself. First, a numerical model is developed to investigate the influence of the porous environment surrounding the nanoparticles. Subsequently, the SERS response of a Raman-active dye is measured and compared for different porous structures in order to understand the influence of the substrate morphology and optical properties. Based on these results, different decorated Bragg mirrors are compared and discussed.

Finally, this thesis concludes by comparing the contributions of this work with the existing state-of-the-art. The remaining challenges are discussed, and several perspectives for future research are proposed before concluding with a final word of the work accomplished.

1

Understanding the SERS effect of a single Au nanoparticle

Plasmonic nanoparticles (NPs) are known for their ability to strongly enhance the surrounding electromagnetic field through localized surface plasmon resonance (LSPR) effects. These enhancement mechanisms are at the core of Surface-Enhanced Raman Scattering (SERS) and strongly depend on the nanoparticle geometry, size, material, and surrounding environment. Understanding how these parameters influence the plasmonic response is therefore essential for the design of efficient SERS substrates.
This interest is further reinforced by the collaboration with Louise Lejeune, which provides the opportunity to synthesize nanoparticles with a wide variety of shapes and sizes. The following research question is therefore addressed:

RQ1: How can a plasmonic nanoparticle be tuned to enhance the electromagnetic field?

This chapter establishes the foundations required for the plasmonic nanoparticles that will later be integrated into the porous substrates presented in Chapter 2. Their incorporation and application in SERS-active porous silicon membranes will subsequently be discussed in Chapter 3.

The chapter first introduces the theoretical background necessary to understand the principles of SERS, beginning with Raman scattering, followed by plasmonic phenomena, and finally the mechanisms governing Surface-Enhanced Raman Scattering. A short review of the related literature is then presented in order to summarize the current state of the art.
Next, the quantification of the SERS enhancement is discussed. An analytical approach is first introduced together with its limitations, after which a numerical model is presented. Both approaches are compared using the simple case of a nanosphere in order to validate the numerical framework. The validated model is then applied to more complex geometries. The optical response and SERS enhancement of gold nanorods are investigated and compared with experimental measurements, followed by a similar analysis for nanodumbbells. Finally, the influence of the surrounding environment on the plasmonic response is studied, highlighting the potential interest of high-refractive-index materials.
The results presented in this chapter are based on the collaborative work conducted with Louise Lejeune, where the numerical simulations developed in this thesis support and complement her experimental observations.

1.1 Background on SERS

Here, only a brief introduction to the basic principles of SERS is provided. For a more detailed description, the reader is referred to the reference book by Le Ru and Etchegoin [30], while a more concise introduction can also be found in the thesis of Alexandre Verdin [31].

1.1.1 Principles of Raman scattering

When light interacts with matter, part of the incident energy can be absorbed or scattered, leading to a reduction of the transmitted intensity. This attenuation is described by the extinction cross-section, which combines both absorption and scattering contributions.

Scattering processes can be either elastic or inelastic. In elastic (Rayleigh) scattering, the scattered photon keeps the same energy as the incident photon. In contrast, inelastic scattering involves an energy exchange with the

molecule, resulting in a frequency shift of the scattered light.

Raman scattering is a well-known inelastic scattering process and forms the basis of Raman spectroscopy. It was first observed by C. V. Raman in 1928 [32]. It originates from the interaction between light and vibrating or rotating molecules. As illustrated in Fig. 1.1, the scattered light contains a dominant Rayleigh component together with weaker Stokes and anti-Stokes contributions. In the Stokes process, the molecule gains energy, while in the anti-Stokes process it loses energy. These frequency shifts are directly related to the molecular vibrational or rotational modes and therefore provide a unique spectroscopic fingerprint of the material.

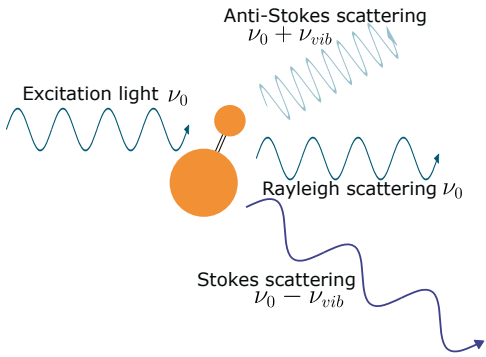


Fig. 1.1 Illustration of the scattering processes when monochromatic light interacts with a molecule that has a vibrating bond at a frequency of ν_{vib}.

Raman scattering can be interpreted as an instantaneous interaction involving a virtual intermediate state rather than a real electronic transition, unlike fluorescence [30]. This means that Raman scattering can happen without a direct absorption of the photon; the Raman scattering can occur even when the incident photon energy does not match an electronic transition of the molecule. However, because this process relies on virtual states, its probability remains intrinsically low, which explains the weak intensity of Raman signals [30].

Within a quantum mechanical description, Raman scattering is represented as the absorption of an incident photon followed by the emission of a scattered photon through a virtual state [30]. As illustrated in Fig. 1.2, three main processes can occur: Rayleigh, Stokes, and anti-Stokes scattering. In

Rayleigh scattering, the molecule returns to its initial vibrational state and the scattered photon keeps the same energy. In Stokes scattering, part of the photon energy is transferred to the molecule, resulting in scattered light with lower energy. Conversely, in anti-Stokes scattering, the molecule initially occupies an excited vibrational state ($\nu = 1$) and transfers energy to the scattered photon, producing light with higher energy.

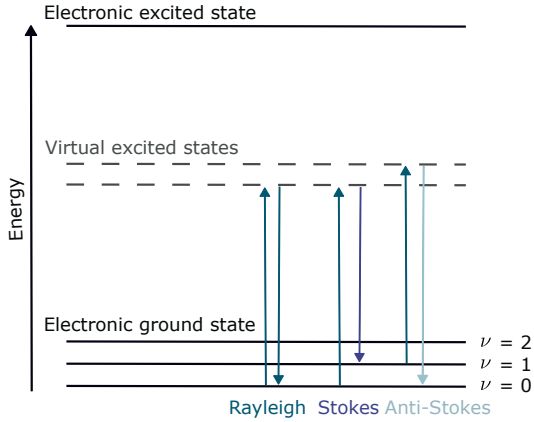


Fig. 1.2 Energy diagram of the three scattering processes involved in Raman vibrational spectroscopy.

When the energy of the virtual state corresponds to that of a real electronic transition of the molecule, the Raman scattering efficiency increases dramatically, often by several orders of magnitude. This effect is known as resonance Raman scattering and provides a much stronger signal [30].

1.1.2 Principles of plasmon resonance

Metals such as gold, silver, and copper exhibit optical properties that differ strongly from those of conventional dielectrics, particularly due to their high reflectivity in the visible range. These properties arise from the presence of free conduction electrons, which can collectively behave as an electron plasma moving within a background of fixed positive ions [33].

The optical response of this electron plasma can be approximated using the Drude model, where conduction electrons are considered free and not

bound by a restoring force. As a consequence, the dielectric function of metals is characterized by a frequency-dependent response dominated by these free carriers.

Plasmonic phenomena are commonly interpreted as collective oscillations of the free electrons within a metal under electromagnetic excitation. These oscillations, referred to as plasmons, correspond to quantized charge-density waves and are intrinsically affected by damping mechanisms such as electron scattering [30]. In practice, however, the plasmonic behavior of a material is most conveniently described through its frequency-dependent dielectric function, which fully determines its optical response.

One of the key characteristics of metals is that the real part of their dielectric function can become negative while the imaginary part remains relatively small over specific frequency ranges. These conditions enable the existence of plasmon resonances, which do not occur in standard dielectric materials. For most metals, the plasma frequency lies in the ultraviolet region, making the visible range particularly suitable for plasmonic phenomena [30]. This behavior is illustrated in Fig. 1.3 using data from [34].

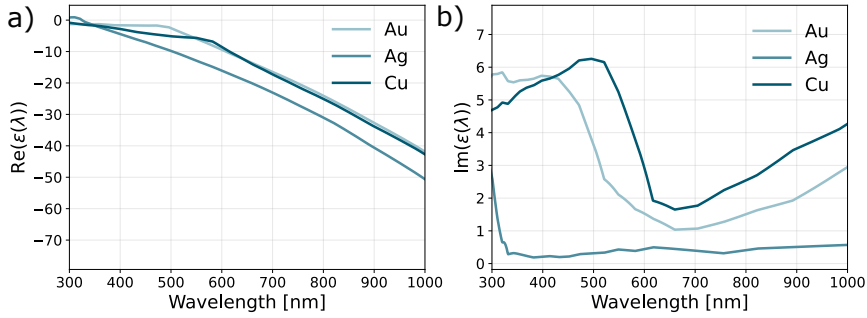


Fig. 1.3 Dielectric function of Au (light blue), Ag (blue) and Cu (dark blue); a) real part and b) imaginary part.

Among plasmonic materials, gold and silver are the most widely used because their dielectric properties allow resonances to occur in the visible and near-infrared spectral ranges. Silver generally provides lower optical losses and stronger electromagnetic enhancement in the visible domain, whereas gold offers superior chemical stability and is therefore often preferred for

practical applications and longer excitation wavelengths.

A simple way to understand localized plasmonic effects is to consider a metallic nanoparticle much smaller than the wavelength of the incident light. Under this electrostatic approximation, the electric field inside a spherical particle E_{in} can be considered uniform and proportional to the incident field E_0, and is given by [30]:

$$E_{in} = \frac{3\varepsilon_{med}}{\varepsilon_{met}(\omega) + 2\varepsilon_{med}} E_0 \tag{1.1}$$

where ε_{met} and ε_{med} are respectively the dielectric functions of the metal and the surrounding medium. A resonance occurs when the denominator approaches zero, corresponding approximately to the condition $\varepsilon_{met}(\omega) = -2\varepsilon_{med}$. At this point, the local electromagnetic field as well as the absorption and scattering cross-sections become strongly enhanced. This phenomenon is known as localized surface plasmon resonance (LSPR).

An important characteristic of LSPR is its strong sensitivity to the nanoparticle geometry and surrounding environment. Although the metal defines the spectral region where resonances may occur, the exact resonance wavelength depends strongly on parameters such as particle size, shape, and local refractive index. Consequently, nanoparticles made of the same material can exhibit very different optical responses depending on their geometry and environment.

1.1.3 Principles of SERS

Despite its excellent chemical specificity, Raman spectroscopy suffers from an intrinsically weak signal intensity, as only about 10^{-6} to 10^{-8} of the incident photons are inelastically scattered [35]. Surface-Enhanced Raman Scattering (SERS) overcomes this limitation by amplifying the Raman response of molecules located near plasmonic nanostructures.

The origin of this enhancement is closely related to the optical response of metallic nanoparticles. The charge displacement of the plasmon induces a dipole moment inside the nanoparticle. For a small metallic sphere, the

induced dipole magnitude is given by [30]:

$$p \propto \frac{\varepsilon_{met}(\lambda) - \varepsilon_{med}}{\varepsilon_{met}(\lambda) + 2\varepsilon_{med}} \tag{1.2}$$

where ε_{met} and ε_{med} correspond respectively to the dielectric functions of the metal and the surrounding medium. When the resonance condition is approached, localized surface plasmon resonances are excited, leading to a strong enhancement of the electromagnetic field near the nanoparticle surface. In the case of other geometries than spheres, a geometrical factor or depolarization factor can be introduced and characterizes the curvature of the ellipsoid along its corresponding axis [30].

The SERS effect is generally described as the combination of two contributions: electromagnetic enhancement and chemical enhancement. The electromagnetic contribution is the dominant mechanism in most situations and originates from the interaction between the incident electromagnetic wave and the plasmonic nanostructure [30]. Near the metal surface, the local electric field can become significantly larger than the incident field, especially at localized regions known as "hotspots". Molecules located within these regions experience a much stronger excitation field, resulting in an amplified Raman response.

The chemical enhancement mechanism is typically weaker and is associated with modifications of the molecular polarizability caused by direct interactions between the molecule and the metal surface, often involving charge-transfer processes. Since this contribution usually remains secondary compared with the electromagnetic effect [30], it is often neglected in first-order SERS analyses.

In practice, the electromagnetic contribution is commonly estimated using the so-called $|E|^4$ approximation [36]. In this framework, the SERS intensity is assumed to scale with the fourth power of the local electric field enhancement relative to the incident field. This approximation arises because the electromagnetic field enhances both the excitation and emission processes. When the Raman shift is small, the excitation and Raman frequencies can be considered approximately identical, leading to the widely used expression [30]:

$$M_{SERS} \propto \left| \frac{E_{loc}}{E_{inc}} \right|^4, \tag{1.3}$$

where E_{loc} is the local field at the surface and E_{inc} is the incident field. Although simplified, the $|E|^4$ approximation provides a practical and efficient way to estimate SERS enhancement factors and remains extensively used in the literature.
Overall, SERS can therefore be understood as the result of strong electromagnetic field confinement near plasmonic nanostructures, enabling a dramatic amplification of an otherwise weak Raman signal.

1.2 Related work

The literature on SERS is extremely extensive, and the present section is therefore not intended to provide a comprehensive review of the field. Instead, only a selection of articles relevant to the present work is briefly discussed here.

The influence of nanoparticle size, shape, and spatial organization on the plasmonic response has been extensively investigated in the literature. Numerous studies have shown that increasing the nanoparticle size generally induces a red-shift of the plasmon resonance wavelength due to retardation effects and modifications of the electron oscillation dynamics [37, 38, 39]. In parallel, shape anisotropy plays a major role by altering the surface charge distribution and therefore the resonance peak positions. Nanoparticles with sharp tips, edges, or corners are particularly interesting because they can strongly localize the electromagnetic field, leading to intense plasmonic hotspots and enhanced local field amplification [40, 41, 42].

A wide range of plasmonic geometries has consequently been explored, including nanocubes [43, 44, 45], nanourchins [46, 47], nanowires [44, 48], nanostar antennas [49, 50], and many others. These studies highlight both the large design space available for plasmonic nanoparticles and the complexity involved in identifying the most suitable geometry for a given SERS application.

Beyond the nanoparticle geometry itself, the spatial arrangement and surface coverage of nanoparticles are also critical parameters for SERS substrates, since the density and distribution of plasmonic hotspots strongly depend on nanoparticle organization [51]. Carefully engineered nanoparticle arrays have therefore demonstrated very high sensitivities together with improved signal reproducibility [52, 53].

Numerous studies have already investigated, through numerical simulations, the influence of plasmonic nanoparticle parameters such as size, shape, and surrounding environment on the electromagnetic field enhancement [54, 55, 56].
The objective of the present chapter is therefore not to develop entirely new numerical methods, but rather to use and adapt existing simulation tools in order to better understand the physical mechanisms governing the plasmonic response. In addition, thanks to the collaboration with Louise Lejeune, these numerical results can be directly compared with experimental measurements performed on synthesized nanoparticles, allowing the simulations to support and validate the experimental observations.

1.3 Quantification of the SERS effect

The quantification of the SERS effect is a central step in evaluating and comparing the performance of plasmonic substrates. In general, SERS enhancement is described through an enhancement factor (EF), which relates the Raman signal obtained in the presence of a nanostructured metallic surface to that of the same molecule in a non-enhancing environment. From a theoretical perspective, the dominant contribution to this enhancement arises from the electromagnetic mechanism, which is associated with the excitation of localized surface plasmon resonances in metallic nanostructures.

Within the quasi-static approximation, the local field around a small metallic sphere can be expressed as a function of the dielectric properties of the particle and its surrounding medium, leading to an explicit formulation of the enhancement factor. Such analytical models provide valuable physical insight, particularly regarding the resonance condition and the role of material permittivity.

However, realistic SERS substrates often involve complex geometries for which analytical solutions are no longer valid. In these cases, numerical methods based on the solution of Maxwell's equations are employed to evaluate the local electromagnetic fields. Techniques such as the finite-difference time-domain (FDTD) method or the finite element method (FEM) are commonly used to compute the spatial distribution of the electric field and, consequently, the SERS enhancement factor through the $|E|^4$ approximation.

In this work, the quantification of the SERS effect is carried out by focusing exclusively on the electromagnetic contribution. The chemical enhancement mechanism, which involves charge-transfer interactions between the molecule and the metal surface and typically requires a quantum mechanical treatment, is not considered here. Instead, the analysis is restricted to the evaluation of the local electromagnetic field enhancement generated by the nanostructures, which is generally accepted to be the dominant contribution in most SERS configurations [57, 58]. This approach allows for a consistent and tractable framework to compare different geometries and to identify the key parameters governing the enhancement. If a more detailed explaination is needed, the reader is referred to chapter 5 of the reference book of Le Ru and Etchegoin [30].

1.3.1 Analytical approach

Analytical approaches provide a valuable framework for describing the optical response of plasmonic nanostructures, offering both physical insight and, in some cases, exact solutions to Maxwell's equations for nanoparticles that are much smaller than the wavelength [30].

Despite their mathematical complexity, such analytical formulations can be implemented efficiently using modern computational tools. Several open-source libraries are available to facilitate their practical use. For example, PyMieScatt [59] provides a user-friendly Python implementation of Mie theory, allowing for the calculation of scattering, absorption, and near-field properties of spherical particles. Le Ru and Etchegoin [30] also provided an easy-to-use implemenation of the Mie theory in the form of Matlab codes.

Mie theory

A detailed understanding of Mie theory is not strictly required to grasp the fundamental principles underlying SERS and other plasmon-related phenomena. Nevertheless, it provides a robust and well-established theoretical framework for interpreting many aspects of the problem.

The problem of electromagnetic scattering by a spherical particle can be solved analytically using Mie theory [60, 61]. This represents one of the simplest exact solutions to Maxwell's equations for a finite object, and as such, it serves as an important model system for exploring the validity of common approximations and for gaining insight into the optical properties of metallic nanoparticles. It should be noted, however, that "simple" in this context is relative: while conceptually accessible, the mathematical formalism of Mie theory remains involved. For this reason, its full derivation is not presented here and is instead provided in Appendix H of Le Ru and Etchegoin [30].

Mie theory describes the scattering properties of homogeneous spherical particles of arbitrary size and composition, whether dielectric or metallic. The formalism can be extended to more complex configurations, such as multilayered (coated) spheres and, with additional complexity, systems of multiple spheres [30].

For assemblies composed of several nanoparticles, Maxwell's equations can be solved rigorously using the generalized Mie theory, which explicitly accounts for the electromagnetic interactions and coupling effects occurring between neighboring spherical particles. Although this framework provides an exact analytical solution for multi-sphere systems, its mathematical formulation rapidly becomes highly complex, which has limited its widespread use in SERS-related studies [30].

Spherical nanoparticles constitute a convenient and widely used model because of their geometrical simplicity and the availability of analytical solutions. However, their strong symmetry also restricts the range of physical phenomena that can be investigated, especially those associated with anisotropic optical responses. To overcome this limitation, spheroidal geometries, corresponding to ellipsoids of revolution with two identical axes,

are often considered as a natural extension. These particles preserve part of the mathematical tractability of spherical systems while introducing shape-induced anisotropy in their plasmonic behavior. Similar to spheres, the electromagnetic scattering problem for spheroids can also be solved analytically through approaches derived from Mie theory [62]. Nevertheless, such analytical formulations generally cannot be extended to more complex nanoparticle geometries.

1.3.2 Numerical electromagnetic modeling

While analytical models provide valuable physical insight into plasmonic systems, their applicability remains limited to relatively simple geometries such as spheres or spheroids. For more realistic nanostructures, analytical approaches are generally no longer sufficient, and numerical methods become necessary to solve Maxwell's equations and accurately describe the electromagnetic response.

Numerical approaches can be broadly divided into two categories. The first category includes general-purpose numerical methods for solving partial differential equations, such as the FDTD method and the FEM. FDTD solves Maxwell's equations in the time domain and is suited for transient analysis. This method is implemented in widely used software packages such as Lumerical FDTD and MEEP [63]. In contrast, FEM operates in the frequency domain and is especially efficient for studying resonant phenomena and handling complex geometries [30].
The second category consists of semi-analytical approaches specifically developed for electromagnetic simulations, such as the discrete dipole approximation (DDA) and the multiple multipole method (MMP). These methods can offer improved computational efficiency for certain classes of problems. While they are not inherently more difficult to implement, the available codes are generally less user-friendly than those for FDTD or FEM. For DDA, notable implementations include DDSCAT [64], one of the historical reference codes, and the more recent ADDA code [65].

Overall, numerical methods provide a powerful and flexible framework for investigating realistic plasmonic systems and are indispensable for accurately predicting electromagnetic-field enhancements in SERS. In this

work, the focus is placed on FEM simulations performed with COMSOL Multiphysics, notably because access to the software licence is available within the institute.

1.3.3 COMSOL model for electromagnetic response

The COMSOL simulation model is based on the work of Grand *et al.* [66], where finite-element method simulations are carried out using the Electromagnetic Waves, Frequency Domain (emw) module of COMSOL Multiphysics 6.2 to model the electromagnetic response of plasmonic nanoparticles. The simulations are performed in the frequency domain, with the time dependence defined as $\exp(+i\omega t)$. The excitation consists of an incident linearly x-polarized plane wave propagating in the z-direction through a homogeneous dielectric medium with a relative permittivity that varies between 1 (air), 1.77(water) and 2.18 (silica). The refractive index of Au in the visible wavelength range is obtained from Johnson and Christy [67]. To avoid any reflection of the incident or scattered waves, the boundary conditions are fixed as perfectly matched layers (PML): a 5-layer spherical bounding box with a thickness of 100 nm.

The incident electric field $E_{inc}(r)$ is a propagating plane wave of amplitude E_0 = 1 V/m along z and polarized along x axis. The local electric field enhancement is quantified through the local field intensity enhancement factor $M(r) = |\frac{E(r)}{E_0}|^2$, calculated at each point on the nanoparticle surface, with E being the electric field and is computed as the sum of the incident field and the scattered field by the nanoparticle. It characterizes by how much the intensity of the electromagnetic field of the incident wave is increased with respect to the intensity in the situation without the metallic sphere E_0. To characterize the near-field resonance, the surface-averaged local field intensity enhancement $\langle M \rangle$ factor is computed as the integral of M(r) over the nanoparticle surface normalized by its total area A:

$$\langle M \rangle = \frac{1}{A} \iint_{NP} |\frac{E(r)}{E_0}|^2 \, dS \tag{1.4}$$

Optical cross-sections are determined from the electromagnetic field according to standard definitions. The scattering cross-section σ_{sca} is obtained from the flux of the complex Poynting vector of the scattered field S_{sca} through

the nanoparticle surface as expressed in Eq. 1.5, while the absorption cross-section σ_{abs} is evaluated from the power dissipation density within the nanoparticle volume, written in Eq. 1.6. The extinction cross-section σ_{ext} is then derived from energy conservation as the sum of scattering and absorption cross-sections.

$$\sigma_{sca} = \frac{1}{S_0} \iint_{NP} \mathrm{Re}(S_{sca}(r) \cdot n)\, dS, \tag{1.5}$$

$$\sigma_{abs} = \frac{1}{S_0} \iiint_{NP} Q_h\, dV, \tag{1.6}$$

where S_0 is the power density of the incident field and Q_h is the total power dissipation density.

1.3.4 A simple comparison example: the metallic nanosphere

The metallic sphere constitutes a particularly useful model system because an exact analytical solution to the electromagnetic scattering problem exists through Mie theory. This solution enables a detailed investigation of the electromagnetic response of metallic nanoparticles, including the spectral dependence of the absorption, scattering, and extinction cross-sections.

An additional advantage of this exact solution is that it provides a rigorous benchmark for assessing the validity and accuracy of numerical simulations. In the following example, a gold nanosphere with a radius of 10 nm, characterized by the dielectric function reported by Johnson and Christy [67], and embedded in an infinite non-absorbing water medium ($\varepsilon_m = 1.77$), is considered. The optical response of this system was calculated numerically using COMSOL Multiphysics and analytically using the open-source implementation PyMieScatt [59]. As shown in Fig. 1.4, the normalized absorption and extinction cross-sections almost perfectly overlap, rendering the absorption curve nearly indistinguishable from the extinction curve. Furthermore, an excellent agreement is observed between the numerical and analytical results, thereby validating the accuracy of the numerical model.
In Fig. 1.4, the values have been normalized. For small NPs, the scattering cross section is very small and can be considered negligible [68]. Consequently, absorption dominates the extinction, as evidenced by the overlap between the extinction and absorption curves.

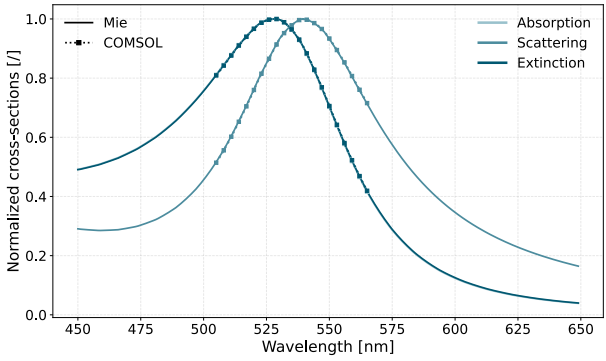


Fig. 1.4 Normalized Mie and COMSOL cross-sections of 10 nm radius gold nanosphere embedded in water with: absorption (light blue), scattering (blue) and extinction (dark blue). The Mie results, shown as solid lines, were computed from 450 nm to 650 nm, while the COMSOL simulations, shown as dashed lines with circular markers, were performed from 505 nm until 565 nm.

1.4 Nanorods

The nanorod geometry is then studied, as it is relatively simple to synthesize while already introducing an anisotropic axis, making it an ideal system for investigating the effect of shape anisotropy on electromagnetic enhancement.

This section first presents the COMSOL numerical model used throughout the study. The influence of nanorod aspect ratio (AR) and size is then analyzed in terms of resonance wavelength, extinction, absorption and scattering cross-sections, as well as electromagnetic field enhancement. Next, the effect of nanorod dimers is investigated in order to evaluate the influence of nanoparticle coupling and hotspot formation.

The numerical results are subsequently compared with experimental measurements performed on colloidal suspensions of nanorods synthesized by Louise Lejeune. This comparison demonstrates that modeling the SERS intensity of colloidal nanorods requires a more advanced approach than considering the electromagnetic enhancement alone. Finally, the section

concludes with a discussion of the main findings and their implications for the following geometry.

The COMSOL model described in section 1.3.3 is used to simulate the optical response of nanorods in order to investigate the influence of their size and aspect ratio on the resonance wavelength, extinction coefficient, and enhancement factor. The nanorod geometry implemented in COMSOL is illustrated in Fig. 1.5. The structure consists of a cylinder completed by two hemispherical ends. The geometry is fully defined by only two parameters: the radius, r, of the extremity spheres and the length, L, of the cylindrical section. The aspect ratio is defined as the ratio between the longitudinal and transverse dimensions of the nanorod, which in this case is given by: $AR = \frac{2r+L}{2r}$.

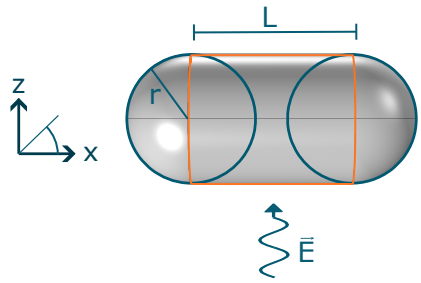


Fig. 1.5 Schematic representation of the COMSOL nanorod geometry with a radius of 5 nm and a cylinder length of 25 nm. The outlines of the two spherical caps are shown in blue, while the cylindrical section is shown in orange. The nanorod is oriented along the x-axis. The incident electric field propagates along the z-axis and is polarized along the x-axis, as indicated by the arrow.

The nanorod can adopt different orientations with respect to the polarization direction of the incident electric field. The effect of this orientation on the intensity of the surface-averaged LFIEF at both the transverse and longitudinal resonances is shown in Fig. 1.6. The longitudinal resonance reaches its maximum intensity at 0°, where the long axis of the nanorod is aligned parallel to the electric field, corresponding to the configuration illustrated in Fig. 1.5. In this orientation, the transverse mode is not excited. In contrast, at 90°, the transverse resonance is maximized because the short axis of the nanorod is alligned with the polarization field. Although the

resonance intensities strongly depend on the nanorod orientation, the resonance wavelengths of both the longitudinal and transverse modes remain unchanged. This behavior is not presented here but can be demonstrated from the classical analytical theory of Gans for spheroids, which does not depend on the orientation angle [69].

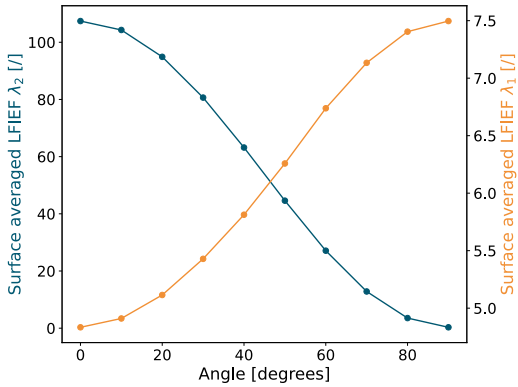


Fig. 1.6 Impact of the orientation between one nanorod (radius of 5 nm and length of 25 nm in water) and the incident electric field vector on the surface averaged LFIEF. The left axis shows the evolution of the longitudinal resonance (blue) and the right axis shows the evolution of the transverse resonance (orange).

1.4.1 Influence of the nanorod AR and size

For all the following simulations, the angle between the nanorod axis and the electric field vector is fixed at 50° in order to compare all nanorods under identical excitation conditions and be able to simulate the longitudinal and transverse modes.

Resonance wavelength λ_1 and λ_2

Different nanorod geometries were simulated, considering radii ranging from 5 to 15 nm and cylinder lengths from 10 to 70 nm in water. Fig. 1.7a shows that the longitudinal resonance wavelength exhibits a linear dependence on the AR, in agreement with the empirical relationship compiled from the literature by Huang *et al.* ($\lambda_2 = 95\,\mathrm{AR} + 420$ nm) [68, 70]. Furthermore, the nanorod radius slightly affects the slope of this relationship,

indicating that thicker nanorods experience a faster increase in resonance wavelength with increasing AR.
The influence of the AR on the transverse resonance wavelength is presented in Fig. 1.7b. Experimental study report that λ_1 undergoes a slight, nearly linear shift with increasing AR, in contrast to the much stronger red-shift of the longitudinal mode [71]. In our simulations, however, this weak trend cannot be reliably resolved: the spatial discretization step of 4 nm used introduces a numerical uncertainty on the resonance position that is of the same order of magnitude as the expected physical shift. As a result, the calculated values remain confined to a narrow range between 536 and 544 nm, and the underlying linear decrease of λ_1 is not clearly visible in our results.

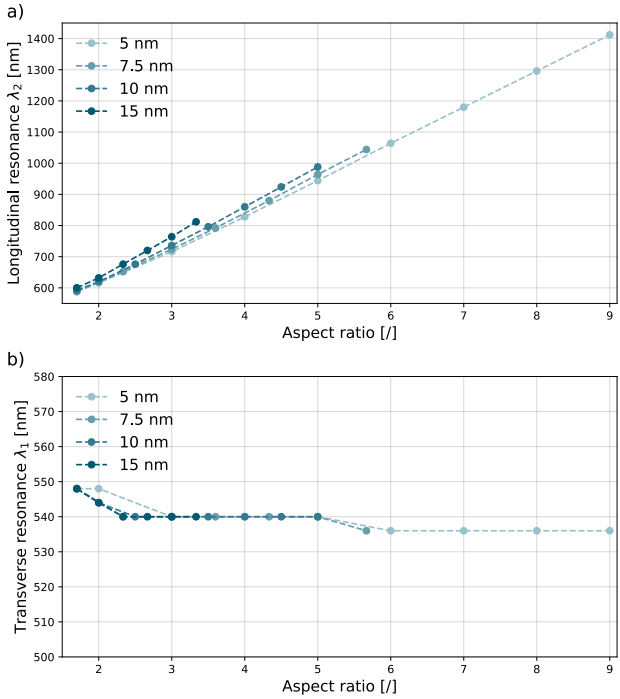


Fig. 1.7 a) Simulated evolution of the longitudinal resonance versus the AR for NRs with radii ranging from 5 nm (light blue) to 15 nm (dark blue). b) Simulated evolution of the transverse resonance versus the AR for NRs with radii ranging from 5 nm (light blue) to 15 nm (dark blue).

Cross-sections: σ_{abs}, σ_{sca}, and σ_{ext}

The extinction cross-section σ_{ext} was also calculated as a function of the wavelength for the different nanorods and is presented in Fig. 1.8. As previously mentioned, increasing the AR induces a redshift of the resonance wavelength λ_2. More importantly, σ_{ext} also increases with increasing AR. This enhancement of the optical extinction becomes even more pronounced for nanorods with larger radii. These observations can be explained by the fact that nanorods with higher ARs exhibit stronger absorption and scattering of the incident light, leading to a greater extinction of the incoming photons compared to smaller nanorods [54, 72, 73]. This trend is consistent with Huang *et al.* [68]. Since increasing either the AR (at fixed radius) or the radius (at fixed AR) increases the overall gold volume of the nanorod, this directly accounts for the systematic rise in σ_{ext} observed in the simulations. Furthermore, Huang *et al.* emphasize that as the nanoparticle size increases, the relative contribution of scattering to the total extinction grows faster than that of absorption [68], which is in line with the more pronounced extinction enhancement obtained for the largest-radius nanorods, where the scattering contribution is expected to become non-negligible compared to absorption.

The influence of the AR on the scattering, absorption, and extinction cross-sections at resonance λ_2 is shown in Fig. 1.9. An increase in AR leads to larger cross-sections for all three optical processes. This effect becomes even more pronounced for nanorods with larger radii, as discussed previously.

Electrical field: E_{max} and $\langle M \rangle$

The surface-averaged LFIEF $\langle M \rangle$, is shown in Fig. 1.10. In contrast to the extinction cross-section, the LFIEF does not increase with the nanorod radius. Furthermore, for a fixed radius, the surface averaged EF tends to reach a plateau for AR values above approximately 3. This behavior can be explained by the definition of the LFIEF, which averages the enhancement over the nanoparticle surface area; as the nanorod dimensions increase, the particle surface area also increases, thereby reducing the average enhancement. This saturation does not apply to the maximum electric field enhancement. As shown in Fig. 1.11, the highest electric field enhancement is obtained for nanorods with small radii, while the intensity increases with increasing AR.

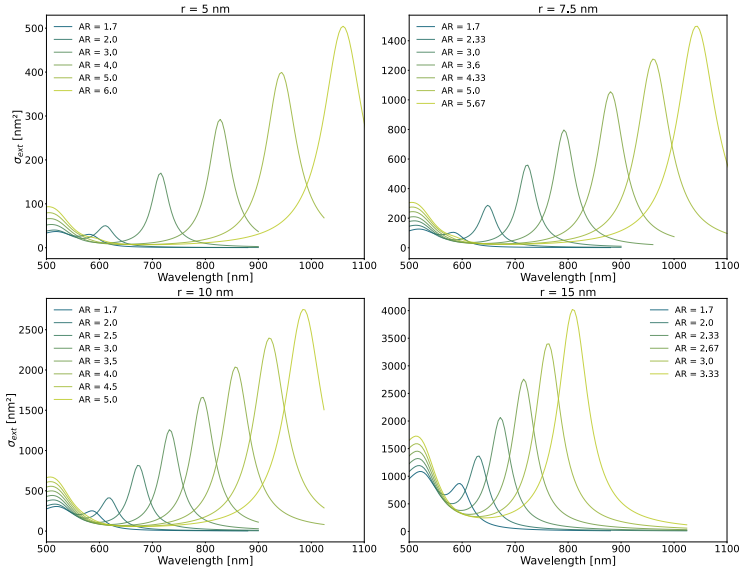


Fig. 1.8 Simulated extinction cross-section as a function of the wavelength for nanorods with radii ranging from 5 to 15 nm. The color of the line varies from blue (AR = 1.7) to green (AR = 6).

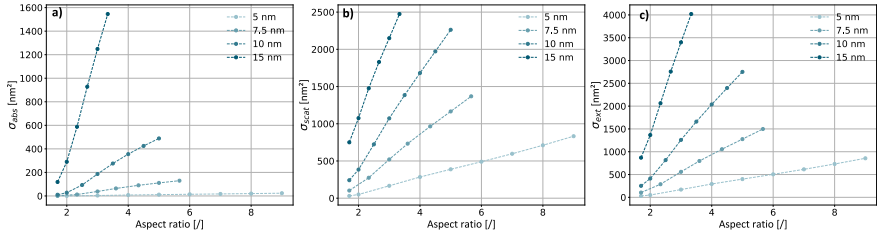


Fig. 1.9 Impact of the AR on the a) absorption cross-section, b) scattering cross-section and c) extinction cross-section for NRs with radii ranging from 5 nm (light blue) to 15 nm (dark blue).

The numerical simulations also reveal a slight λ_2 resonance shift between the extinction cross-section, the surface-averaged LFIEF, and the maximum electric field enhancement, as illustrated in Fig. 1.12. However, this redshift remains smaller than 4 nm, indicating that the electromagnetic enhancement closely follows the extinction behavior. Consequently, strong optical extinction is associated with strong electromagnetic enhancement, in agreement with the observations reported by van Dijk *et al.* [74].

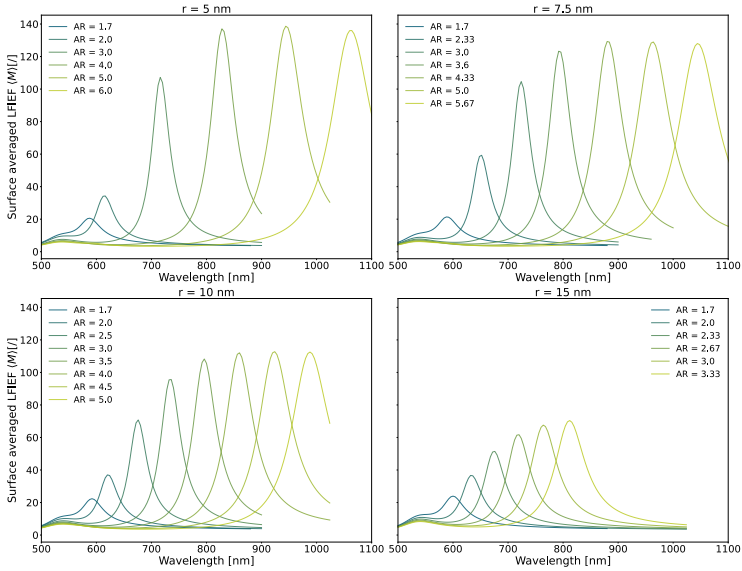


Fig. 1.10 Simulated surface averaged enhancement factor as a function of the wavelength for nanorods with radii ranging from 5 to 15 nm with increasing AR. The y-axis scale is identical for all four graphs.

Wrap-up on the influence of nanorod AR and size

For an isolated nanorod, the optical cross-sections were observed to increase with the AR, and this increase becomes even more pronounced for larger nanorod radii. Concerning the maximum electromagnetic field enhancement, higher aspect ratios also lead to stronger local fields but smaller radii show higher electric fields. The evolution of the averaged enhancement factor $\langle M \rangle$ is more complex. Although it follows the same trend as the maximum electromagnetic field enhancement, a saturation effect progressively appears. This behavior can be explained by the normalization over the nanoparticle surface area, which increases for larger nanoparticles and therefore limits the overall gain in the averaged enhancement factor.

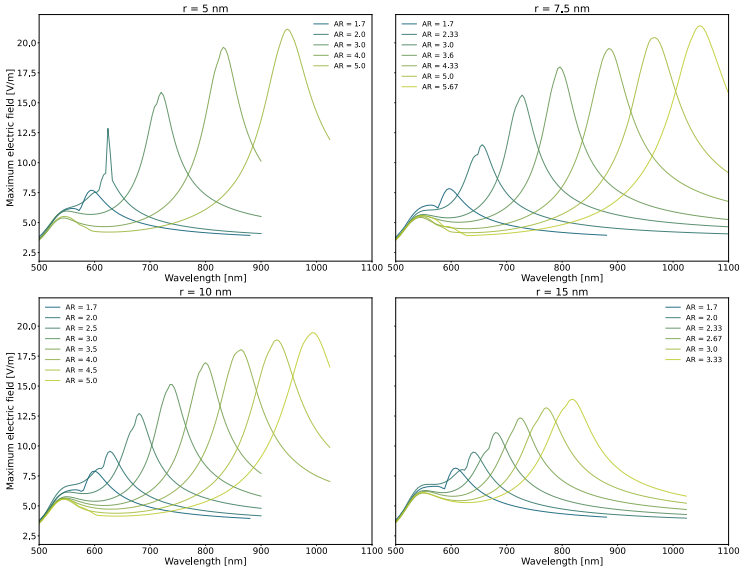


Fig. 1.11 Simulated maximum value of the electric field [V/m] as a function of the wavelength for nanorods with radii ranging from 5 to 15 nm with increasing AR. The y-axis scale is identical for all four graphs.

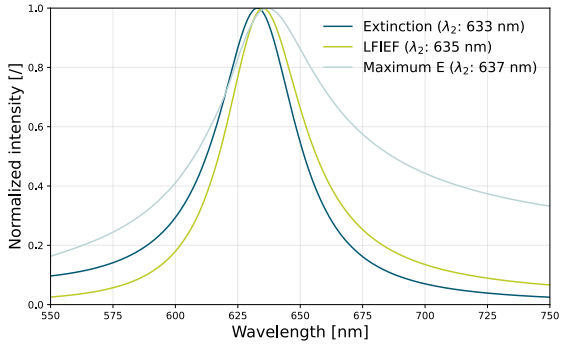


Fig. 1.12 Normalized simulated extinction cross-section (blue), surface averaged LFIEF (green) and the maximum electric field (light blue) versus the wavelength for a nanorod with a radius of 5 nm and a cylinder length of 15 nm in water.

1.4.2 Dimer configuration

Another important parameter to investigate for these nanorods is the influence of nanoparticle coupling on both the resonance wavelength and

the electromagnetic enhancement. To this end, dimers composed of two nanorods with a radius of 5 nm and a cylinder length of 15 nm, separated by a gap distance of 2.5 nm, were analyzed in four different configurations, as illustrated in Fig. 1.13.
The electromagnetic coupling between neighboring plasmonic nanostructures is known to modify both the local electric-field distribution and the spectral position of the plasmon modes [75, 76].

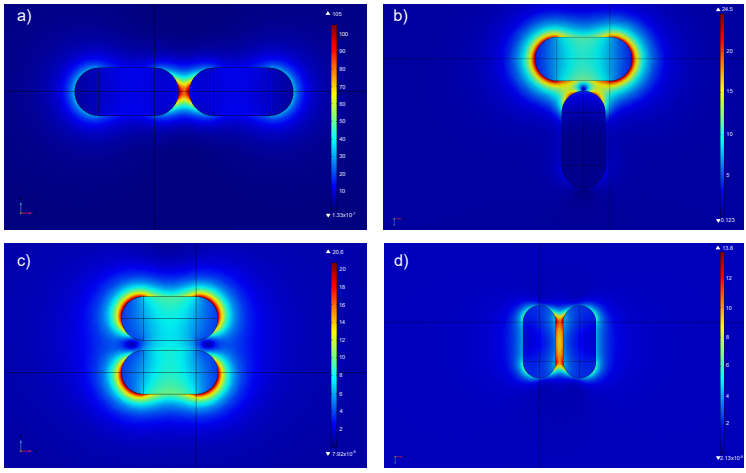


Fig. 1.13 Four hotspot configurations formed by two nanorods with a radius of 5 nm and a cylinder length of 15 nm separated by a gap distance of 2.5 nm. The norm of the electric field intensity is shown for each configuration at its respective resonance wavelength. The xz-plane is displayed in each graph and the incident electric field is a plane wave propagating along the z-axis with an amplitude of 1 V/m and polarized along the x-axis; **a)** Longitudinal configuration, resonating at 675 nm, with a maximum electric field of 110.6 V/m; **b)** Perpendicular configuration, resonating at 640 nm, with a maximum electric field of 26.1 V/m; **c)** Parallel configuration, resonating at 610 nm, with a maximum electric field of 21.7 V/m; **d)** Transverse configuration, resonating at 550 nm, with a maximum electric field of 14.9 V/m.

Among the four configurations investigated, the longitudinal arrangement shown in Fig. 1.13a produces the strongest electromagnetic enhancement. In this configuration, the electric field is concentrated in the gap between the two nanorod tips, resulting in a pronounced hotspot. The corresponding

longitudinal resonance occurs at $\lambda_2 = 675$ nm, with a maximum electric field of 110.6 V/m and a surface-averaged LFIEF $\langle M \rangle$ of 91. In comparison, the parallel and perpendicular configurations shown in Fig. 1.13b and c yield significantly lower surface-averaged LFIEFs of 189 and 190, respectively, while the transverse configuration in Fig. 1.13d reaches only 26. This strong field localization in the gap is consistent with the formation of bonding longitudinal modes in coupled nanorod structures, for which the electric-field maximum is concentrated toward the interparticle gap [76].

The formation of nanorod dimers also induces significant shifts in the resonance wavelength λ_2. A single nanorod, in this case, exhibits a longitudinal resonance at 634 nm. In contrast, configurations (a) and (b) produce a redshift of the resonance wavelength, with λ_2 values of 675 nm and 640 nm, respectively. On the other hand, configurations (c) and (d) induce a blueshift, leading to resonance wavelengths of 610 nm and 550 nm, respectively. These results demonstrate that the spectral modification induced by interparticle coupling depends strongly on the relative orientation of the nanorods and the associated plasmonic mode. Similar spectral shifts and modifications of the local electromagnetic field have been reported for interacting gold nanorods [75], while studies of nanowire dimers have further shown that coupling can lead to the splitting of longitudinal plasmon modes into bonding and antibonding modes [76].

Figure 1.14 presents the effect of the interparticle distance on both the resonance wavelength λ_2, and the surface-averaged LFIEF $\langle M \rangle$, for the dimer configuration shown in Fig. 1.13a. An infinite separation distance corresponds to the case of an isolated nanorod. As the separation increases, both the electromagnetic enhancement and the resonance shift progressively approach the values of the isolated nanorod, indicating a reduction in interparticle coupling. Beyond approximately 30 nm, $\langle M \rangle$ and λ_2 exhibit only limited variation with further increases in the separation distance, suggesting that the electromagnetic interaction between the nanorods becomes negligible. This corresponds to the distance-dependence for nanospheres relation as explained by Verdin *et al.* [31], where $\mathrm{EF} \propto (1 + \frac{distance}{radius})^{-10}$.

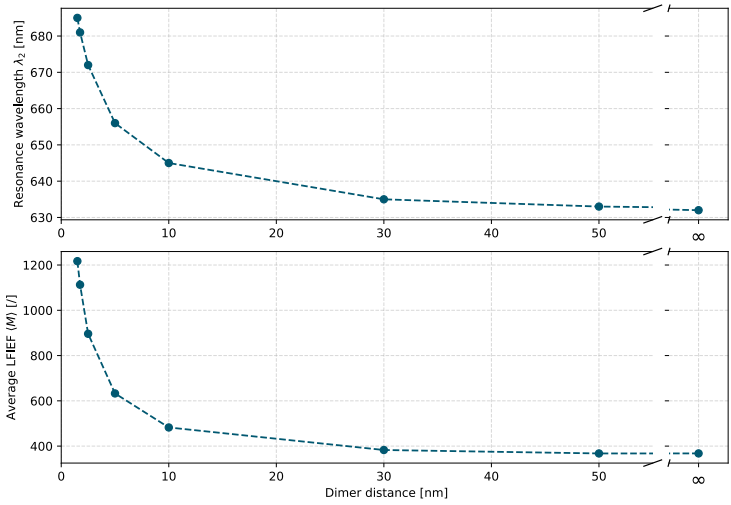


Fig. 1.14 Simulations of the resonant wavelength λ_2 and the average enhancement factor $\langle M \rangle$ as a function of the distance between the two NRs shown in Fig. 1.13a.

1.4.3 Comparison with experimental measures

Louise Lejeune synthesized twelve different gold nanorod suspensions, referred to as NR1 to NR12 according to their longitudinal resonance wavelength λ_2, ranging from 600 nm (NR1) to 1000 nm (NR12). Transmission Electron Microscopy (TEM) images of these twelve nanorod suspensions are shown in Fig. 1.15 and were used to determine their dimensions and aspect ratios (AR). As expected from the simulations presented in Fig. 1.7, the nanorods resonance wavelength λ_2 increases with the AR. The size, resonance wavelength λ_2 and AR determined by TEM images of the twelve NRs are listed in Table 1.1 and Table 1.2.

Based on these TEM images, the nanorod dimensions were determined and are summarized in Table 1.1. The twelve nanorods were subsequently simulated using the same COMSOL model, and their geometries are shown in Fig. 1.16.

Because the nanorods are freely dispersed in the liquid phase, their orientations are not fixed and can be considered randomly distributed. Con-

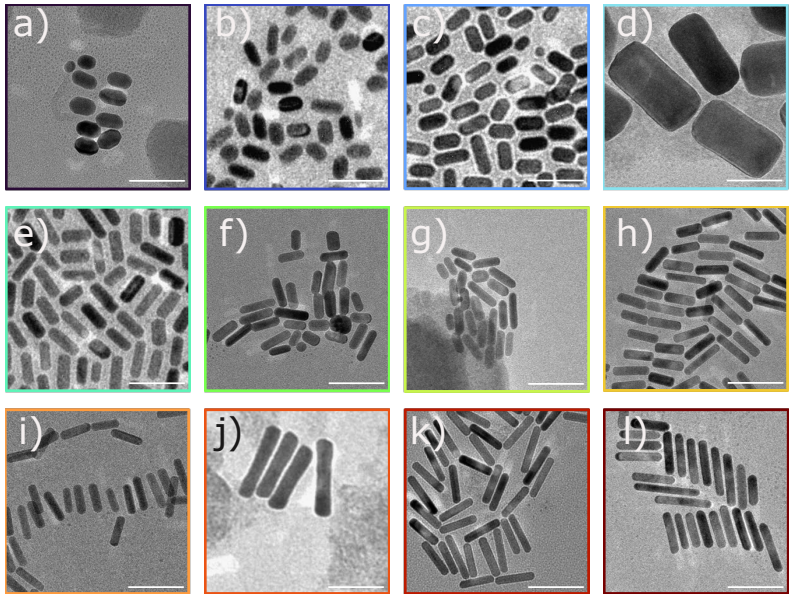


Fig. 1.15 TEM images of dried suspensions of **a)** NR1, **b)** NR2, **c)** NR3, **d)** NR4, **e)** NR5, **f)** NR6, **g)** NR7, **h)** NR8, **i)** NR9, **j)** NR10, **k)** NR11 and **l)** NR12. The scale bar represents 50 nm. Increase in the aspect ratio of the gold nanorods synthetized can be appreciable from left to right and from top to bottom. Colored frame in accordance with the legend in the following figures.

Name	Length [nm]	Radius [nm]	AR [/]
NR1	8.9	7.05	1.7
NR2	8	5.5	1.7
NR3	13.3	5.35	2.3
NR4	30	15	2.6
NR5	16.9	5.05	2.8
NR6	14.9	4.05	2.8
NR7	16	4	3.1
NR8	22.1	3.95	3.8
NR9	22.3	3.85	4.0
NR10	49.3	6.35	4.9
NR11	28	3.5	5.1
NR12	34.1	3.95	5.4

Table 1.1 Mean length and radius parameters for each simulated NR.

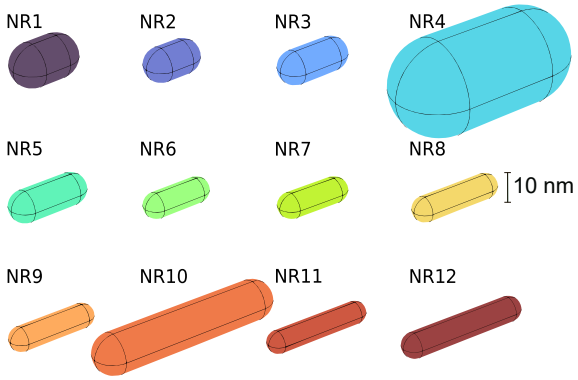


Fig. 1.16 Schematic representation of the 12 nanorods prepared based on the TEM-measured average, scale bar represents 10 nm.

sequently, neither the longitudinal nor the transverse plasmon mode is preferentially excited during the Raman measurements. As previously shown in Fig. 1.6, the nanorod orientation does not affect the positions of λ_1 or λ_2, but only modifies the resonance intensity. Therefore, in the simulations, the angle between the nanorod axis and the electric field vector was fixed at 50° in order to compare all nanorods under identical excitation conditions and be able to simulate the longitudinal and transverse modes.

Comparison of the extinction and λ_2

The experimentally measured and simulated optical properties of the nanorods are compared in Fig. 1.17, where the UV-Vis-near-infrared extinction spectra are presented together with the simulated extinction cross-sections calculated from the dimensions measured on the TEM images. The experimental values of λ_2 show good agreement with the simulated ones. To allow a direct comparison, the simulated extinction cross-sections were normalized by the nanorod volume, resulting in equivalent cross-section values at 400 nm. This normalization is necessary because both the scattering and absorption cross-sections increase approximately linearly with the aspect ratio, with the effect becoming even more pronounced for larger nanorod radii, as shown in Fig. 1.9. Volume normalization therefore enables a meaningful comparison between the experimental extinction spectra and the simulated extinction cross-sections, thereby validating the simulation model.

Overall, the simulated extinction spectra closely reproduce the experimentally measured spectra. In particular, the relative increase in extinction intensity at λ_2 with increasing AR is consistent between simulations and experiments. Small discrepancies are nevertheless observed between the measured and simulated resonance wavelengths, as summarized in Table 1.2. These differences may arise from the fact that the simulations consider a single idealized nanorod in water with average dimensions extracted from TEM images, whereas the experimental suspensions contain a distribution of nanorod sizes and aspect ratios. In addition, factors such as surface roughness, agglomeration and faceting may also influence the plasmon resonance position [77].

Name	$\lambda_{2,UV-vis}$ [nm]	$\lambda_{2,COMSOL}$ [nm]	AR [/]
NR1	594	579	1.7
NR2	623	587	1.7
NR3	637	631	2.3
NR4	645	635	2.6
NR5	676	679	2.8
NR6	718	696	2.8
NR7	732	715	3.1
NR8	787	795	3.8
NR9	815	812	4.0
NR10	883	927	4.9
NR11	942	936	5.1
NR12	1023	975	5.4

Table 1.2 Comparison between the measured λ_2 by UV-vis and the simulated λ_2.

This behavior is further confirmed in Fig. 1.18, where Eq. 1.7 is compared with the simulated values of λ_2 obtained for various aspect ratios while considering different nanorod radii (5 nm, 7.5 nm, 10 nm, and 15 nm). Equation 1.7, established statistically by Engel *et al.* [70], describes the linear relationship between λ_2 and the aspect ratio of gold nanorods. For small aspect ratios (AR<6), Eq. 1.7 shows good agreement with the simulations, which is particularly relevant here since the biggest AR (5.4) is smaller than 6.

$$\lambda_2 = 97 * AR + 436. \tag{1.7}$$

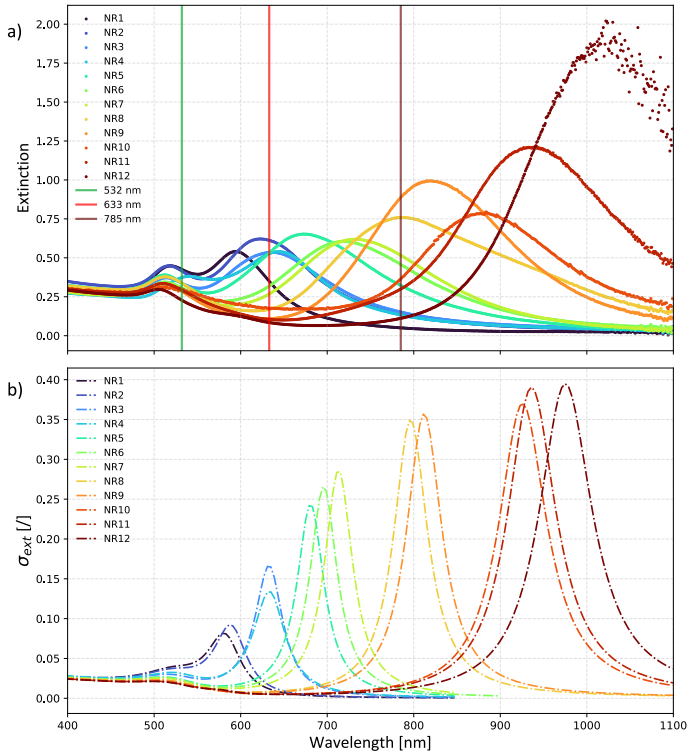


Fig. 1.17 **a)** UV-vis-NIR extinction spectra of the 12 NRs suspensions labelled with 2.5×10^{-7} mol/L MGITC prepared to have an extinction of 0.32 at 400 nm. The three vertical lines represent the position of the 3 different lasers (532 nm in green, 633 nm in red and 785 nm in dark crimson red) used in Raman experiments as references. **b)** Simulated extinction cross-sections of a single nanorod with a size corresponding to the TEM-measured average of the 12 NRs suspensions, normalized by its volume with an orientation of 50° to excite both longitudinal and transverse modes.

Comparison of electrical field enhancement

Now that the resonance wavelength and the extinction spectra of the nanorods have been compared, it is of interest to relate the simulated electromagnetic enhancement to the measured SERS intensity. Nevertheless, it should be kept in mind that these two quantities are not strictly equivalent, since the SERS intensity depends on phenomena that are more complex than the electric field enhancement alone.

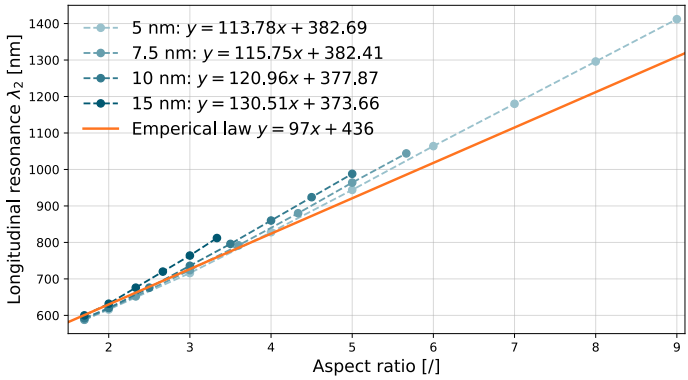


Fig. 1.18 Simulated evolution of λ_2 versus the AR. The equation of each linear fit is shown in the legend for each radius. The orange slope shows the empirical law established by Engel *et al.* [70].

The electromagnetic field enhancement is commonly evaluated using the maximum electric field intensity at the nanoparticle surface. However, in the present study, it is more appropriate to consider the surface averaged LFIEF $\langle M \rangle$ rather than relying solely on the maximum electric field enhancement. This choice is motivated by the intrinsic heterogeneity of colloidal suspensions: the measured SERS enhancement is not spatially uniform, and MGITC (a widely used Raman reporter dye that binds to gold nanoparticles through its isothiocyanate group) molecules are not necessarily located at positions corresponding to the highest electromagnetic fields, such as the nanorod tips. For this reason, we propose to use the surface averaged LFIEF $\langle M \rangle$ introduced by Grand *et al.* [66] to characterize the intensity of the largest field enhancement on the NP surface and how strongly localized it is.

To evaluate the relevance of this approach, the normalized SERS intensity was compared with the two measures of the electromagnetic enhancement squared corresponding to the $|E|^4$ rule explained in eq. 1.3. First with the squared maximum electric field intensity (Fig. 1.19). Next with the square of the surface-averaged enhancement factor, $\langle M \rangle^2$, derived from eq. 1.4 (Fig. 1.20).

At excitation wavelengths of 532 nm and 633 nm, the surface-averaged

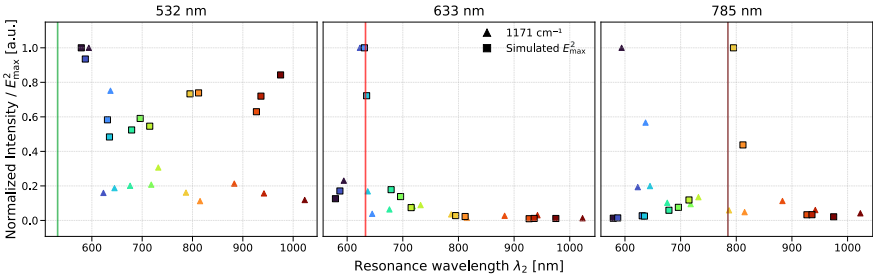


Fig. 1.19 Normalized MGITC SERS intensity measured at 1171 cm-1 (triangles) at the three different excitation wavelengths compared with the squared normalized simulated maximum electric field (square) in function of the longitudinal resonance wavelength λ_2 of the nanorods. The same y-axis scale is used for all three panels.

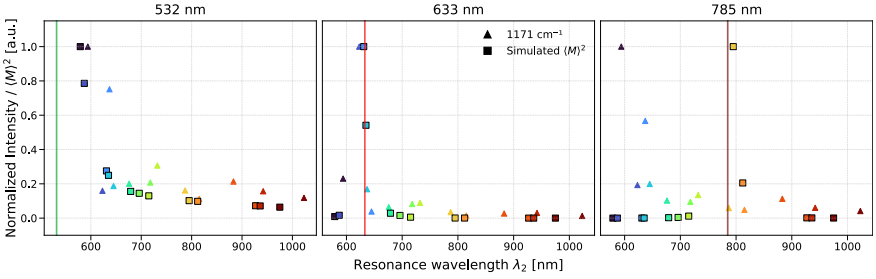


Fig. 1.20 Normalized MGITC SERS intensity measured at 1171 cm-1 (triangles) at the three different excitation wavelengths compared with the squared normalized simulated surface averaged LFIEF $\langle M \rangle$ (square) in function of the longitudinal resonance wavelength λ_2 of the nanorods. The same y-axis scale is used for all three panels.

enhancement factor exhibits significantly better agreement with the experimental measurements than the maximum electric field enhancement. Nevertheless, at an excitation wavelength of 785 nm, both simulation approaches overestimate the enhancement observed experimentally for NR8 and NR9, the nanorods whose plasmon resonance are closest to the excitation wavelength. In this case, the COMSOL simulations fail to fully reproduce the experimental behavior, suggesting that additional physical effects not included in the model significantly influence the measured SERS enhancement.

A similar discrepancy is observed experimentally: nanorods with smaller

longitudinal plasmon resonance wavelengths, corresponding to lower aspect ratios, exhibit stronger Raman enhancement regardless of the excitation wavelength, λ_0.

At first glance, this observation appears to contradict the commonly accepted rule stating that optimal SERS enhancement is achieved when the LSPR wavelength matches the excitation wavelength [78, 79, 80, 81]. This expected behavior is indeed reproduced by the COMSOL simulations. Specifically, the simulations predict that the most efficient nanorods are NR1 for λ_0 = 532 nm, NR3 and NR4 for λ_0 = 633 nm, and NR8 for λ_0 = 785 nm, since their respective resonance wavelengths (579 nm, 631 nm, 635 nm, and 795 nm) are the closest to the excitation wavelengths.

Nanorods with smaller aspect ratios, particularly NR1 (AR=1.6), NR2 (AR=1.9), and NR3 (AR=2.1), possess plasmon resonances close to the excitation wavelengths of 532 nm and 633 nm, in agreement with both the simulations and the experimental measurements within this spectral range. However, under 785 nm excitation, these nanorods exhibit resonance wavelengths that are significantly blueshifted relative to the laser wavelength, unlike NR8 and NR9, whose resonance wavelength are nearly matched to λ_0.

One possible explanation for the discrepancy between the simulations and the experimental results is a resonance shift induced by interparticle coupling and the formation of electromagnetic hotspots. As discussed previously about the dimers, different nanorod dimer configurations can induce either redshifts or blueshifts of the plasmon resonance wavelength. However, in the present study, the measurements were performed in dilute colloidal suspensions, where the nanorods are assumed to be homogeneously dispersed. Furthermore, no aggregation was detected in the UV-Vis spectra.
This demonstrates that the electromagnetic enhancement calculated from the local field alone is not sufficient to accurately model the SERS intensity of nanorods in colloidal suspensions. Additional phenomena, such as extinction effects, nanoparticle concentration, and light propagation through the suspension, must also be taken into account to obtain a more realistic description of the experimental SERS response.

1.4.4 SERS modelisation of nanorod suspensions

As discussed by van Dijk *et al.* [74] and Sivapalan *et al.* [82], SERS measurements performed in colloidal suspensions of gold nanospheres and nanorods must account for the extinction of the excitation laser, arising from both absorption and scattering by the nanoparticles themselves. In contrast, this effect is generally negligible for measurements conducted on dried substrates.

Sivapalan and van Dijk revealed that for an excitation wavelength of 785 nm, the most efficient nanorod enhancers are those whose longitudinal plasmon resonance is blueshifted relative to the excitation wavelength, corresponding to nanorods with smaller aspect ratios. In contrast, Guo *et al.* [78] observed at an excitation wavelength of 633 nm that gold nanorods exhibited the strongest SERS response when their plasmon resonance was positioned close to the excitation source. The results obtained in the present work help clarify this apparent discrepancy, by investigating three different excitation wavelengths (532 nm, 633 nm, and 785 nm).

The spectral positions of the extinction maximum and the electromagnetic enhancement are closely related (see Fig. 1.12). However, an important distinction arises when considering their dependence on nanorod dimensions. As shown in Fig. 1.10, the intensity of the surface-averaged LFIEF $\langle M \rangle$ does not increase with nanorod radius, in contrast to the extinction cross-section (see Fig. 1.8). Furthermore, for a fixed radius, the electromagnetic enhancement $\langle M \rangle$ tends to reach a plateau for aspect ratios above approximately 3; showing that the extinction and the electromagnetic field enhancement do not evolve in the same way with increasing nanoparticle size, while the extinction cross-section has also been shown to play an important role in the resulting SERS intensity.

The model introduced by van Dijk *et al.* [74], developed at first for gold nanospheres, enables to correctly estimate the SERS signal in colloidal suspension. The Raman intensity is, in their work, not only determined by the local electromagnetic enhancement G, but by also considering the extinction losses within the suspension (absorption and scattering of the gold nanoparticles). The Eq. 1.8 stands for the Raman reflection mode (mode used in our Raman setup):

$$R = \langle N \rangle A R^{(0)} G \frac{1 - e^{-hm\rho[C_{ext}(\omega)+C_{ext}(\omega_0)]}}{m\,[C_{ext}(\omega) + C_{ext}(\omega_0)]}, \tag{1.8}$$

where $\langle N \rangle$ is the average number of molecules, A the integral over the transverse beam profile, $R^{(0)}$ the Raman signal without nanoparticles, h the sample thickness, m the refractive index of the medium, ρ the concentration of the gold nanoparticles, C_{ext} the extinction cross-section at the frequency of the incident laser (ω_0) and at the Raman scattered frequency (ω) and G is the enhancement factor defined by van Dijk as:

$$G(\omega, \omega_0) = \left| (1 + 2\frac{n_s^2(\omega) - n^2(\omega)}{n_s^2(\omega) + 2n^2(\omega)}) \cdot (1 + 2\frac{n_s^2(\omega_0) - n^2(\omega_0)}{n_s^2(\omega_0) + 2n^2(\omega_0)}) \right|^2, \tag{1.9}$$

where n is the refractive index of the medium and n_s is the refractive index of the nanospheres.

In the work of van Dijk *et al.* [74] and Sivapalan *et al.* [82] the extinction cross-section is derived analytically within the dipolar approximation for spheroidal nanoparticles.
In this work, both analytical expressions of G and C_{ext} are replaced with numerically computed quantities obtained from COMSOL simulations at 3 different wavelengths (532, 633 and 785 nm). For each individual nanorod geometry, the extinction cross-section and surface-averaged field intensity enhanemecnt factor $\langle M \rangle$ are calculated at the frequency of the incident laser (ω_0) and at the Raman scattered frequency (ω). This numerical approach enables a self-consistent determination of both the extinction cross-section and the electromagnetic enhancement for each specific nanorod geometry studied. In contrast to the analytical spheroidal model, where the enhancement G follows a fixed dipolar expression and depends only on the dielectric function, the COMSOL-based implementation explicitly accounts for geometry-dependent field redistribution. This extends the framework from an analytical description limited to spheroids to a fully numerical model applicable to nanoparticles of arbitrary shape.

Fig. 1.21a compares the analytical and numerical models for a gold nanosphere in water and highlights the small differences between the two approaches. As observed, the calculated extinction cross-sections are nearly identical, while a slight shift is present between G and $\langle M \rangle$. The effect of these small

variations on the SERS intensity is presented in Fig. 1.21b.
A blueshift of less than 20 nm is observed, with the resonance shifting from 565 nm in the analytical model to 546 nm in the numerical model. These results validate the use of numerically calculated parameters in Eq. 1.8, thereby extending its applicability to nanoparticle geometries more complex than simple spheres.

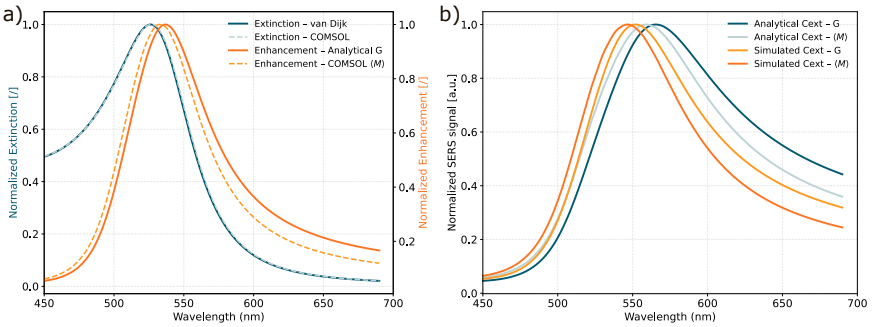


Fig. 1.21 **a)** Normalized extinction cross-section of a gold nanosphere with a radius of 6 nm in water as a function of the incident wavelength, comparing the analytical model of van Dijk [74] (solid blue line) with the numerical COMSOL simulation (dashed blue line). The normalized Raman enhancement for the same nanoparticle is also shown as a function of the incident wavelength, comparing the analytical model (solid orange line) with the numerical COMSOL surface-averaged model (dashed orange line), calculated for a Raman shift at 1171 cm^{-1}. **b)** Predicted normalized SERS signal in reflection mode as a function of the incident wavelength for a gold nanosphere with a radius of 6 nm in water, evaluated for a Raman shift of 1171 cm^{-1}. The calculations were performed for a nanoparticle concentration of 2 nM and a sample thickness of 2 cm, using the different models presented in panel (a).

In colloidal systems, the measured SERS intensity is therefore governed by a balance between electromagnetic enhancement and optical extinction. This interplay is illustrated in Fig. 1.22, which presents the results of Eq. 1.8 for nanorods of varying radii (5–15 nm) and aspect ratios, alongside the experimentally measured SERS intensities (diamond markers). The experimental data fall within the envelope defined by the simulations, reflecting the intrinsic size dispersity of the nanorod samples. For meaningful comparison, the simulated intensities were fitted such that their maximum

matched the maximum experimental intensity.

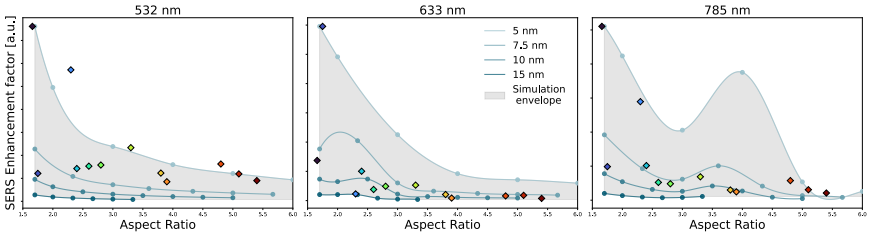


Fig. 1.22 Simulated SERS enhancement factor as a function of nanorod aspect ratio (AR) for excitation wavelengths of 532 nm, 633 nm, and 785 nm. Solid lines show the cubic interpolation in between the simulation points for different radii (5 nm (light blue) to 15 nm (dark blue)). The grey shaded region indicates the simulation envelope. The diamond markers show the experimentally measured SERS intensities for the corresponding 12 NRs.

This analysis confirms that nanorods with smaller aspect ratios yield higher SERS intensities, in agreement with experimental observations. Importantly, the model also indicates that, at an excitation wavelength of 785 nm, nanorods with an aspect ratio around 4 and a small diameter represent a promising compromise between enhancement and extinction.

Consequently, nanorod suspensions exhibiting higher extinction lead to a reduction in the effective light intensity available for both excitation and Raman scattering processes. This behavior arises from the fact that nanorods with higher aspect ratios more efficiently absorb and scatter both incident photons (from the excitation laser) and scattered photons (from the analyte), thereby increasing overall optical losses and diminishing the measurable SERS signal.

1.4.5 Discussion

From these considerations, it can be concluded that the optimal SERS enhancement in colloidal nanorod suspensions is not governed solely by the spectral overlap between the longitudinal plasmon resonance λ_2 and the excitation wavelength λ_0, but rather by a balance between nanoparticle size and aspect ratio. In particular, nanorods with smaller aspect ratios

and reduced radii provide the best compromise: they ensure a sufficient increase in the average electromagnetic field while minimizing extinction losses in the medium. This also explains why smaller aspect ratio nanorods, whose λ_2 values are naturally closer to lower excitation wavelengths such as 532 nm and 633 nm, appear as efficient enhancers, in agreement with the observations of Guo *et al.* [78].

Overall, determining the optimal nanorod geometry for a given excitation wavelength remains a delicate task, as it strongly depends on the measurement environment; namely, whether the SERS experiment is performed in colloidal solution or on a dried substrate.
In liquid phase, the SERS response is governed by a subtle balance between electromagnetic enhancement and optical extinction. It is often advantageous to employ nanorods whose longitudinal plasmon resonance λ_2 is slightly blueshifted relative to the excitation wavelength λ_0, as this configuration reduces the extinction cross-section.
In contrast, in the solid state, where nanoparticles are immobilized, the formation of electromagnetic hotspots dominates the SERS enhancement. In such configurations, plasmonic coupling between closely spaced nanorods induces a redshift of the resonance wavelength, as illustrated in Fig. 1.14. These contrasting behaviors highlight the importance of considering both nanoparticle environment and collective effects when designing plasmonic systems for SERS applications.

1.5 Nanodumbbells

The concept of this geometry originated from the simulations performed on gold nanorods, which highlighted that the strongest electromagnetic enhancement was localized at the nanorod tips. This observation motivated the idea of increasing the size of these highly enhanced regions by enlarging the extremities of the nanorod, leading to the development of the so-called nanodumbbell geometry. This approach was also inspired by the work on nano-antennas that break the symmetry [50, 49]. Louise Lejeune synthesized several nanodumbbell suspensions, examples of which are shown in Fig. 1.23b and c. One of the advantages of this synthesis method is that nanodumbbells can be produced from various nanorod seeds while

independently controlling the growth of the outer spherical extremities. The synthesis is adapted from the deposition of palladium on the tips of gold nanorods [83].

The same COMSOL model as previously developed for nanorods is used to simulate the optical response of nanodumbbells in order to investigate the influence of the enlarged extremities. The nanodumbbell geometry implemented in COMSOL is illustrated in Fig. 1.23a. Similar to the nanorod geometry, the structure consists of a cylinder connected to two spheres. However, in this case, the radii of the outer spheres differ from that of the cylinder. The geometry is therefore defined by three parameters: the cylinder radius r, the cylinder length L, and a factor k, corresponding to the ratio between the radius of the outer spheres and the cylinder radius. The aspect ratio, defined as the ratio between the longitudinal and transverse dimensions of the nanoparticle, is thus given by: $AR = \frac{2rk+L}{2r}$.

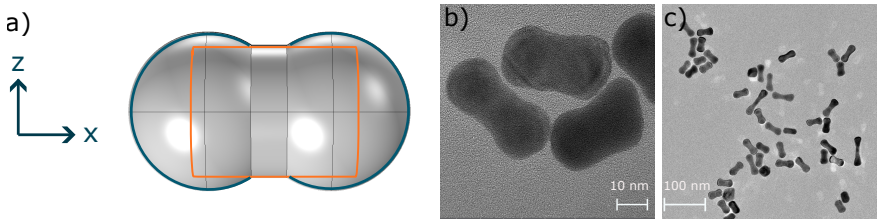


Fig. 1.23 a) Schematic representation of the COMSOL nanodumbbell geometry with a cylinder radius of 5 nm, a cylinder length of 25 nm, and a shape factor $k = 1.2$. The outlines of the two outer spheres are shown in blue, while the cylindrical section is shown in orange. The nanodumbbell is oriented along the x-axis. b) TEM image of dried nanodumbbell suspension. Scale bar: 10 nm. c) TEM image of dried nanodumbbell suspension. Scale bar: 100 nm.

1.5.1 Results

By increasing the k factor of a nanodumbbell, as shown in Fig. 1.24, the AR of each dumbbell increases linearly with the resonance wavelength λ_2. In this figure, each line represents a family of nanodumbbells derived from the same nanorod seed geometry. Along a given line, each marker corresponds to an increasing k factor, with the leftmost marker representing the initial

nanorod seed. The color of each line indicates the radius of the nanorod seed, while the marker shape represents its initial aspect ratio. This increase is expected, since nanoparticles with larger aspect ratios are associated with a redshift of λ_2.

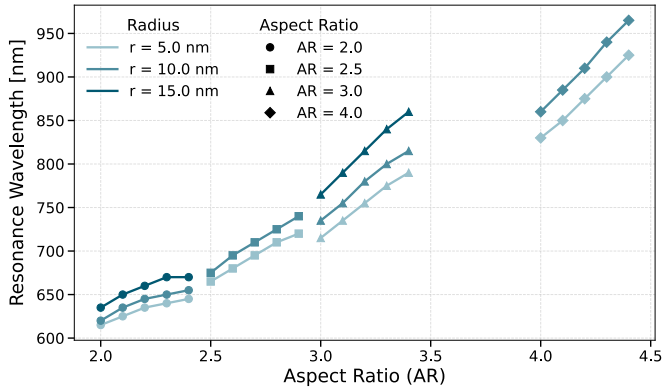


Fig. 1.24 Evolution of the resonance wavelength as a function of the AR for different nanodumbbells. Each line corresponds to a dumbbell with an increasing k factor. Darker blue colors indicate larger cylinder radii (from 5 to 15 nm). The markers show the AR of the corresponding nanorod seed (k = 1).

The influence of the dumbbell size on the electric-field enhancement is, however, more difficult to analyze. As shown in Fig. 1.25b, the maximum electric-field intensity does not always increase linearly with the k factor. For small dumbbells (AR < 3), increasing the size of the outer spheres leads to a stronger electric field. In contrast, for larger dumbbells (AR > 4), the electric field decreases as the k factor increases.
When considering the surface averaged LFIEF $\langle M \rangle$, shown in Fig. 1.25a, not only the electric-field intensity but also the extent of the "hot" surface region must be taken into account. Those two parameters increase simultaneously only for small dumbbells (AR < 3). For larger dumbbells, enlarging the outer spheres reduces the electric-field intensity while increasing the total surface area, resulting in a decrease of the surface averaged LFIEF $\langle M \rangle$. It can therefore be concluded that the nanodumbbell geometry is mainly beneficial for small nanorod seeds (AR < 3).

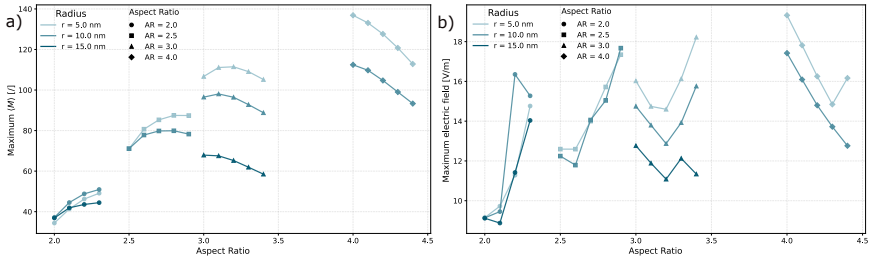


Fig. 1.25 a) Evolution of the maximum surface averaged LFIEF $\langle M \rangle$ at the resonance wavelength as a function of the AR for different dumbbells. b) Evolution of the maximum electric field [V/m] at the resonance wavelength as a function of the AR for different dumbbells. Each line corresponds to a dumbbell with an increasing k factor. Darker blue colors indicate larger cylinder radii (from 5 to 15 nm). The markers indicate the aspect ratio of the corresponding nanorod seed ($k = 1$).

1.5.2 SERS modelisation of nanodumbbell suspensions

As explained in the nanorod section, in colloidal systems, the measured SERS intensity is governed by a balance between electromagnetic enhancement and optical extinction. The SERS enhancement is shown in Fig. 1.26, which presents the results of Eq. 1.8 for nanodumbbells of varying radii (5–15 nm) and aspect ratios, with growing k factors. As can be seen, the nanodumbbells that have the highest SERS EF, are the dumbbells with the seeds that have the smallest radius (5 nm in light blue). And an optimum seems to be either with nanodumbbells that have a high k factor starting with a seed with AR = 2 or nanodumbbells with small k factor and AR close to 2.5, this can be explained by the fact that the resonance of those nanodumbbells is close to the excitation wavelength at 633 nm, but it also needs to be remembered that the larger the nanoparticle, the higher the extinction cross section and thus the lower the SERS enhancement. A trade-off is thus needed.

1.5.3 Discussion

Nanodumbbells constitute an appealing class of nanostructures for SERS applications, as they combine a geometrical configuration that is both physically promising and experimentally accessible. From a synthesis perspective, these structures are particularly attractive because they can be grown from a

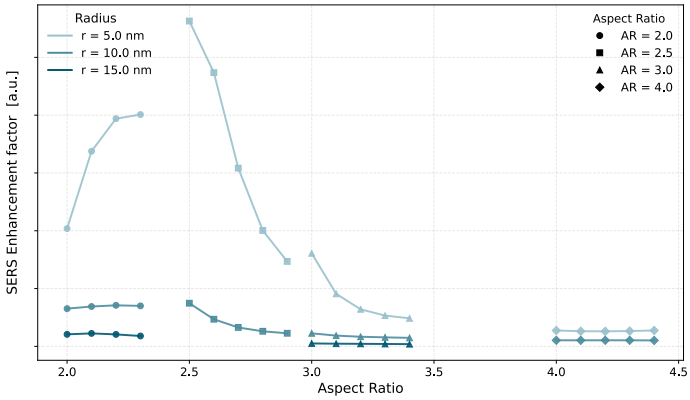


Fig. 1.26 Simulated SERS enhancement factor as a function of the nanodumbbell aspect ratio for an excitation wavelength of 633 nm. Each line corresponds to a dumbbell with an increasing k factor. Darker blue colors indicate larger cylinder radii (from 5 to 15 nm). The markers indicate the aspect ratio of the corresponding nanorod seed ($k = 1$).

wide range of nanorod seeds. This versatility allows their optical properties to be tuned through the initial nanorod geometry, while the subsequent formation of the two outer lobes remains relatively straightforward compared to more complex nanostructures [83].

From an optical standpoint, the presence of the two outer spheres is expected to modify the local electromagnetic field distribution. However, the precise role of these outer features remains difficult to isolate. This challenge is further compounded by the fact that the numerical results obtained in this work have not yet been compared with experimental measurements.

Based on the numerical simulations performed in this work, some general trends can nevertheless be identified. In particular, nanodumbbells with relatively small aspect ratios (AR < 3) appear to be the most promising in terms of field enhancement. In this regime, the structure remains sufficiently compact to support strong localized electromagnetic fields, while still benefiting from the geometrical features introduced by the outer spheres. For larger aspect ratios, however, the overall size of the dumbbell increases significantly, leading to higher extinction cross section, as observed for the nanorods.

In summary, nanodumbbells represent a promising and experimentally accessible platform for SERS applications. However, a deeper understanding of the specific role played by the outer spheres is still required. Future work combining numerical simulations with controlled experimental studies will be essential to fully elucidate their potential and to determine the optimal design parameters.

1.6 Environment

The dielectric environment surrounding a plasmonic nanoparticle strongly influences the electromagnetic field enhancement [30]. As explained in section 1.1 the dipole induced at the center of a nanosphere is given by $p \propto \frac{\varepsilon(\lambda)-\varepsilon_m}{\varepsilon(\lambda)+2\varepsilon_m}$, where ε_m is the dielectric constant of the surrounding medium. The LSPR occurs when the induced dipole reaches its maximum amplitude, resulting in a strong enhancement of the electric field around the nanoparticle. This resonance condition is satisfied when $\varepsilon(\lambda_{LSPR}) = -2\varepsilon_m$. As already mentioned, in the case of other geometries than spheres, a geometrical factor has to be introduced [30].

An example of the influence of the surrounding environment on the electromagnetic enhancement is presented in Fig. 1.27 where the surface averaged LFIEF $\langle M \rangle$ of gold nanospheres with increasing radius is simulated at 633 nm in three different media. As shown in the figure, silica provides the highest enhancement possible because its dielectric constant is the closest to that of gold at 633 nm, for which ε_{Au}(633 nm) = -11.75 [67]. It can also be observed that the optimum nanoparticle radius increases as the dielectric constant of the surrounding medium decreases, as reported by He *et al.* [84].

1.6.1 Coating

A first approach to modifying the environment surrounding a plasmonic nanoparticle is to introduce a coating around the nanoparticle. One commonly used coating is a silica shell because of its stability, biocompatibility

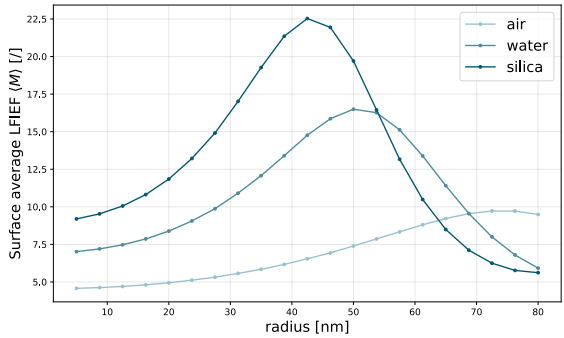


Fig. 1.27 Simulated surface averaged LFIEF $\langle M \rangle$ as a function of nanosphere radius at 633 nm for three surrounding media: air (light blue, n= 1), water (blue, n = 1.33), and silica (dark blue, n = 1.46).

and ease of functionalization [85, 86]. As discussed previously, silica is particularly well suited for excitation at 633 nm because its dielectric constant is closer to that of gold at this wavelength. An example of the implementation of a silica-coated nanoparticle in COMSOL, immersed in water, is shown in Fig. 1.28a.

The effect of the silica coating on the electromagnetic field distribution is presented in Fig. 1.28b. The electric field enhancement reaches its maximum intensity near the gold nanoparticle surface but still extends beyond the silica shell. This result demonstrates the potential of silica coatings for SERS applications, as Raman reporter molecules can be embedded between the gold core and the silica shell while remaining efficiently enhanced or nanotags and analytes located outside the silica shell may also remain detectable [87].

Introducing a coating layer around a plasmonic nanoparticle modifies its local dielectric environment. Consequently, the resonance wavelength of the coated nanoparticle depends on the thickness of the coating layer. This effect is illustrated in Fig. 1.29, where the resonance wavelength progressively shifts from the value corresponding to a nanoparticle immersed in water (blue dot at 0 nm coating thickness, corresponding to an uncoated particle) toward the value obtained for a nanoparticle fully surrounded by silica (grey dot at 40 nm coating thickness, corresponding to an effectively infinite silica layer). The same trend is observed for nanospheres of different

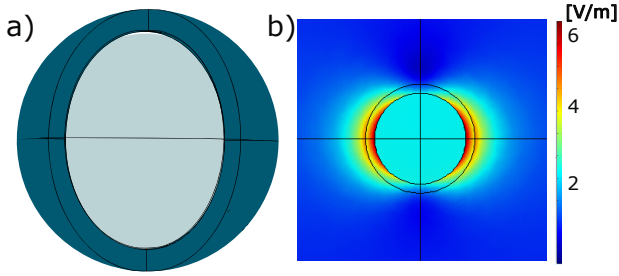


Fig. 1.28 a) Schematic representation of a gold nanosphere (light blue) with a radius of 10 nm coated with a 2 nm thick silica shell (dark blue). b) Simulated electric field intensity distribution at the resonance wavelength of the coated nanoparticle shown in panel (a)

sizes: the nanoparticle shown in the left panel (a) has a radius of 10 nm, while the nanoparticle in the right panel (b) has a radius of 20 nm.

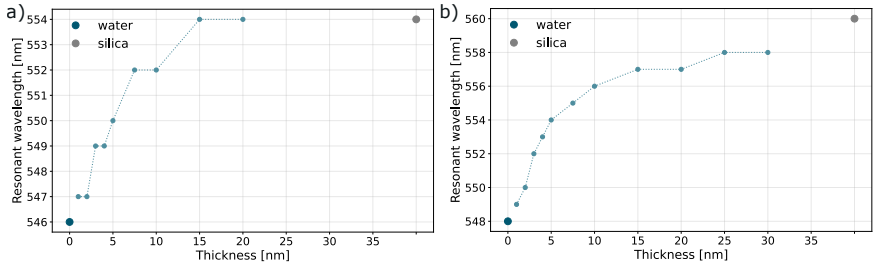


Fig. 1.29 Impact of the coating thickness on the resonance wavelength of a coated Au NP with silica. The blue circle corresponds to an uncoated nanoparticle immersed in water, while the grey circle represents an uncoated nanoparticle fully immersed in silica; a) for a gold nanosphere with a radius of 10 nm. b) for a gold nanosphere with a radius of 20 nm.

The intensity of the electric field enhancement also depends on the thickness of the coating layer. The surface-averaged LFIEF $\langle M \rangle$, is simulated both at the surface of the gold nanosphere and at the outer surface of the silica shell, as shown in Fig. 1.30. The simulations indicate that larger gold nanospheres generate stronger electric field enhancements both at the gold surface and at the outer surface of the silica shell. The influence of the silica shell thickness is more complex; the results reveal a trade-off between maximizing the electromagnetic enhancement at the gold surface, which is

favored by thicker silica coatings, and maximizing the enhancement at the outer silica interface, which is favored by thinner shells. Consequently, the optimal coating thickness depends strongly on the targeted application and on the location where the electromagnetic enhancement is required.

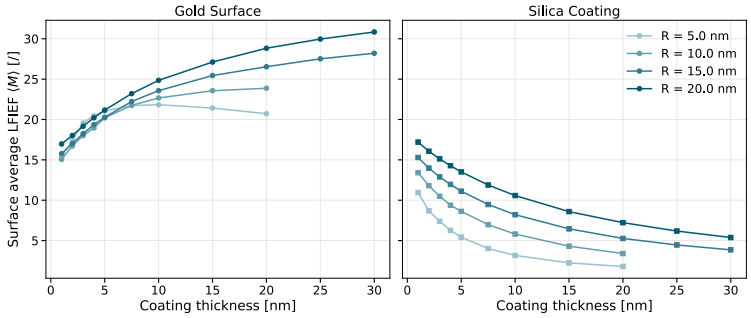


Fig. 1.30 Evolution of the Surface average LFIEF $\langle M \rangle$ as a function of the coating thickness for nanospheres with different radii. The left panel shows the LFIEF intensity calculated at the surface of the gold nanosphere, while the right panel presents the LFIEF intensity calculated at the outer surface of the silica shell.

1.6.2 Optimal effective medium

The excitation wavelength is fixed at 633 nm, corresponding to a dielectric constant for gold of ε_{Au}(633 nm) = -11.75 based on the refractive coefficients of Johnson and Christy [67]. According to the LSPR resonance condition, the optimal dielectric environment is therefore given by ε_{med}(633 nm) = 5.875. The influence of this ideal dielectric environment is illustrated in Fig. 1.31, where the same gold nanoparticle with a radius of 10 nm is simulated first in air (ε_{med} = 1) and then in a medium satisfying the LSPR resonance condition (ε_{med} = 5.87). As shown in the figure, the electric field enhancement is significantly stronger when the surrounding medium matches the resonance condition compared with the case of air. The surface averaged LFIEF $\langle M \rangle$ increases from 4.6 in air to 79.6 in the resonant medium, corresponding to an enhancement factor approximately 17 times larger. Although this example is presented for a nanosphere, the same principle applies to nanoparticles of different shapes and sizes [88].

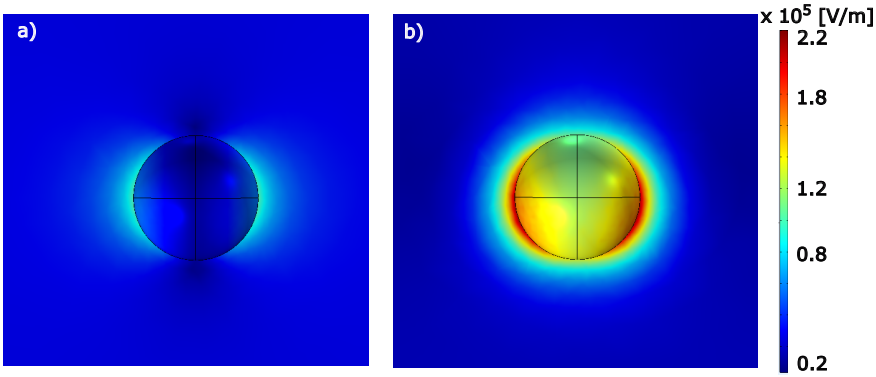


Fig. 1.31 Simulated electric field [V/m] of a Au NP with a radius of 10 nm. a) in air, with a maximum electric field intensity of 1.05×10^5 [V/m]; b) in a medium with a dielectric constant $\varepsilon_{med} = 5.87$, with a maximum electric field intensity of 2.37×10^5 [V/m]. The same color scale is used in both images.

However, this estimation should be interpreted with caution. As explained in section 1.1, SERS is inherently governed by highly localized electromagnetic effects, whereas effective medium theories rely on averaged macroscopic properties. Consequently, although this approach provides useful guidelines and supports the existence of an optimal dielectric environment, the exact morphology required to achieve this optimum must be investigated through detailed numerical simulations, as illustrated previously for the case of silica coatings as an example. Further discussion on this aspect will be provided in Chapter 3.

1.7 Key message

Several key messages can be drawn from this first chapter, which also provide perspectives for the following chapters.

First, a **numerical COMSOL model** was shown to be a powerful tool for simulating the plasmonic behavior of nanoparticles. The model makes it possible to tune the nanoparticle shape, size, and surrounding environment, and to analyze their influence on both the resonance wavelength and the

electromagnetic enhancement.

The results also demonstrated that interactions between nanoparticles can significantly modify both the electromagnetic field enhancement and the localized surface plasmon resonance. In particular, in solid-state configurations, nanoparticle coupling leads to the formation of **hotspots and induces a shift of the LSPR**. This highlights the importance of distinguishing between measurements performed in liquid suspensions and those performed after solid deposition. Although no experimental measurements of this solid-state effect were carried out in the present work, Louise Lejeune is further investigating this phenomenon.

In the case of colloidal suspensions, it was shown that evaluating the electromagnetic enhancement alone is not sufficient to predict the SERS response. The numerical model predicts the highest enhancement when λ_2 matches the excitation wavelength λ_0. However, experimental measurements revealed a different behavior, where nanorods with the smallest aspect ratios produced the strongest SERS enhancement.

To explain this discrepancy, the analytical model proposed by van Dijk *et al.* [74] was introduced, highlighting the **crucial role of the extinction cross-section in liquid suspensions**. By combining this analytical framework with numerical simulations, it became possible to extend the original model, previously limited to spheroidal nanoparticles, toward a fully numerical approach applicable to nanoparticles of arbitrary geometry. This methodology was successfully applied to nanodumbbells. Although additional experimental validation is still required, this approach already appears promising for estimating the SERS enhancement of colloidal nanoparticle suspensions.

Finally, the influence of the surrounding environment on the LFIEF was investigated numerically. For gold nanoparticles, the results suggest that working around 633 nm is particularly advantageous because gold absorption losses remain relatively low in this spectral region. In addition, the optimal dielectric constant predicted by the LSPR condition, $\varepsilon(\lambda_{\mathrm{LSPR}}) = -2\varepsilon_m$, is approximately 5.87, which lies within the dielectric constant range of porous silicon and oxidized porous silicon. This result highlights the **strong potential of porous silicon as a plasmonic environment** and motivates the investigations presented later in Chapter 3.

2

Understanding the porous silicon material

Porous silicon (PSi) has recently emerged as a promising substrate for SERS due to its intrinsically rough surface morphology and highly developed porous structure. In particular, porosity represents a critical design parameter for SERS, as it simultaneously addresses two major challenges: analyte concentration, and electromagnetic field enhancement [89]. It is therefore essential to first understand the properties of this material and subsequently develop a substrate that can be functionalized with plasmonic nanoparticles. The approach adopted in this work is based on freestanding membranes, building upon previous research conducted in this laboratory [8, 9]. This chapter investigates the following research question:

RQ2: How can a porous substrate be fabricated to enable efficient decoration with plasmonic nanoparticles?

This chapter establishes the foundation for the substrates that will later incorporate the plasmonic nanoparticles described in Chapter 1. Their integration and application will be discussed in Chapter 3.

The chapter begins with a brief introduction to porous silicon and presents the fundamental concepts required for the remainder of the chapter. The key fabrication parameters are then introduced, together with their influence on the structural and optical properties of PSi. Different porous silicon nanostructures are subsequently presented. Particular attention is given

to a challenge encountered during fabrication, namely the formation of a transitional layer that hinders the formation of uniformly wide pores. A transfer matrix model is then proposed to better understand the influence of PSi properties on its optical reflectance.
Once the material and its properties are well understood, freestanding membranes (FSMs) are introduced as a simple and versatile approach for the fabrication of porous substrates that can subsequently be decorated with plasmonic nanoparticles. A brief state of the art of FSMs is first presented, followed by the development of a reproducible fabrication protocol enabling both repeatable membrane fabrication and integration into microfluidic systems through controlled membrane release. The flow-through properties of these FSMs are then characterized. Finally, Bragg mirror FSMs are introduced to demonstrate the adaptability of the proposed fabrication strategy to more complex nanostructures. Their fabrication process and the tuning of their optical response are presented in detail. The results presented in this chapter are adapted from our journal publications [JP1, JP2].

2.1 Background of PSi

Porous silicon (PSi) is a nanostructured form of silicon obtained through electrochemical etching, offering a versatile platform for a wide range of applications. Although first discovered in the 1950s by Arthur Jr. and Ingeborg Uhlir, it only gained significant attention in the late 1980s following the observation of quantum confinement effects. This discovery revealed unique optical and electronic properties, sparking extensive research into its potential [90, 91, 92].

PSi is particularly attractive due to its tunable structural characteristics, such as porosity, pore size, and thickness, which can be precisely controlled during fabrication. These features enable the design of materials with tailored optical and transport properties. In particular, porous silicon membranes [93, 94], formed by detaching the porous layer from the bulk substrate, act as permeable structures suitable for applications in sensing, filtration, and molecular transport. The combination of compatibility with established silicon technology and low-cost fabrication makes PSi a highly promising material in both fundamental research and applied fields.

2.1.1 Fabrication

The interest in porous silicon arises from its versatile structural properties, which can be widely tuned through various fabrication conditions. In particular, parameters such as pore size, thickness and porosity can be controlled over broad ranges, enabling a large variety of applications.

Several fabrication approaches have been developed, mainly based on dry etching or electrochemical methods. Dry etching involves the use of a hard mask followed by anisotropic plasma etching to define pore structures [95]. In contrast, wet chemical approaches include electrochemical etching and stain etching. The latter is based on the spontaneous dissolution of silicon in an oxidizing HF-based solution [96] and, when combined with metal catalysts such as thin films or nanoparticles, leads to Metal-Assisted Chemical Etching (MACE). In MACE, the metal locally enhances the oxidation and dissolution of silicon, enabling the formation of highly anisotropic and well-defined porous or nanostructured features [97].

Electrochemical etching, also referred to as anodization, relies on the controlled dissolution of monocrystalline silicon under an applied current in an HF-containing electrolyte. This process can be performed using either a double-cell configuration with two platinum electrodes or a single-cell setup where at the anode the silicon wafer is oxidized and a platinum electrode serves as the cathode. The etching system is typically constructed from HF-resistant materials such as Teflon® or polyether ether ketone (PEEK) to ensure chemical stability [9]. A schematic illustration of an electrochemical single etching cell is shown in Fig. 2.1a, and the cross-section of this cell is shown in Fig. 2.1b.
Even if the electrochemical process depends on many parameters listed above, it can be stated that there are some general shared features [98]:

- Pores initially form randomly and without any specific ordering on the silicon surface, unless the wafer has been intentionally pre-patterned.
- The electric current is mainly concentrated at the bottoms of the pores.
- The pore walls become passivated, so that silicon dissolution occurs predominantly at the interface between the porous layer and the

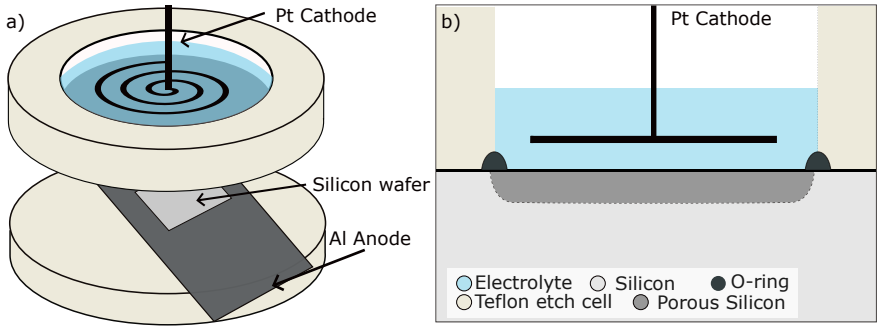


Fig. 2.1 a) Exploded view of an electrochemical etching cell, with a Teflon etch cell, an aluminum foil as anode, a silicon wafer, and a platinum spiraled wire that is the cathode; b) cross section of the etch cell after the anodization of the PSi.

underlying crystalline silicon substrate.

- After their formation, pores remain stable and do not reorganize or change structure.
- The PSi samples exhibit a range of pore sizes rather than a uniform diameter.

The electrochemical etching of silicon can be described by two main regimes: pore formation and electropolishing. The transition between these regimes depends on the substrate properties, such as doping level and crystalline orientation, and external parameters like electrolyte concentration and temperature. However, it is primarily governed by the ratio between the applied current density and the concentration of fluoride ions [9].

The most widely accepted description of PSi formation is the model proposed by Lehmann and Gösele [92]. In this framework, pore formation is driven by valence band holes acting as oxidizing agents. Under an applied electric field, these holes migrate to the silicon surface by drift and diffusion, a process enhanced at sharp pore tips where the electric field is locally intensified. When holes reach the surface, they weaken Si-H bonds, allowing fluoride ions F^- from the HF electrolyte to substitute hydrogen atoms and form highly polarized Si-F bonds. This weakens adjacent Si-Si bonds, enabling their dissolution and the removal of silicon atoms as SiF_4 [98]. This simplified mechanism is shown in Fig. 2.2.

As dissolution proceeds, pores nucleate and grow preferentially at their tips, where the current density is highest. A space-charge region forms along the pore walls, limiting lateral etching and promoting anisotropic pore propagation. However, when the current density is significantly increased or the fluorine ion concentration becomes insufficient, this space-charge region shrinks. As a result, pore walls begin to merge, marking the transition to the electropolishing regime, in which the porous structure collapses and a smooth silicon surface is formed [98].

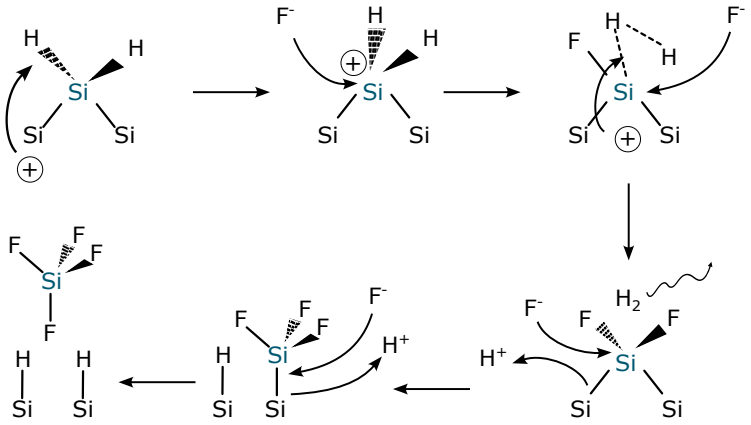


Fig. 2.2 Simplified mechanism for electrochemical etching of silicon in a fluoride-containing solution, where ⊕ are valence band holes, adapted from [98].

Freshly etched porous silicon is typically hydrogen-terminated, with reactive Si-H_x surface groups that are metastable. Exposure to air leads to gradual oxidation and incorporation of impurities such as oxygen and carbon, causing progressive surface degradation [99].

2.2 Characterization of porous silicon

Before describing the fabrication of porous membranes that will be used in Chapter 3, it is necessary to first explain the characterization methods of PSi. All the wafers used in this work have the same resistivity that has been

measured with the four-point probe method. The resistivity measurements yielded a value of 0.98± 0.02 mΩ·cm, which corresponds to the value indicated by the manufacturer (< 2 mΩ·cm). For all experiments presented in the following sections, the same parameters were used unless otherwise specified. If any parameter was modified for a particular experiment, the change will be clearly indicated in the corresponding section. All parameters are summarized in Table 2.1.

Parameter	Value
Etching solution	HF (49% aqueous):ethanol (3:1 v/v)
Removing solution	2 M KOH
Resistivity of p-doped silicon	0.98 ± 0.02 mΩ·cm
Current density	5–800 mA/cm^2
Etch area	1.2 cm^2

Table 2.1 Parameters used for the porous silicon etching process.

The link to the code used to control the Keithley source measure unit during the porosification process is provided in the appendices. The code can be adapted to define different current-density profiles and etching conditions, enabling the fabrication of porous silicon nanostructures with tailored morphologies.

2.2.1 Porosity & etch rate

Each porosification was performed by anodization in a custom-built Teflon® single bath etch cell with an etching area of 1.2 cm^2 equipped with a spiraled platinum wire cathode, an aluminum flat anode and a potentiostat/galvanostat (Keithley 2450) as current source. The etching was carried out in HF(49% aqueous):ethanol (3:1 v/v).

SEM images were performed on a Scanning Electron Microscope, Zeiss Auriga FIB-SEM at an acceleration voltage of 3 kV. The samples were prepared by sticking it onto carbon paper tape on the sample holder.

The PSi has been characterized by applying different current densities from 50 to 700 mA/cm^2 to estimate the etch rate and the porosity at each current step. In Fig. 2.3, the impact of the current density on the porosity and the etch rate is shown. The etch rate was quantified through the measured

thicknesses on the SEM images. The porosity has been measured by spectroscopic liquid infiltration method (SLIM), which is a non-destructive method for determining both porosity and layer thickness. It is based on Reflective Interferometric Fourier Transform Spectroscopy (RIFTS). These techniques rely on the optical response of the porous silicon layer in the visible range. The reflectance spectrum of the porous silicon layer is measured using a 10 mW halogen light source and a fibre-couple Ocean Optics JAZ spectrometer. This measurement is performed twice at the same location using two different media: typically, the first spectrum is acquired with the pores filled with air, and the second after infiltration with a solvent. Due to multiple reflections at the top and bottom interfaces of the porous layer, the reflectance spectra display Fabry–Pérot interference fringes, arising from constructive and destructive interferences. By applying a Fourier transform to each spectrum, a characteristic frequency peak is obtained. The position of this peak corresponds to the effective optical thickness (EOT), which is related to the physical thickness L of the layer and the average refractive index n of the filled porous medium through the relation EOT = 2nL. The EOT values obtained for the two different media are then used in effective medium models, such as the Bruggeman or Looyenga equations, to determine both the porosity and thickness of the porous silicon layer [98].

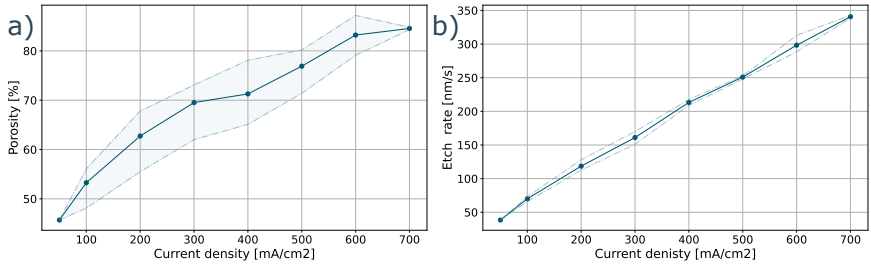


Fig. 2.3 Impact of the current density on a) the porosity and b) etch rate. Etching was performed on p-type Si with a resistivity of 1 mΩ·cm using an aqueous HF (49%):ethanol solution in a 3:1 (v/v) ratio. The blue line represents the mean value of the measures and the upper and lower lines show the maximum and minimum value of each measurement.

2.2.2 Pore size

Three pore size regimes are commonly distinguished [100]: micropores, with widths below 2 nm; mesopores, with widths ranging from 2 to 50 nm; and macropores, with widths exceeding 50 nm. The pore size is primarily governed by the doping level of the silicon substrate, as summarized in Table 2.2 [101].

Wafer type	Doping conc.	Pore size
n-doped Si	$< 10^{18}$ cm^{-3}	from nanometers to micrometers
p-doped Si	$< 10^{15}$ cm^{-3}	large pores (µm) with nanometric pores within
p+ Si	$10^{15} - 10^{18}$ cm^{-3}	1 to 10 nm
p++ & n++ Si	$> 10^{19}$ cm^{-3}	from 10 to 100 nm

Table 2.2 Effect of wafer doping concentration on the PSi pore size, adapted from [9].

Highly doped p++ silicon is particularly attractive, as it does not require external illumination during electrochemical etching. Janshoff *et al.* [102] demonstrated that, by varying the current density from 100 to 600 mA/cm^2, the pore size can be tuned over a wide range, from approximately 5 to 1200 nm.
Based on these considerations, p++ silicon wafers with a resistivity below 2 mΩ·cm were selected, since the objective is to enable the infiltration of nanoparticles or biological species within the pores, whose characteristic sizes typically range from 5 to 60 nm, as discussed in Section 1.4 and summarized in Table 1.1.
The characterization of the pore size was done on the same samples as for the porosity and etch rate, based on a custom made Matlab code. This code first converts the SEM image into a binary image, where the pores are white and the rest is black, this is based on a threshold value that is fixed at 100 for darker images and 123 for brighter images. Afterwards it extracts the pore size based on the maximum Feret diameter. This Matlab code is based on the work done by Rasson and Vercauteren [8, 9] and automates the image analysis process compared with the manual analysis performed using ImageJ. It is available in the appendices. The evolution of the pore size versus the current density is shown in Fig. 2.4 and a top view is shown in Fig. 2.5. It should be noted that this analysis is based only on the top-view morphology of the pores, which does not necessarily reflect the actual pore

size within the bulk material. A potential approach for future work would be to use the BJH method to determine the pore size distribution.

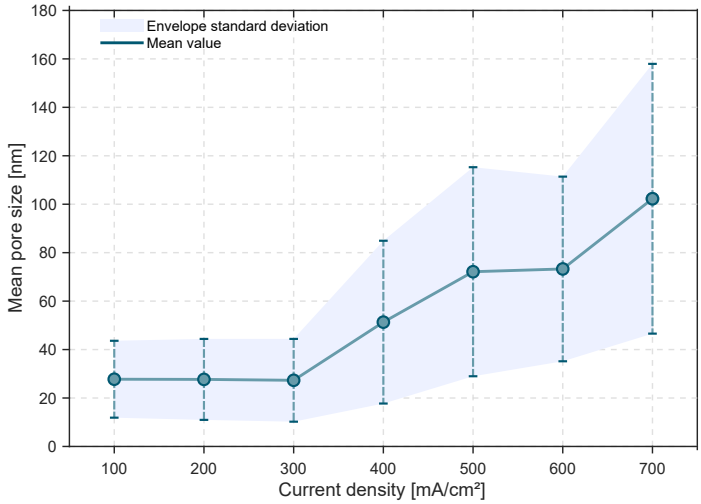


Fig. 2.4 Evolution of the pore size with the current density. The blue line shows the evolution of the mean value while the envelope shows the limits of the standard deviation.

As can be seen in Fig. 2.4, the standard deviation of the pore size increases with the current density, indicating a large pore size distribution. This had also been noted in Vercauteren [JP2]. This is not a main problem, the objective is that the mean pore size is large enough to be decorated with nanoparticles.

2.2.3 Nanostructures

By modulating the applied current density over time during a single electrochemical etching process, it is possible to fabricate porous silicon multilayers with controlled variations in pore size and porosity. This approach enables the engineering of complex structures with tailored physical and optical properties.

A common example is the formation of a double-layer structure, obtained by reducing the current density at a specific stage of the etching process. This

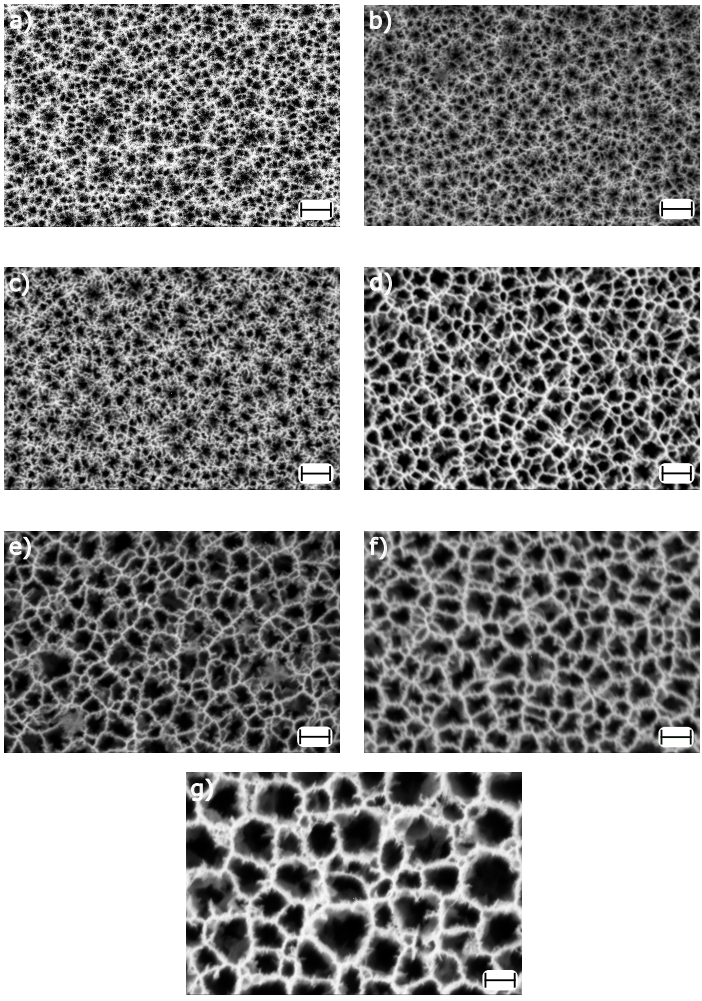


Fig. 2.5 SEM top-view images of PSi samples fabricated at increasing current densities: a) 100 mA/cm^2 b) 200 mA/cm^2, c) 300 mA/cm^2, d) 400 mA/cm^2, e) 500 mA/cm^2, ef) 600 mA/cm^2, g) 700 mA/cm^2. The scale bar is 100 nm for every image.

results in a stratified architecture composed of a top layer with larger pores and higher porosity, and a bottom layer with smaller pores and lower porosity. Such hierarchical structures are particularly well suited for selective molecular transport, as larger species may be excluded from penetrating

the lower-porosity region [103, 104]. In addition to size-selective filtration, this configuration can thus function as a sensing layer.

More sophisticated periodic structures can also be achieved, such as Bragg stacks (or Bragg mirrors), by alternating between different current densities for controlled time intervals. This produces a sequence of layers with alternating high and low porosity, each characterized by a specific refractive index n and thickness L. When designed such that the optical thickness nL of each layer corresponds to one quarter of a target wavelength, the structure exhibits a pronounced reflectance peak centered at that wavelength. This photonic behavior arises from constructive interference within the periodic stack [98]. Further details are provided in the final section of this chapter.

Beyond these configurations, a wide range of porous semiconductor architectures can be realized. For instance, porous materials can be integrated into optoelectronic devices such as vertical-cavity surface-emitting lasers (VCSELs), where porous distributed Bragg reflectors (DBRs) act as mirrors surrounding an active region [105]. This highlights the versatility of porous structures and their potential in both sensing and photonic applications.

2.2.4 Sacrificial layer

When a silicon wafer is anodized for the first time, the morphology of the pores is not uniform throughout the thickness, particularly near the surface. Watanabe *et al.* [106] were the first to report this, showing that pore sizes at the surface are significantly smaller than those deeper within the film, with diameters below 10 Å at the surface compared to a much wider range in the bulk, depending on fabrication conditions. This observation indicates that pore nucleation is not instantaneous, and that the initial stages of formation produce a distinct transitional layer, typically extending over the first few hundred nanometers [98].

Subsequent studies have shown that the properties of this transitional region depend strongly on parameters such as current density [107, 108], and models such as the wine-bottle morphology proposed by Zhang *et al.* [108] have been introduced to describe its structure. The initiation of pores is also closely linked to the presence of surface defects, such as vacancies, which

act as preferential nucleation centers [108].

From a practical standpoint, controlling or removing this non-uniform surface layer is essential. It has been demonstrated that simple electropolishing prior to porous silicon formation does not reproduce the desired pore morphology [98]. A commonly used approach consists of etching a first porous layer and subsequently removing it (e.g., using KOH) before fabricating the final layer. Alternatively, techniques such as SF_6 plasma reactive ion etching, as proposed by Rasson [8], can be used to selectively remove the transitional layer and improve the homogeneity of the porous film.

In the present work, achieving large and well-defined pores is essential, as porous silicon is intended to serve as a SERS substrate requiring efficient infiltration of plasmonic nanoparticles. This necessitates the removal of the transitional surface layer. To this end, electrochemical sacrificial etching is employed, as it offers a simple, rapid, and cost-effective approach that does not require complex instrumentation. However, it was observed that a single sacrificial etching step was not sufficient, as a transitional layer was still present on the anodized layer after the sacrificial step.

The objective is therefore to identify the key parameters governing the removal of the transitional layer and to evaluate their impact on the resulting porous structure. For this purpose, several batches of samples were fabricated, in which parameters such as etching time, current density, and the number of sacrificial etching steps were systematically varied. The resulting morphologies were characterized using top-view SEM imaging in order to determine the optimal conditions for eliminating the transitional layer while improving pore size and uniformity.

Fig. 2.6a presents a porous silicon sample etched without removal of the transitional layer, which is clearly visible at the surface. A slight scratch performed with tweezers reveals that this layer is very thin and overlies a regular porous structure underneath.

Varying the current density or the etching time alone did not lead to conclusive improvements. After removal of the sacrificial layer with KOH, the transitional layer systematically reappeared, regardless of the etching depth. In contrast, repeating the sacrificial etching step proved to be effective. It was observed that performing two consecutive sacrificial etching steps suc-

cessfully removed the transitional layer, resulting in the desired porous structure directly at the surface. Although this approach slightly increases the fabrication time (by approximately 5 minutes), it significantly improves the uniformity of the porous layer and prevents the reformation of the transitional region. This demonstrates that a purely electrochemical method can be sufficient to eliminate the transitional layer, without requiring additional techniques such as reactive ion etching.

As previously reported by Barillaro *et al.* [109], sacrificial etching also induces a pre-patterning of the silicon surface, such that the morphology of the subsequent porous layer is influenced by the initial etching conditions. As shown in Fig. 2.6b, the current density defines this pre-pattern. Performing the sacrificial etching at the same current density as the final etching step therefore promotes more uniform pore formation and can facilitate pore enlargement. The proposed approach is consistent with the method developed by Pinna *et al.*[110], where a sacrificial double layer is first formed and subsequently removed using an aqueous NaOH solution, leaving a pre-patterned surface suitable for the controlled growth of a new porous layer.

All subsequently fabricated samples underwent two identical consecutive sacrificial etching steps, and no transitional layer was observed.

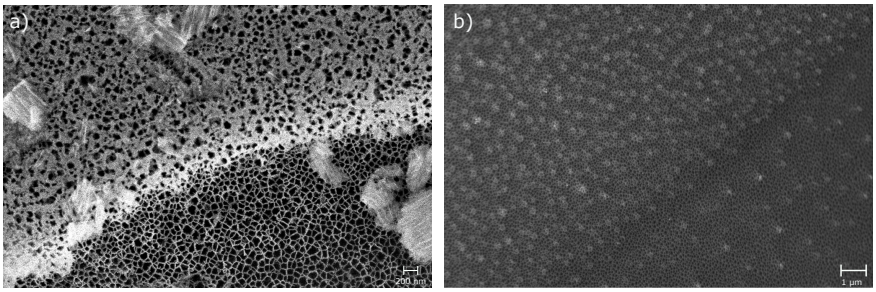


Fig. 2.6 a) SEM image of the edge of a scratched zone with tweezers, the left side shows the transitional layer and the right side shows the scratched zone with the desired PSi underneath. The etch was performed at 400 mA/cm^2 for 30 s. b) SEM image after dissolution of PSi with KOH. A pre-patterning where the future pores would probably start is shown, and is influenced by the etching current density.

2.2.5 Modeling

The optical response of the multilayer porous silicon membrane was simulated using the transfer matrix method (TMM). This approach is well suited for stratified media, as it efficiently accounts for multiple reflections and interference effects across layered structures. By representing the device as a stack of planar layers along the propagation direction, TMM provides an accurate and computationally efficient framework to model its optical behavior.

The refractive index of each layer is determined using the effective medium approximation (Looyenga [111] and Bruggeman [112] model). These effective indices are then used to evaluate the optical thickness of each layer and its contribution to the overall reflectance spectrum. When the surrounding or infiltrating medium changes, the effective refractive index of the porous layers is modified accordingly, leading to a shift in the EOT. This variation enables the calculation of relative EOT shifts based on a Fast Fourrier Transform, which serve as a key parameter to quantify the optical response of the structure to different filling media.

The model developed by Vercauteren [JP2] is shown in Fig. 2.7a. It was further optimized based on the work of Ruminski *et al.* [113] and the SCOUT software [114], which simulates various porous silicon layer configurations. The optimized transfer matrix additions:

1. The material dispersion is considered rather than assuming a fixed refractive index of 3.1.
2. The incoherent behavior of thick layers has been included.

As shown in Fig. 2.7b, the model reproduces similar interference fringes in the visible range, while deviations appear at shorter wavelengths, where the refractive index differs most significantly from the constant value of 3.1. The experimental spectrum, presented in Fig. 2.7c, is in better agreement with the updated model, confirming the importance of accurately accounting for dispersion. However, the effect of coherence cannot be clearly resolved under the present experimental conditions. For comparison between the two models, the EOT of the porous layer has been computed and is 4513 nm for the initial model, 6134 nm for the updated model, and 6165 nm for the experimental measurement, showing the improvement of the second model.

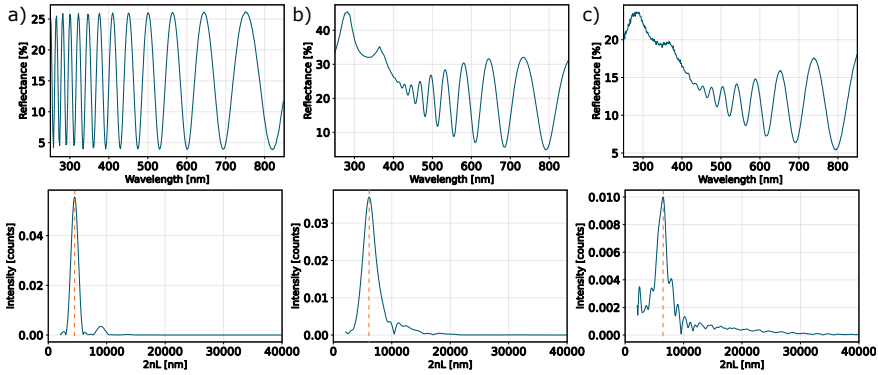


Fig. 2.7 Reflectance spectra and corresponding Fourier transforms of a porous silicon sample with a porosity of 41% and a thickness of 1050 nm, supported by a 350 µm thick silicon substrate, measured in air at an incidence angle of 50°. The Fourier transform is calculated over the spectral range from 425 to 850 nm, the orange dashed line indicates the EOT. a) Reflectance calculated using the basic TMM model; b) reflectance calculated using the improved model; c) experimental reflectance spectrum

First parameter analysis: Oxidation

A first required parameter to bring the optical model closer to experimental reality is the oxidation of PSi. Oxidation is commonly used to stabilize the optical properties of PSi; however, it also significantly alters its refractive index. Moreover, partial oxidation can already occur during anodic etching or shortly after fabrication due to exposure to ambient air, making its consideration essential in accurate optical modeling [115].

The refractive index and porosity of porous layers can thus be evaluated as a function of the oxidation degree of the silicon skeleton using the Bruggeman effective medium approximation [112]. Oxidized PSi is treated as a three-component system composed of silicon, silicon dioxide, and voids, expressed in eq. 2.1 [115].

$$(1-p-ox)\frac{\varepsilon_{Si}-\varepsilon_{eff}}{\varepsilon_{Si}+2\varepsilon_{eff}}+2.27ox\frac{\varepsilon_{SiO_2}-\varepsilon_{eff}}{\varepsilon_{SiO_2}+2\varepsilon_{eff}}+(p-1.27ox)\frac{\varepsilon_{fill}-\varepsilon_{eff}}{\varepsilon_{fill}+2\varepsilon_{eff}}=0 \tag{2.1}$$

where p is the initial porosity, ox is the fraction of the silicon carcass that has been oxidized and transformed into SiO_2, ε_{eff} is the dielectric constant of the effective porous silicon and ε_{fill} is the dielectric constant of the sur-

roundings that fills the pores, usually air or a liquid.
The oxidation process induces a volumetric expansion of the solid matrix, as the formation of SiO_2 increases the volume of the silicon carcass by a factor of 2.27 [113]. The oxidation degree is quantified by the fraction of silicon converted into oxide relative to its initial content; $s = \frac{ox}{1-p} * 100\%$.

From an optical perspective, oxidation systematically reduces the effective refractive index of PSi. Although the pores become partially filled with SiO_2, which has a higher refractive index than air, this effect is outweighed by the consumption of silicon, whose refractive index is significantly larger. The magnitude of this change depends on the initial porosity: low-porosity layers exhibit a stronger decrease in refractive index upon oxidation, while highly porous layers are less sensitive. This is shown in Fig. 2.8a at a wavelength of 633 nm.

Additionally, the evolution of porosity during oxidation depends strongly on its initial value, as shown in Fig. 2.8b. Highly porous layers can retain their pore structure even after complete oxidation, whereas layers with lower initial porosity may experience pore closure before full oxidation is reached, leading to a transition toward a dense Si-SiO_2 composite. The full mathematical explanation is described in [115].

Second parameter analysis: Rugosity

A second parameter that must be considered to improve the realism of the optical model is the interface roughness, which affects the reflected intensity through increased light scattering. Two types of interface fluctuations have been identified by Lerondel *et al.* [116, 117]: long-range waviness at the millimeter scale and short-range roughness at the micrometer scale. The former has been attributed to resistivity oscillations in the silicon substrate, which induce periodic variations in layer thickness during the etching process [116]. While the roughness is inherently present but depends on the etching time and current density [117].

The interface roughness is incorporated in the transfer matrix method through a modification of the Fresnel coefficients, typically by introducing a mean roughness height that attenuates coherent reflection [118, 119]. The presence of such roughness is particularly evident at the air/PSi and PSi/Si interfaces, visible in Fig. 2.9.

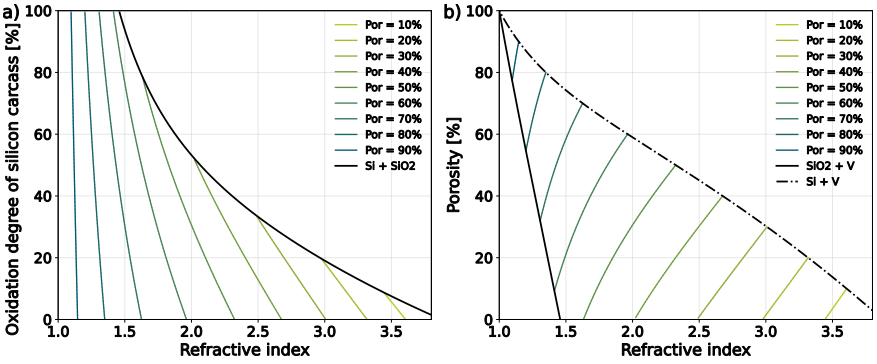


Fig. 2.8 a) Calculated dependence of PSi oxidation degree on its effective refractive index for different initial porosities, the black curve corresponds to the films without pores that have been closed because of the oxidation. b) Relationship between the refractive index and porosity of oxidized PSi films, the black curve corresponds to porous silica while the dashed black curve to the two-component system without oxide. Adapted from [115].

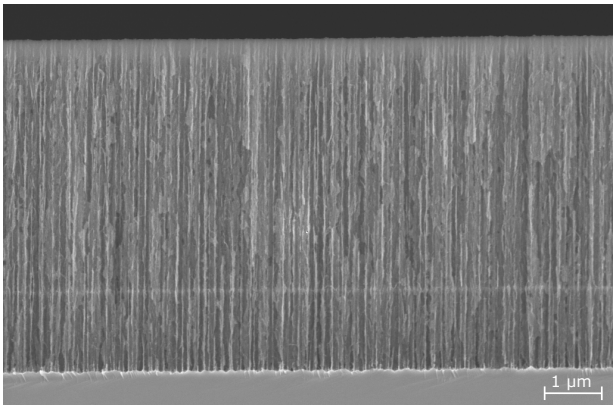


Fig. 2.9 SEM image of a cross-section of a 600 mA/cm^2 etch for 20 s.

Discussion on the final improved model

The model parameters, namely porosity, layer thickness, interface roughness, and oxidation degree, were optimized by minimizing the mean square error between the simulated and measured reflectance spectra. The resulting best-fit values were then compared with experimental measurements obtained by SEM for the thickness and SLIM for the porosity, yielding values of 1050 nm and 41%, respectively.

The simulated reflectance curve that best matches the experimental data (Fig. 2.10) corresponds to a porosity of 41% and a thickness of 910 nm. In addition, mean roughness values of 10 nm and 15 nm were obtained for the air/PSi and PSi/Si interfaces, respectively, while the oxidation degree was estimated to be approximately 4%, consistent with the presence of a native oxide layer.

Despite this apparent agreement, several limitations must be acknowledged. In practice, it is not possible to independently and accurately determine all model parameters, particularly interface roughness and oxidation degree, which are difficult to validate experimentally. Moreover, for the purposes of this work, the most relevant parameters are the pore size and layer thickness, both of which can be directly measured using SEM. While the proposed modeling approach provides a more comprehensive description of the system, it also introduces additional complexity without necessarily improving the reliability of the key parameters of interest.

Consequently, the main advantage of this model lies in its ability to qualitatively assess the influence of parameters on the reflectance response, as previously demonstrated by Vercauteren [JP2]. However, within the scope of the present study, the inclusion of interface roughness and oxidation is not considered essential.

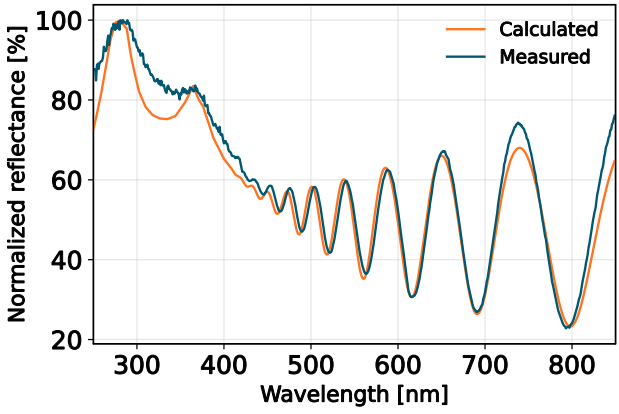


Fig. 2.10 Comparison between calculated and measured normalized reflectance of a PSi sample of 1050 nm and a porosity of 41%.

2.3 Freestanding membranes

A nanostructure that is of great interest as reviewed by Vercauteren *et al.* [120] are the self-supported PSi membranes. They have five main application areas: electronics, energy conversion, medical applications, sensing, and microfluidics. They usually rely on several anodization and microfabrication processes to reach successful integration within applicable devices [120]. However, this requires compliance to typical silicon-based electronics cleanroom processes, that are costly, intensive in resource and time-consuming. The release of the membrane is the most critical step, including combinations of wet, dry and electrochemical etching. The full fabrication process can take up to a week of labor intensive work, and generates waste as effluent [9].

This is where the interest for a quick and simple fabrication method for flow-through PSi membranes is raised. Freestanding membranes are a solution and have a straightforward process which is used in many application fields, going from the integration of radio-frequency micro-inductors in microelectronic devices [121, 122] to the porous silicon transfer process for thin-film silicon solar cells for photovoltaics [123]. It is also used in the medical domain as either drug delivery method [98] or biosensor [124].
Having fully characterized the porous silicon, the next step is to develop a freestanding membrane intended for subsequent decoration with plasmonic nanoparticles (cf. Chapter 3). To this end, the following section focuses on the key fabrication steps required to produce porous silicon FSMs with large pores, with particular emphasis on ensuring reproducibility and compatibility with microfluidic integration.

2.3.1 Related work

FSM prepared by electrochemical etching involve a two-step process. First, a layer with the desired porosity for the final membrane is created. Then, a high porosity layer is produced, which is brittle and coalesces into a cavity under the first layer to facilitate the membrane's mechanical detachment in a step named lift-off. This is represented in Fig. 2.11 and it locates the cavity. After this phase, the freestanding layer can be transferred onto another

substrate, such as tape or polymer slab, for implementation in different applications. The remaining bulk silicon substrate can be reused afterwards [121], a sacrificial etching step is suggested to restore a flat starting substrate for subsequent processing.

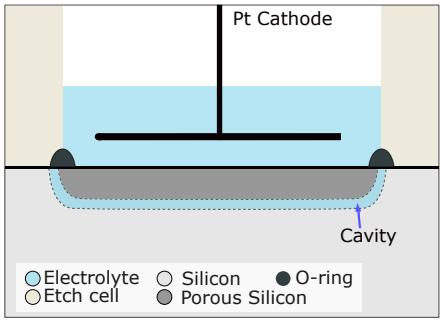


Fig. 2.11 Cross section of the etch cell after the formation of the cavity.

Since the early 2000s, multiple methods to fabricate FSM by electrochemical etching have been explored. The electrochemical etch involves wet etching of monocrystalline silicon by applying an electric current at the electrodes in the presence of a HF-containing electrolyte [98]. Solanki *et al.* [125] proposed a two-step procedure, where the current applied is increased after the first anisotropic layer is etched. This allows to rapidly increase the pore size and thus generates the cavity, causing lift off [126], as this isotropic etch interconnects the pores that finally merge into a single void [125]. These pores will eventually overlap together and fracture from the bulk [127, 128].

The key of the lift-off is to apply a sufficiently high current such that the mass transfer rate of fluoride ion is lower than the delivery rate of valence band holes at the Si/PSi interface. The shortage of fluoride ions leads to the formation of SiO_2 instead of the soluble SiF_4 and the reaction stoichiometry transitions from 2 electrons in eq. 2.2 to 4 electrons in eq. 2.3 [98]:

$$Si + 6HF + 2h^+ \longrightarrow SiF_6^{2-} + 4H^+ + H_2 \tag{2.2}$$

$$Si + 6HF + 4h^+ \longrightarrow SiF_6^{2-} + 6H^+ \tag{2.3}$$

This oxide layer grows further at the interface and blocks the electrochemical current, this results in the thinning of the pore walls. Eventually the

oxide layer is dissolved by HF, leading to the detachment of the porous layer [98]. This mechanism is called electropolishing.

In the case of incomplete lift-off, the membrane can still be detached subsequently mechanically either on a tape, as reported by Bardet *et al.* [121], or on polydimethylsiloxane (PDMS) [129, 130, 131, 132, 133, 134]. Some mechanical force can also be applied, such as water jet, ultrasonic vibration or mechanical tensile force [125]. Another way to induce the detachment is to score and release the edges of the patterned film before the second anodization using a stainless-steel syringe [124, 129, 134].

The main disadvantage of PSi FSM is the low repeatability of the procedure and the fragility of the resulting membrane that limits the integration in a microfluidic set-up as mentioned by Zhao *et al.* [135]. The control of large pore size is another challenge [98], notably with p-type Si substrates, that are preferred for their compatibility with electronics applications. To the best of our knowledge, FSMs have reached average pore sizes of 50 nm at the maximum, as shown in Table 2.3. This table compares the mean pore size of FSM in the literature, but not the thickness as it is a less critical parameter because it mainly depends on the etch time. This limitation in pore size hinders the flow of liquids or NPs suspensions through the membrane. A final problem of current PSi FSM fabrication methods is related to near-edge porosity that poses specific problems as it varies due to restricted electrolyte diffusion and nonuniform current density under the O-ring seal during the electrochemical etch [136]. This leads to difficulty in reproducing the shape of the FSM and problems of integration in a microfluidic set-up [135].

2.3.2 Fabrication

A p-type Si substrate of 1 mΩ·cm is etched with an electrolyte solution used for each etching step being a solution of HF (49% aqueous): ethanol (3:1 v/v) in a custom-built Teflon® single bath etch cell with an etching area of 1.2 cm^2 equipped with a spiraled platinum wire cathode, an aluminum flat anode (shown in Fig. 2.1a) and a potentiostat/galvanostat (Keithley 2450) as current source. The sacrificial step consists in etching twice a sacrificial porous layer at 300 mA/cm^2 for 60 s and removing it with a 2M solution of KOH for 5 minutes. Since porous silicon dissolves in strongly basic

Mean pore size (top)	Electropolishing current	Etch time	Ref.
3–8 nm	13–27 mA/cm^2	1.5 s	[126]
10 nm			[137]
10 nm	250 mA/cm^2		[125]
6–17 nm	220 mA/cm^2		[138]
20 nm	50 mA/cm^2	30 s	[139]
20 nm	4 mA/cm^2	95 s	[131, 132]
20–30 nm	600 mA	few seconds	[140]
2–30 nm	450 mA	60 s	[141]
30 nm	45 mA/cm^2	15 s	[133]
35 nm	800 mA/cm^2	0.1 s	[124]
30–40 nm	22 mA/cm^2	180 s	[142]
20–60 nm	76 mA/cm^2	6 s	[143]
40 nm	200 mA/cm^2	pulse	[144]
40–80 nm	high	pulse	[145]
52 nm	170 mA/cm^2	60 s	[146]
67 nm	**800 mA/cm^2**	**3 s**	**this work**
0.5–2 μm	2–15 mA/cm^2	10 min/step	[128]

Table 2.3 Comparison of FSM from the literature based on pore size.

media, this step provides a rapid and effective cleaning of the surface. By eliminating the initial irregularities, the subsequent porosification proceeds more uniformly, leading to improved reproducibility and a narrower pore size distribution [98].
Then, for a single layer FSM, an etching step is carried out at a constant current density of 300 mA/cm^2 for 360 s. After an etch stop of 3 seconds, a current density of 800 mA/cm^2 is applied for 3 seconds. The FSM is then rinsed three times with isopropanol before being glided onto a Kapton® holder. This entire process is completed under 25 minutes and gives a porosity of around 70% and an estimated membrane thickness of 57 µm. The membrane is then oxidized at 200°C for 1 hour under ambient atmosphere to stabilize the oxidation of the FSM.

Double layer FSM structures are fabricated following the same protocol as the single layer samples, with the exception of the anodization sequence following the sacrificial etch step: a current density of 300 mA/cm^2 is applied for 19 seconds, followed by an etch stop of 3 seconds. A second anodization is then performed at 100 mA/cm^2 for 783 seconds. Upon release, the result-

ing FSM comprises a first porous layer with approximately 70% porosity and a thickness of 3 µm, followed by a second layer with 55% porosity and a thickness of 54 µm. 50 single layers FSMs and 25 double-layers FSMs were prepared which demonstrates the repeatability of the process.

After characterizing the substrate at different current densities and by measuring the porosity and pore size, it was found that at a current density of 300 mA/cm^2, the pores have a mean size of 67 ± 38 nm, as shown in Fig 2.12a. This average size of 67 nm is large for FSMs compared to the state of the art, as shown in Table 2.3. This is an improvement compared to previous work [JP2] where the maximum pore size that could be achieved without compromising the mechanical integrity of the membrane was found to be 55 ± 25 nm.

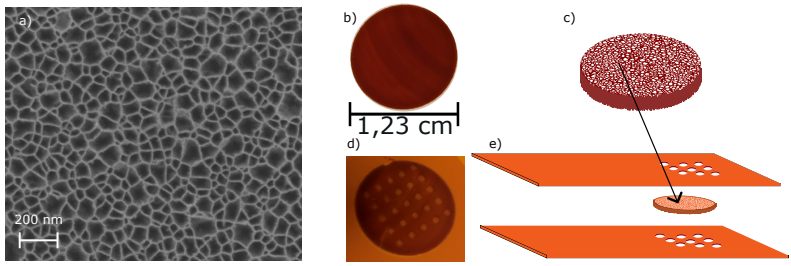


Fig. 2.12 a) SEM image of the top of the FSM prepared at a current density of 300 mA/cm^2, with a magnification of 37.23 kX, the pores have an average size of 67 nm ; b) top-view photography of the top of an FSM of 1.2 cm^2; c) schematic image of an FSM extruded from Fig.a; d) FSM sandwiched inside the Kapton holder; and e) exploded schematic view of the FSM in the Kapton holder.

The FSM was subsequently integrated into a home-made Kapton® holder (DuPont de Nemours inc.) that was perforated by CNC cutting. Kapton® is a polyimide sheet with heat resistance up to 400 °C, making it a suited material for the thermal processes involved during the whole fabrication. This holder eases the manipulation of the FSM. It also increases the process compatibility, the flexibility and the mechanical strength of FSM. The integration of the FSM within the holder is shown in Fig 2.12 c–e.

The Kapton® was processed into a membrane holder, as shown in Fig 2.12,

by Computer Numerical Control (CNC) cutting three distinct layers with a Cricut Explore AirTM 2 machine. Two identical outer layers, each measuring 2 x 4 cm^2, are perforated by the CNC cutter with uniformly distributed 1 mm diameter holes in the region intended to contact PSi. The Kapton® film was then cleaned with acetone and ultrasound bath before exposing all layers to a 24 s 200 W oxygen Plasma. The Kapton® can be cleaned after the incorporation of the FSM and reused afterwards.

2.3.3 Controlled release of the FSM

To increase the reproducibility of the FSM preparation, it is needed to better understand and improve the release process from the substrate. To do so, a FEM on COMSOL Multiphysics® software is used to analyze the electropolishing step after the anisotropic etch.

The COMSOL model is based on the work of Ivanov [147] , where the time-dependent finite-element simulations of the anodization process have been performed in COMSOL Multiphysics®(COMSOL Inc.) version 6.1 in the electrodeposition physics. Fig. 2.13a shows the 2D geometry that was used. The stoichiometry of the equation was set to 4 and a high current density of 800 mA/cm^2 was applied to simulate the electropolishing step. In order to find a solution, a time step of 10 µs was applied.

To ensure reproducibility and robustness, the following settings were used. The silicon substrate and electrolyte were discretized with triangular elements, with mesh refinement applied at the silicon/electrolyte interface to capture the current crowding effect. A convergence test following the procedure of Ivanov *et al.* [147] was performed, showing that the results obtained with a finer mesh were consistent with those from the coarser mesh described here, with deviations below 5%. Boundary conditions were set to ground at the cathode and to a fixed applied current at the anode, consistent with the experimental anodization configuration. The moving boundary was tracked using the deforming mesh option with automatic remeshing. The nonlinear solver was run with Newton iterations and Jacobian updates at each time step. These settings provided stable and reproducible simulations, consistent with the results reported in Ivanov [147].

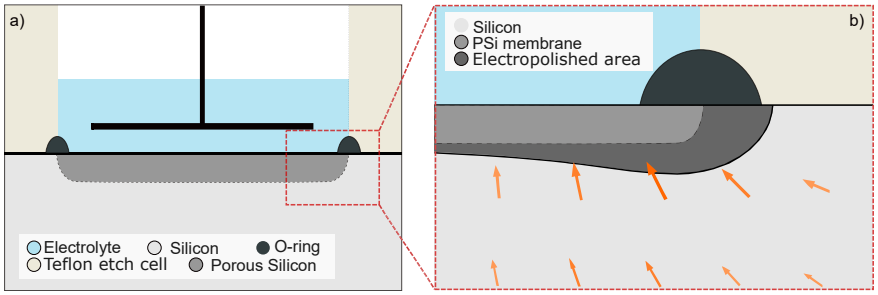


Fig. 2.13 Cross-section views of a simulated electrochemical etch: a) after the first anodization step; b) zoom of the simulated etch front of the electropolished underetch below the O-ring during the second anodization step. Orange arrows represent the electrode current density from the aluminum electrode, and the gradient of the arrows shows the intensity of the current density.

This simulation analyses the behavior beneath the O-ring, as the porosity varies at the edges. Fig. 2.13a illustrates the porosification after the initial step, while Fig. 2.13b depicts the electropolished region beneath the O-ring after 3 seconds of etching. The convex shape that is obtained can be explained by two complementary mechanisms: the electrical mechanism and the diffusion mechanism [148]. The electrical mechanism refers to the distribution of current during the etching process. At the beginning of etching, the electric current is not uniformly distributed across the silicon surface. Due to the geometry of the mask, higher current densities occur near the edges of the openings, leading to faster etching at these regions and resulting in a convex profile. In parallel, the shape evolution is also influenced by the diffusion mechanism, which is governed by the transport of ions in the electrolyte. As the process continues, ion transport becomes increasingly restricted by the geometry (e.g., mask thickness and opening size), which gradually alters the etching profile [148].

The arrows in Fig. 2.13b indicate the direction of the electrode current density and the gradient represents its intensity, demonstrating that the area beneath the O-ring is etched more rapidly than the surrounding regions, due to current crowding. This observation aligns well with experimental results. By varying the electropolishing duration, we noted that insufficient electropolishing time prevents membrane detachment, whereas excessive electropolishing induces membrane breakage at the border near the O-ring.

Therefore, an optimal electropolishing time must be determined to ensure a complete lift-off of the membrane without compromising its structural integrity at the edges. If the electropolishing step is too short (t < 2 s), the porous layer is still attached to the substrate, while if the electropolishing time is too long (t > 5 s), the border of the FSM is weakened and breaks off as shown in Fig. 2.14.



Fig. 2.14 Broken FSM after an electropolishing step of 5 seconds.

Fig. 2.15 shows the temporal profile of the imposed current (orange) and a typical measured voltage profile (blue) during the phase of electropolishing for the release of the membrane. As can be seen, there is a clear drop of the voltage at 365 seconds, this means that the lift-off just took place [127], immediately after, the voltage rises again, indicating the formation of a new PSi layer on the substrate. Similar observations have also been reported in the literature [126, 149]. The moment of release can vary a bit from device to device, this is why a minimum of 3 seconds and a maximum of 5 seconds is recommended.

Knowing the importance of the electropolishing step, our PSi FSM fabrication process follows the simple approach outlined in Corsi's work [124], except omitting the mechanical step of scratching the edge of the FSM to separate it from bulk silicon. We use a controlled electropolishing time of 3 seconds instead, ensuring a clear and reproducible release of the FSM at the surface of the electrolyte solution. A top view of the so-obtained FSM is shown in Fig 2.12b, showing a disk of 6.2 mm of diameter.

Table 2.3 summarizes various p-type FSMs classified according to their pore size, which spans from a few nanometers to several micrometers. Using the methodology developed in this work, the mean pore size of 67 nm falls within the upper end of this range. As highlighted by the variation

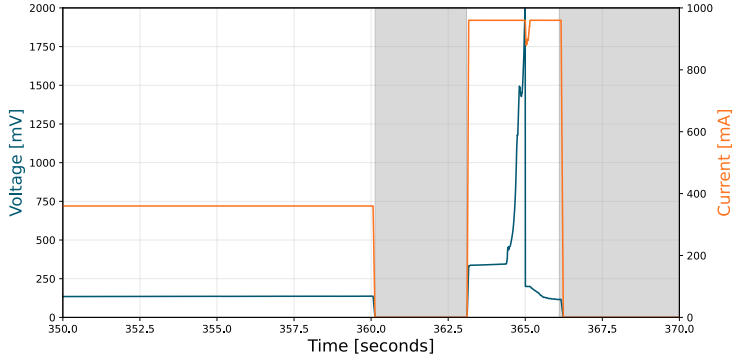


Fig. 2.15 Temporal profile of the current (orange) and voltage (blue) applied at the release, where no current is applied in the grey area (etch stop). The tension drop appears a bit after 2 seconds of high current applied, this means that the membrane is in this case released after 2 s.

in electropolishing currents and etching times, the release process of FSMs is highly dependent on the specific fabrication approach adopted in each study.

2.3.4 Microfluidic integration

The microfluidic set-up wherein the Kapton® holder can be placed, is shown in Fig 2.16a-c. The Kapton® holder shape helps to limit the stress that is applied onto the FSM when fastening the screws of the microfluidic cell.

The flow rate of DI water in the empty Kapton® holder and for the Kapton® holder with the single layer FSM have been measured at different pressure values with a Fluigent LINEUP fluidic setup (see Fig 2.16a). The linear relation of 6.9 µL/min/mbar and 4.1 µL/min/mbar was obtained for the empty holder and with the single-layer FSM, respectively, as shown in Fig 2.17, where the same relation can be seen at the increase and decrease of the pressure. This is in accordance with the Darcy law that states that the flow is proportional to the applied pressure [150].

To reach a flow of 20 µL/min, a pressure of 40 mbar is needed, as shown in Fig. 2.18a. This is a lower pressure than typical pressure applied on PSi

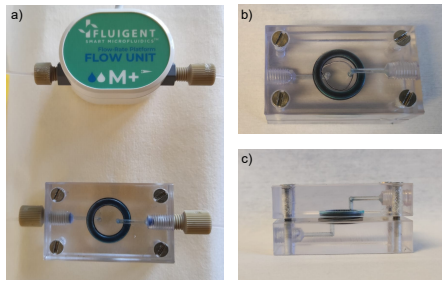


Fig. 2.16 a) Picture of the microfluidic setup, showing the Fluigent flow unit that measures the flow rate upstream of the cell; Microfluidic cell: b) top view, c) side view.

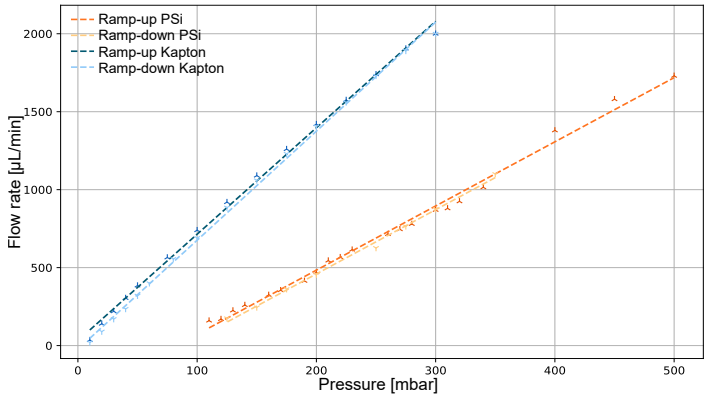


Fig. 2.17 Pressure versus the flow rate for the rise (dark markers) and drop (light markers) of the pressure with their respective linear regression (dashed curves), for the Kapton holder alone (blue) and single-layer FSM (red), with a respective slope of 6.9 µL/min/mbar and 4.1 µL/min/mbar.

membranes so far; for instance, for a flow of 15-20 µL/min Vercauteren [9] reported that a pressure of 2 bar needs to be applied due to the smaller PSi pore size of 12-20 nm. To compare the impact of the pore size, the flow through the double layer has been also measured. The linear relation is then 0.01 µL/min/mbar for the double layer, shown in Fig. 2.18b. The observed flow through the membranes with 20 nm pores is approximately 400 times lower than that of the membrane with 67 nm pores. This strong dependence is well described by the Hagen-Poisseuille equation, which predicts that the volumetric flow rate Q through a cylindrical pores scales as

$Q \propto 1/r^4$, where r is the pore radius. Given this fourth-power relationship, even modest increases in pore size lead to substantial increases in flow. The ratio of 67 nm over 20 nm to the fourth power corresponds to 126, which is of the same order of magnitude as the measured slope ratio between the two. Consequently, working with larger pores is advantageous, as a lower pressure is required to achieve a given flow rate.

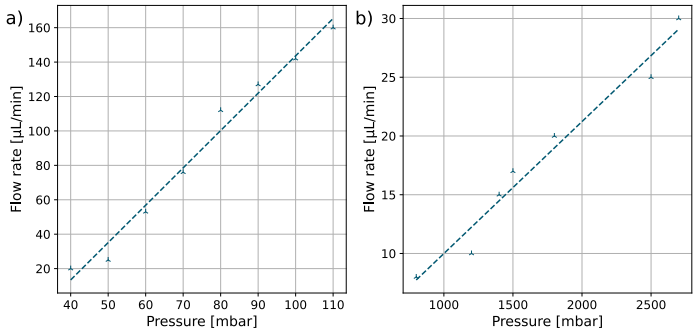


Fig. 2.18 Pressure versus flow rate during the pressure rise, the dashed lines represent linear regression fits; a) Single-layer FSM, exhibiting a slope of 2.17 µL/min/mbar; b) Double-layer FSM, with a slope of 0.011 µL/min/mbar.

2.4 Bragg mirror FSM

A more complex nanostructure of interest for the applications discussed in Chapter 3 is the Bragg mirror. This section describes the fabrication of the Bragg stack as a freestanding membrane (FSM).

A Bragg stack consists of a periodic arrangement of two alternating porous silicon layers with high and low porosity. This structure enhances reflectivity within a defined stopband centered at a target wavelength λ_s. The thickness L of each layer is controlled by the etching time, while the current density determines the porosity and thus the refractive index. The stopband position is therefore set by these parameters according to the following relation:

$$\frac{\lambda_s}{4} = n_h L_h = n_l L_l, \tag{2.4}$$

with n_h and n_l the refractive index of the high and low layer respectively and L_h and L_l the thickness of the high and low layer. An example of these alternating layers is shown in Fig. 2.19.

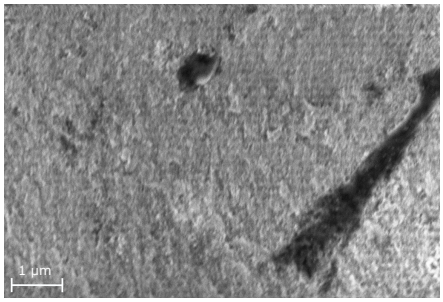


Fig. 2.19 SEM cross section of a Bragg mirror composed of alternating layers fabricated at 5 mA/cm^2 for 8.31 s (low porosity layer) and 45 mA/cm^2 for 4.41 s (high-porosity layer).

Freestanding multilayer photonic structures have attracted increasing interest for sensing and optoelectronic applications. For example, Liu *et al.* fabricated freestanding GaN-based distributed Bragg reflector (DBR) membranes for flexible optoelectronic devices [151]. In porous silicon, several types of freestanding photonic structures have been reported, including rugate filters [145], multilayer FSMs for naked-eye monitoring of drug delivery [152], and structures incorporating multiple optical cavities[153]. Freestanding porous silicon nanostructures have also been investigated for flow-through sensing applications and compared with conventional flow-over architectures [133, 154]. In addition, fully oxidized porous silica-based Bragg mirror FSMs have been demonstrated[155].

Despite these developments, relatively limited research has focused on the fabrication of reproducible porous silicon Bragg mirror FSMs. Furthermore, to the best of our knowledge, the integration of plasmonic nanoparticles with such freestanding Bragg mirror structures has not yet been reported. This aspect will be investigated in Chapter 3.

2.4.1 Tuning of the stopband

The precise tuning of the photonic bandgap remains a critical challenge in the design of Bragg mirror structures [156, 157]. Conventional approaches typically rely on semi-empirical and iterative optimization procedures to achieve a target optical response [98]. In this work, a different and more controlled strategy is adopted.

Because the flow rate strongly depends on the pore size as shown in Fig. 2.17, and the mirrors are intended to be functionalized with a colloidal suspension, the applied current density during electrochemical etching is deliberately kept constant. This ensures a uniform pore morphology and comparable fluid transport properties across all samples. Consequently, the refractive index of the layers remains effectively unchanged.

Under these conditions, the only available parameter to tune the photonic bandgap is the etching time, which directly determines the thickness of each layer. The key idea of this approach is to scale the etching time by a multiplicative factor relative to a reference structure. By doing so, the entire Bragg stack is proportionally stretched or compressed while preserving identical fabrication conditions, since the stopband and scaling factor are linearly proportional following eq. 2.4.

The evolution of the measured stopband center wavelength as a function of the etching time scaling factor is shown in Fig. 2.20a, together with top-view images of the fabricated Bragg mirrors taken with a simple camera, whose color varies with λ_s in Fig. 2.20b. The reference Bragg structure, designed for a stopband centered around 580 nm, was fabricated using 40 pairs of a low current density of 5 mA/cm^2 applied for 8.31 s and a high current density of 45 mA/cm^2 applied for 4.41 s. All other structures were then obtained by multiplying these two etching times by a common scaling factor, while keeping the current densities unchanged.

A clear linear dependence of λ_s on this scaling factor is observed. This demonstrates that uniformly scaling the etching time results in a proportional shift of the stopband position. Therefore, the photonic bandgap can be predictably and reproducibly tuned through a single parameter, without altering pore size or other structural properties.

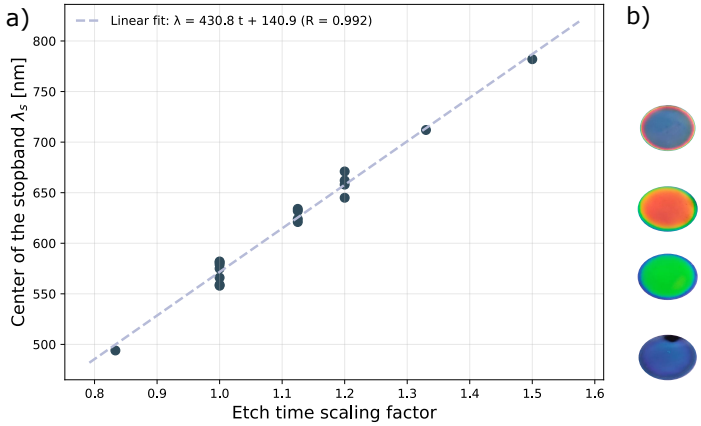


Fig. 2.20 a) Evolution of the measured mean value of λ_s as a function of the etch time scaling factor relative to the reference Bragg structure; the dashed grey line represents the linear relation. b) Image of the top view of fabricated Bragg mirrors at 500, 580, 623 and 712 nm.

For each fabricated Bragg sample, multiple reflectance spectra were acquired due to surface inhomogeneity. The averaged reflectance spectra for different scaling factors (1, 1.125, 1.2, and 1.33) are shown in Fig. 2.21. A clear redshift of the stopband wavelength, λ_s, is observed with increasing scaling factor. Additionally, samples 3 and 4, which were fabricated using identical process parameters, exhibit the same λ_s position and reflectance intensity, demonstrating good reproducibility of the fabrication process.

2.4.2 Fabrication of Bragg FSM

A sensing layer is added above the Bragg stack since the objective will be to accumulate the nanopartciles inside the porous layers and it had been showed by Vercauteren [9] that this sensing layer was important for the capture of the analyte. The whole stack consists thus different porous layers, starting with a sensing layer above a Bragg mirror that lays on a support layer. This is shown in Fig. 2.22.

A p-type Si substrate of 1 mΩ·cm is etched with an electrolyte solution used for each etching step being a solution of HF (49% aqueous): ethanol (3:1 v/v). The first step consists in etching twice a sacrificial layer at 500

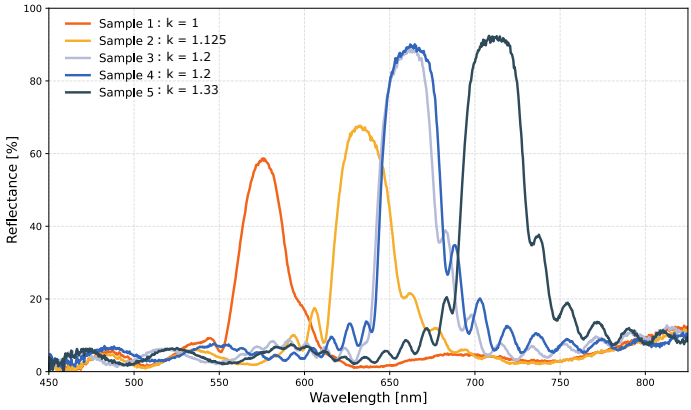


Fig. 2.21 Averaged reflectance spectra measured at normal incidence of 5 samples with scaling factor: 1 (orange), 1.125 (yellow), 1.2 (light blue and blue) and 1.33 (dark blue).

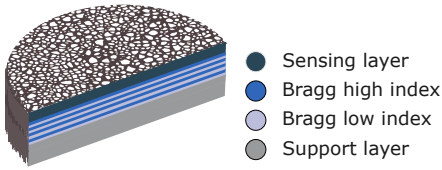


Fig. 2.22 Schematic cross section of the structure of the Bragg FSM.

mA/cm^2 for 60 s and removing it with a 2M solution of KOH by dissolving it for 5 minutes, (cf. subsection 2.2.4). Next, the sensing layer is etched with a current density of 500 mA/cm^2 for 7 seconds, this gives a thickness of 1.8 µm and a porosity of 79%. Then 40 pairs of alternating high and low current are applied with a current density of 5 mA/cm^2 and 45 mA/cm^2 for 8.31 s and 4.41 s respectively. Afterwards the support layer is anodized with a current density of 120 mA/cm^2 for 783 seconds, creating a layer of 54 µm that brings support to the whole structure since it has relative small porosity and is around 50 μm thick. Between each layer, an etch stop of 2 seconds is applied to be sure that HF has the time to diffuse. All the methodology is summed up in Table 2.4. To detach the FSM from the silicon wafer, the same lift-off current as in previous section has been applied, showing that this lift-off methodology can be adapted to all different substrates. The

membrane is then oxidized at 200 °C for 1 hour under ambient atmosphere to stabilize the oxidation.

Layer	Current density [mA/cm^2]	Time [s]	Porosity	Thickness
Sensing	500	7	79%	1.8 μm
Bragg high index	5	8.31	23%	200 nm
Bragg low index	45	4.41	40%	141 nm
Support	120	783	55%	54 μm
Lift-off	800	3	/	/

Table 2.4 Fabrication parameters of the reference Bragg FSM centered at 580 nm.

The SEM cross-section of the reference structure is shown in Fig. 2.23. The sensing layer can be observed at the top of the structure, characterized by straight vertical pores. Below this layer, the Bragg stack is identified by the alternating porous layers. The straight pores are not clearly visible within the Bragg stack because the individual layers are only 200 nm thick, which limits their resolution at this magnification. Finally, the upper part of the support layer can be observed beneath the Bragg stack, exhibiting vertical pores. The same color code used in Fig. 2.22 is reproduced next to the SEM image to identify the different layers.

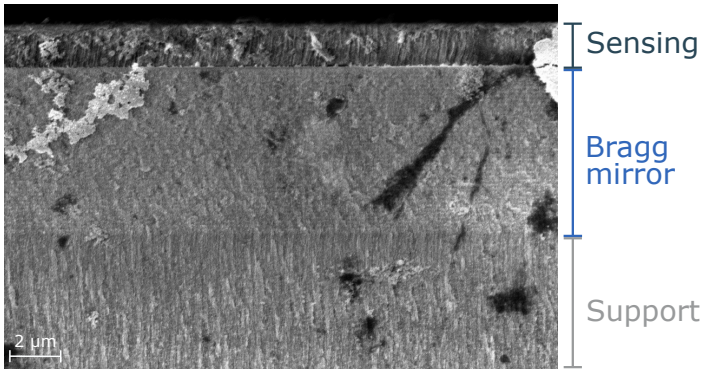


Fig. 2.23 SEM cross section of the reference Bragg structure. The different layers indicated on the right using the same color code as in Fig. 2.22: the sensing layer is shown in dark blue, the Bragg stack in blue, and the support layer in grey.

2.5 Key message

In this chapter, the porosity, etching rate, and pore size of the porous silicon substrates were systematically characterized. This understanding enabled the precise tuning of the different fabrication protocols in order to obtain the desired structural and optical properties.

During the development of the sacrificial layer process, it was observed that a single sacrificial etching step did not lead to satisfactory pore size, whereas the use of **two consecutive sacrificial etching steps** resulted in reproducible and reliable structures. Although the exact mechanism behind this improvement remains unclear, this approach is consistent with the method proposed by Pinna *et al.* [110], where a sacrificial double layer is formed and subsequently removed. While their exact procedure could also be investigated in future work, the present approach was retained because of its simplicity, reliability, and the minimal additional fabrication time required for each membrane. Another solution could be to increase the etching time to 120 seconds, which could be investigated in future work.

A transfer matrix model was also introduced to simulate the optical response of porous silicon structures. Although a more advanced model could improve the interpretation of reflectance measurements, this was not the primary objective of the present work, which mainly focuses on SERS applications. Nevertheless, the model provides a solid foundation for future studies involving the optical properties of porous silicon structures.

FSMs were then introduced as a versatile platform due to their **straightforward and reproducible lift-off**, which requires minimal fabrication steps. These membranes can be fabricated rapidly and adapted to a wide variety of porous silicon nanostructures. Different fabrication strategies were explored, and it was found that maintaining the lift-off current for 3 s enabled clean and reproducible membrane release, independently of the membrane structure. This behavior was further supported by numerical simulations.

The integration of these membranes into a microfluidic setup was also demonstrated, enabling flow-through operation. The required **pressure was shown to strongly depend on the pore size**, highlighting the impor-

tance of designing membranes with sufficiently large pores to avoid the need for excessive pressure during operation.

Finally, the fabrication strategy was successfully extended to porous silicon Bragg mirror membranes, which are of particular interest for the applications discussed in the next chapter. A simple and tunable methodology for the fabrication of porous silicon Bragg mirror membranes was demonstrated, and a linear relationship between the etching time and the stopband center wavelength, λ_s, enabled precise control of the photonic bandgap. These results illustrate the **versatility of porous silicon** and demonstrate that a wide range of **nanostructures can readily be transformed into free-standing membranes**. The research question addressed in this chapter is therefore successfully answered, as the fabricated membranes possess pores larger than the plasmonic nanoparticles while maintaining sufficient mechanical stability, making them suitable for subsequent nanoparticle decoration in Chapter 3.

3

Decoration of PSi with Au Nanoparticles for SERS application

SERS relies on the presence of plasmonic nanoparticles, whose properties strongly enhance the resulting signal. As discussed in Chapter 1, the size and shape of these nanoparticles play a crucial role in tuning their plasmonic resonance and, consequently, in optimizing the Raman enhancement. In addition to their intrinsic properties, the local environment surrounding the nanoparticles can further influence their optical response and enhance the SERS signal.
In this context, integrating metallic nanoparticles into porous silicon appears particularly promising. As presented in Chapter 2, porous silicon is a highly versatile material whose structural parameters such as pore size, thickness, and structure, can be precisely controlled. Combining these two aspects naturally raises a key question:

RQ3: How can porous silicon be decorated to enable the integration of various types of nanoparticles, and how are these nanoparticles distributed within the porous structure?

Beyond nanoparticles incorporation, it is essential to understand the role of the substrate itself. The porous matrix may contribute to signal enhancement through several mechanisms, including pore geometry, surface

roughness, and light–matter interactions. Moreover, introducing more complex optical architectures, such as photonic structures, could further amplify the Raman signal. This leads to another question:

RQ4: What is the effect of the decorated porous substrate on the SERS signal?

To address these two questions, this chapter is organized as follows. First, a brief review of the state of the art is presented, with the aim of comparing existing nanoparticles deposition techniques and highlighting their respective advantages and limitations. Next, we discuss why porous silicon can be considered an effective SERS substrate, supported by numerical simulations that illustrate the influence of pore geometry on electromagnetic field enhancement.
The experimental section then follows, where the porous silicon substrates fabricated in Chapter 2 are used. A novel decoration method is introduced and described in detail. Its effectiveness is evaluated through quantitative analysis of nanoparticles incorporation, followed by reflectance measurements to calibrate the process.
Finally, SERS measurements are performed on the decorated substrates to investigate the influence of the porous matrix. The study begins with simple structures to establish a baseline SERS response, and subsequently explores the enhancement achieved by incorporating Bragg mirror structures, in order to further amplify the signal.

All measurements in this chapter have been performed using the FSMs introduced in Chapter 2. Results are adapted from our journal paper [JP1] regarding the first research question, and from our latest experiments for the second question.

3.1 Related work

Since the late 1980's, PSi interested the scientific community for its many optical properties [120]. But it has been given additional attention lately since its hybridization by integration with plasmonic NPs that increase its optical, physical, and chemical properties and open the door to many applications. Indeed, the chemical and physical properties [158] of NPs are controlled by their sizes and shape, but are also dependent on their surrounding environment that dictates their plasmonic behavior. They can

improve the physical properties of semiconductors, and more specifically PSi [159]. The optical response of PSi can be tuned by NPs thanks to the strong localized electromagnetic fields near the surface of plasmonic NPs [159]. This behavior arises from the collective excitation of the electrons in the metal, responsible for the formation of the surface plasmons. Therefore, the local resonance occurs at the interface between PSi and NPs and enhances the coupling efficiency of light because of enhanced optical scattering [160].

This filling of PSi with plasmonic NPs is thus a hot topic and has been used recently in many promising application fields including enhanced photovoltaics [161], catalytic activity [158, 162, 163] , anti-reflective coatings [160], enhanced light emission in optoelectronic devices [164, 165, 166, 167, 168], antibacterial activity [142], computerized tomography imaging [169], surface-enhanced Raman [170, 171, 172] or infrared absorption spectroscopy [143, 173, 174, 146, 175, 176, 177, 178], as well as enhanced interferometric performance in (bio)sensing applications [179].

The decoration of the silicon pores by NPs has been demonstrated through several ways as reviewed by Khinevich *et al.* [27]. It is possible to synthesize the NPs in situ through the immersion deposition [163, 167, 168, 143, 173, 146, 178, 180], where the weak Si-H bonds are used to reduce impregnated metallic ions into metal NPs. This galvanic immersion plating method is usually chosen because of its simplicity but NPs typically form clusters on the surface [167] with poor control over their shape and size. In addition, there is only minor penetration of the deposited NPs into the thickness of the pores system [173]. Some authors proposed to oxidize the PSi to enhance its hydrophilicity and thus increase the amount of NPs synthesized inside the pores [168, 169].
By opposition, the pores can be decorated by depositing metallic NPs from their colloidal suspensions [27]. The main advantage of this method compared to all other in situ techniques is that the size and shape of the NPs can be well controlled by prior wet-synthesis targeted for the desired applications. Non-covalent chemistry can be used to reach electrostatic interactions, as for example the layer-by-layer technique proposed by Mariani *et al.* [179] for the nanoassembling of AuNPs onto silicon dioxide. Another method is the silanization [170] of the PSi with aminopropyltriethoxysilane as a linker for Au NPs. However, most of the decorated PSi substrates are prepared via drop-casting [159, 161, 165, 181] of the nanoparticles suspension, which

typically results in the formation of a metallic crust on the surface. This crust can result in clogging of the pores rather than filling them, because of the hydrophobic character of PSi [159]. The deposition is typically inhomogeneous and exhibits a coffee-ring pattern, which is influenced by the porosity and oxidation state of the PSi [159].

The common problem with most of these methods is that the NPs are mainly on top of the PSi and not trapped inside the pores, while a higher plasmon effect has been shown when Au NPs are uniformly distributed in the pores [168, 170]. The mobility being higher outside the pores, NPs deposited on the outer surface also tend to form clusters which cannot be controlled. This is why we propose here an innovative solution by enabling the flow of Au NPs through PSi membranes to decorate the totality of the thickness of the PSi layers.

3.2 Porous silicon as SERS substrate

Numerous strategies have been developed to fabricate efficient SERS-active substrates, including colloidal nanoparticles [182, 183], lithographically patterned surfaces [184, 185], and metal-coated nanostructures [186, 187]. In most cases, the dominant contribution to Raman enhancement arises from the electromagnetic mechanism, which relies on the strong amplification of the local electromagnetic field near plasmonic nanostructures. This enhancement is particularly intense in highly confined regions, commonly referred to as "hotspots", typically located at nanogaps or sharp features between adjacent metallic nanoparticles [188].

In this context, PSi has recently emerged as a promising SERS substrate due to intrinsically rough and highly developed surface morphology [176]. Compared with flat substrates, porous silicon offers a very high specific surface area, enabling efficient loading of both plasmonic nanoparticles and target analytes [189]. In addition, its pore size and porosity can be finely tuned through electrochemical etching, allowing control over nanoparticles packing, spatial distribution, and analyte confinement within the structure. PSi is also compatible with large-scale and cost-effective fabrication processes, while exhibiting advantageous properties such as biocompatibility [176, 190], making it particularly attractive for sensing and biomedical appli-

cations. The integration of PSi with plasmonic materials therefore represents a powerful approach for the development of reliable, cost-effective, and ultrasensitive solid SERS substrates [27, 191].

From a structural perspective, the intrinsic nanoscale roughness and highly developed pore network of PSi promote the formation of a large density of electromagnetic hotspots when decorated with metallic NPs [89]. The curvature and irregularity of the pore walls favor strong local field confinement [89], while this rough surface not only enhances light scattering efficiency but also facilitates local electromagnetic field confinement [192]. Furthermore, PSi can be engineered into photonic structures, such as Bragg mirrors, enabling additional field enhancement through constructive interference and resonant light confinement.

Beyond these geometrical and optical considerations, the dielectric environment provided by PSi is particularly relevant for plasmonic enhancement. As discussed in previous section 1.6, the optimal surrounding dielectric for maximizing the electromagnetic response of gold nanoparticles is around 5.8, which lies within the typical range of the effective dielectric constant of porous silicon in the visible spectrum. This suggests that PSi provides a favorable optical environment for plasmon resonance tuning and field enhancement. Consequently, analyzing the electromagnetic field distribution within a pore becomes especially relevant, as it allows one to assess both the effect of multiple scattering induced by the porous structure and the influence of the surrounding medium on the plasmonic response.

Importantly, PSi does not merely act as a passive support for plasmonic nanoparticles. Its porous framework serves as a three-dimensional template that enables controlled organization and distribution of metallic nanostructures. By tailoring both the structural parameters of PSi and the characteristics of the nanoparticles (size, shape, composition, and spatial arrangement), the plasmonic response can be finely tuned to maximize the SERS enhancement factor and lower the detection limit.

Altogether, these features make PSi a highly promising host material for the design of advanced SERS substrates, combining structural versatility, optical tunability, and compatibility with scalable fabrication processes.

3.2.1 Simulation of the pore effect

To the best of our knowledge, only a limited number of studies have explicitly addressed the role of the PSi matrix in the electromagnetic response of plasmonic nanoparticles through numerical simulations. In most reported works, the substrate is either approximated as flat or treated as a simplified effective medium, without fully accounting for the complex morphology of the porous network [193, 194]. Among the few studies that attempt to model this interaction more realistically, the work of Lu *et al.* [195] provides valuable insights into the influence of silicon morphology on the local electromagnetic field distribution.

In their study, FDTD simulations were performed to compare the electromagnetic response of silver NPs deposited on flat silicon and on nanoporous silicon surfaces. A key observation is that, in the case of nanoporous silicon, a significant fraction of the nanoparticles is located at the edges of the pores. These geometrical features induce stronger field confinement, leading to a pronounced localization of the electromagnetic field around the nanoparticles. The simulations reveal that the local field intensity can be enhanced by approximately a factor of five on nanoporous silicon compared to a flat substrate. In principle, this corresponds to an increase of up to 25 times in the Raman enhancement, given the quadratic dependence of SERS on the electric field intensity. However, the authors also point out that, in experimental conditions, this enhancement is reduced due to the variability in nanoparticles size, shape, and spatial distribution, as well as the fact that not all nanoparticles are ideally positioned at pore edges [195]. However, the exact physical mechanisms underlying this improvement remain only partially understood. It is suggested that the increased porosity enhances metal infiltration, leading to a higher density of nanoparticles located at favorable positions such as pore edges, where hotspots are more likely to form [195]. Additionally, the large specific surface area of PSi increases the number of analyte molecules within the excitation volume, further contributing to the observed signal enhancement [172].
The pore depth appears to have a more complex effect: while shallow pores can support efficient enhancement, deeper pores may lead to trapping of Raman-scattered photons, ultimately reducing the detected signal [195].

Overall, these studies underline the critical role of the porous morphology in governing the plasmonic response of nanoparticle-decorated PSi

substrates. At the same time, they reveal that the interplay between pore geometry, nanoparticles distribution, and electromagnetic field localization is not yet fully understood, thereby motivating further investigation of the field distribution within realistic porous architectures.

COMSOL simulation

Building on these observations, a more detailed analysis of the electromagnetic response within realistic porous environments is required. Numerical simulations are therefore performed to explicitly analyze the influence of both the pore structure and the dielectric environment on the electromagnetic field enhancement around plasmonic nanoparticles.
As discussed in section 1.6, the optimal dielectric environment for maximizing the electromagnetic response of a gold nanoparticles corresponds to a permittivity of approximately $\varepsilon_{\text{med}}(633\text{nm}) = 5.8$. However, this estimation should be interpreted with caution. SERS is inherently governed by highly localized electromagnetic effects, whereas effective medium theories rely on averaged macroscopic properties. Therefore, while this approach provides useful guidelines and supports the idea that porous silicon enhances the local refractive index surrounding gold nanoparticles, it remains an approximation. A more accurate description requires detailed numerical simulations that explicitly account for nanoparticles placement within pores, as well as light scattering and hotspot formation effects.

To address this, electromagnetic simulations were carried out using the Electromagnetic Waves, Frequency Domain (emw) module of COMSOL Multiphysics 6.2 to model the electromagnetic response of plasmonic nanoparticles on a silicon substrate. The model is based on the application library example "Scatterer on Substrate" (Application ID 14699) [196]. The advantage of this model is that the background field incorporates the reflection and refraction at the interface.
The original COMSOL example was modified to match the system investigated in this work. The dielectric substrate used in the reference model was replaced with the wavelength-dependent complex refractive index of silicon [197]. Additionally, the geometry of the scattering particle was modified. Instead of the particle geometry used in the original example, the scatterer was modeled as a gold nanosphere of 10 nm radius, placed on the substrate surface. To investigate field confinement within nanostructures, a cylindrical pore with a diameter of 25 nm was introduced into the substrate.

A plane electromagnetic wave was used as the excitation source, incident on the substrate surface. The intensity of the electric field is determined by the input port power that is fixed at 1 MW/m^2 times the area of the port. Perfectly matched layers (PMLs) were applied at the outer boundaries of the simulation domain to absorb outgoing scattered fields and prevent artificial reflections. Periodic Floquet boundary conditions were applied along the lateral boundaries of the computational domain to emulate an infinitely extended structure in the lateral directions.

The simulation results provide direct insight into the role of both the substrate and the pore geometry. In the planar configuration (Fig. 3.1a), a strong electric field enhancement is observed at the interface between the gold nanoparticles and the silicon surface. However, this enhancement remains highly localized, with the resulting hotspot confined to a very limited spatial region. When the nanoparticles is positioned within a pore (Fig. 3.1b), two key effects emerge. First, the local field intensity is further increased compared to the planar case, due to the combined influence of geometric confinement and the higher refractive index environment since the resonance frequency is shifted. Second, and more importantly, the spatial extent of the enhanced field is significantly broadened within the pore volume.

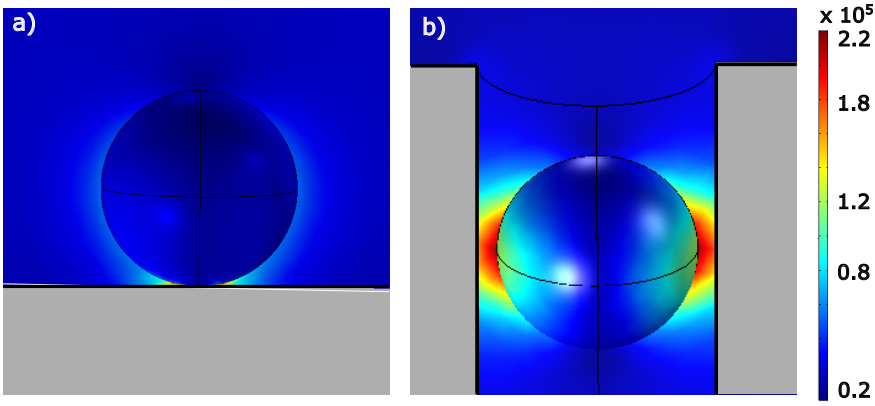


Fig. 3.1 COMSOL simulations of the electric field norm [V/m] at 633 nm of a AuNP withe a radius of 10 nm; a) on a silicon substrate where the maximum electric field value is 1.88×10^5 [V/m]; b) in a pore of silicon, where the maximum electric field value is 2.21×10^5 [V/m]. The same color scale is used in both images.

This behavior is reflected quantitatively by the average surface enhancement factor $\langle M \rangle$, which increases from 1.77 for a planar silicon interface to 13.2 in the presence of a pore, showing an increase of 7.45 between the two scenarios. Although this value remains below the theoretical maximum predicted for an ideal homogeneous medium predicted in section 1.6, it highlights the critical role of realistic porous geometries in enhancing both the intensity and spatial distribution of electromagnetic hotspots.

Overall, these results demonstrate that porous silicon provides a dual advantage for SERS applications: it offers a favorable dielectric environment for plasmonic resonance while simultaneously introducing geometrical confinement that enhances and spatially extends the electromagnetic field. This combined effect, which is not captured by simplified models, underscores the importance of explicitly considering both pore morphology and matrix properties in the design of optimized SERS substrates. Although the present study focuses on a spherical gold nanoparticle, the underlying physical mechanism, namely the interplay between dielectric environment and geometrical confinement, are not specific to this particular geometry. Similar enhancement trends are therefore expected for nanoparticles of different shapes, as the formation of localized surface plasmons and associated hotspots remains governed by the same fundamental principles.

3.3 Decoration of the FSM

3.3.1 NPs synthesis protocol and characterization

The synthesis and characterization of the nanoparticles has been done by Louise Lejeune. It is described here and it can be noted that the LSPR band of the NRs has been tuned to be close to the excitation wavelength at 633 nm.

Gold nanorods suspension used in the microfluidic experiments were prepared by a seed-mediated protocol developed by Vingderman and Zubarev [198]. The seeds were prepared in a glass vial of 10 mL placed in an oil bath thermostatically controlled at 25 °C, 2.5 mL of aqueous solution of CTAB (0.15 mol/L) (previously dissolved at 30 °C) was mixed with 120 µL of $HAuCl_4$ (0.0145 mol/L). Next, 600 µL of 0.01 mol/L $NaBH_4$ was added

to the solution while stirring. The solution turned brown. The solution was aged for 40 minutes at 25 °C without stirring, prior to use. In a 50 mL Erlenmeyer flask, stirred at 30 °C in a thermostatically controlled oil bath, 5.7 mL of MilliQ water was added. Then, 3.333 mL of CTAB (0.15 mol/L) and 500 µL of $HAuCl_4$ (0.0145 mol/L) were mixed together. The solution was orange. 50 µL of $AgNO_3$ (0.01 mol/L) and then 500 µL of HQ (0.1 mol/L) were added under stirring for an anisotropic growth. The solution became uncoloured immediately after the addition of HQ. Finally, the as-prepared seeds were added and the suspension was left for aging in the oil bath at 30 °C without stirring for 24 hours. To stop the reaction, the suspensions were centrifuged at 9690 RCF for 40 minutes (Biofuge Stratos®, Heraeus instruments, Corning® 50 mL centrifuge tubes, Centristar cap™). The supernatant was carefully discarded and the nanoparticles were resuspended with MilliQ water (final volume of 25 mL). Before the microfluidic integration, NRs were concentrated four times by centrifugation (21802 RCF, 10 minutes), discarding the supernatant and then resuspended in a final volume 4 times smaller. NRs were then labelled with malachite green isothiocyanate (MGITC, Invitrogen™, ThermoFischer Scientific) (5×10^{-5} mol/L), by adding 50 µL of MGITC (10^{-3} mol/L) in a final total volume of 1 mL.

To characterize the nanorods suspension UV-vis spectroscopy was performed. Ultraviolet–visible–near-infrared (UV–Vis–NIR) extinction spectra were acquired in the 400–1100 nm range using a Varian Cary 60 spectrophotometer Agilent®. Samples were analyzed in 1 cm path length quartz cuvettes (3 mL volume, BRAND UV cuvettes). Prior to the measurement, a baseline correction was performed using MilliQ water.
The UV-vis-NIR extinction spectrum is shown in Fig. 3.2. Two LSPR bands are observable due to the two axes of symmetry of nanorods (transverse and longitudinal), proving that the correct morphology is obtained [199]. The longitudinal LSPR band is located at 663 nm.

3.3.2 Methodology

Thanks to our designed Kapton® holder (see Fig. 2.12), PSi FSM are easily inserted into the microfluidic cell, as shown in Fig. 2.16, allowing a controlled flow of pre-synthetized Au nanorods suspension through the pores,

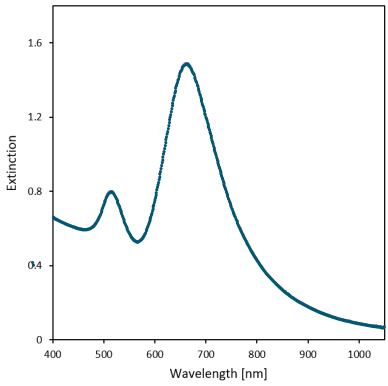


Fig. 3.2 UV-vis-NIR extinction spectrum of the NRs suspension.

leading to their deposition within the whole porosity.

To the best of our knowledge, no porosified Si membrane has previously been decorated in this way with pre-synthesized Au NPs inside the pores, even spherical ones. These Au NPs were injected at a pressure of 40 mbar. Fig. 3.3a shows the top view of the decorated membrane and Fig. 3.3b demonstrates that the flow of Au NPs went through the membrane, as we imaged a cross-section of the decorated FSM where nanorods are visible all along the thickness of the membrane with a homogeneous distribution. The bright white spots observed in Fig. 3.3 correspond to Au nanoparticles and not residuals, as confirmed by X-ray Photoelectron Spectroscopy (XPS) performed by Lauraleen Barremaecker, shown in Fig. 3.4, in agreement with other reports [189, 157, 200].

The XPS analyses were performed using a Genesis photoelectron spectrometer (Physical Electronics, USA) equipped with a monochromatized micro-focused Al Kα X-ray source, operated at 50 W. Membranes samples were mounted on the XPS sample holder using molybdenum mask. The pressure in the analysis chamber was around 10^{-6} Pa. The angle between the surface normal and the axis of the analyser lens was 0°. High-resolution scans of the C 1s, O 1s, N 1s, F 1s, Si 2p and Au 4f photoelectron peaks were recorded using a spot diameter of 100 µm, a pass energy of 55 eV, and an energy step size of 0.5 eV. Charge stabilization was achieved through the combined use of argon and electron guns. The C-(C,H) component of the

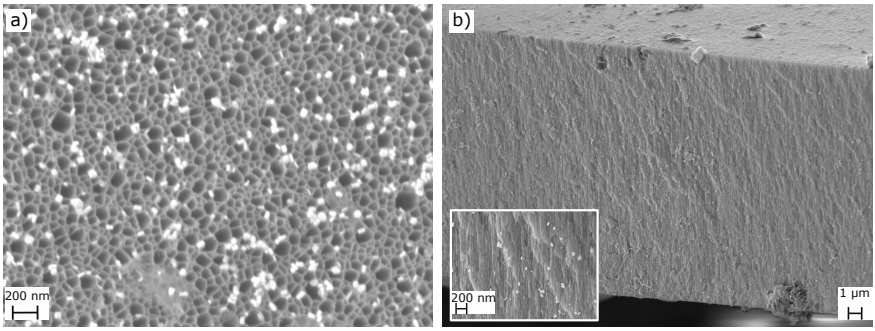


Fig. 3.3 SEM images of decorated FSM with Au NPs; a) top view of the FSM with a magnification of 26.33 kX; b) cross-section view of the whole thickness of the FSM with a magnification of 3.27 kX; the inset is a zoom of the center of it with a magnification of 41.27 kX. The Au NPs are clearly observable in white.

C 1s peak was calibrated to 284.8 eV to establish the binding energy scale. Data processing was carried out using the CasaXPS software (Casa Software Ltd., UK). Some spectra were decomposed using the least-squares fitting routine integrated into the software, employing a Gaussian/Lorentzian (70/30) product function after subtraction of a non-linear background. Molar fractions were calculated from the peak areas normalized with respect to acquisition parameters and sensitivity factors provided by the instrument's manufacturer.

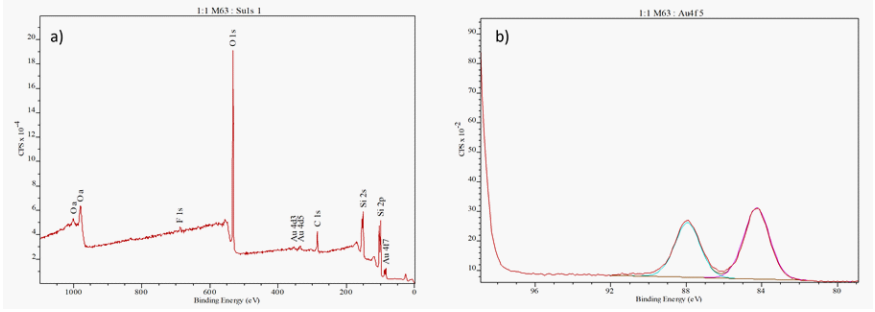


Fig. 3.4 XPS spectra of a) one FSM decorated by flow-through of gold NPs, b) narrow scan of Au 4f region.

Most of the FSM decoration in the literature is done through the immersion

plating method [143, 146, 131, 132]. In contrast, Jin *et al.* [142] achieve pore infiltration using a colloidal suspension. In their approach, the FSM is fragmented into flakes via ultrasonication before being mixed with the NPs suspension, effectively enabling full penetration. The method presented in this work offers a novel alternative, enabling the integration of pre-synthesized colloidal nanoparticles with controlled size and shape directly into intact freestanding membranes. This opens the door to applications where the FSM needs to be integrated in a flow-through system too.

3.3.3 Quantification of the decoration

When looking at the back of the FSM, shown in Fig. 3.5a, we can also see NPs, showing that the NPs fully decorate the totality of the membrane. To validate this, the amount of NPs in the FSM has been counted with a homemade Python code that uses adaptive thresholding to detect the white NPs based on contour detection. An example is shown in Fig. 3.5b. The whole thickness is shown in Fig. 3.6 where the top-left image is the top of the membrane and the bottom-right image is the bottom of the membrane; the images are ordered from left to right.

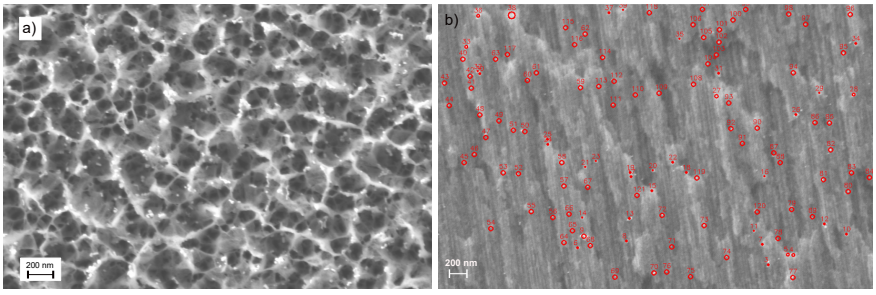


Fig. 3.5 SEM images of decorated FSM with Au NPs; a) back view of the FSM with a magnification of 31.95 kX; b) cross-section view of the FSM with a magnification of 22.67 kX, where the red dots show the automatic detection by the Python code and count the amount of detected Au NPs.

The evolution of the density of particles through the whole FSM based on Fig. 3.6 is shown in Fig. 3.7, which allows us to calculate a mean density of 8.47 # NP/μm^2.

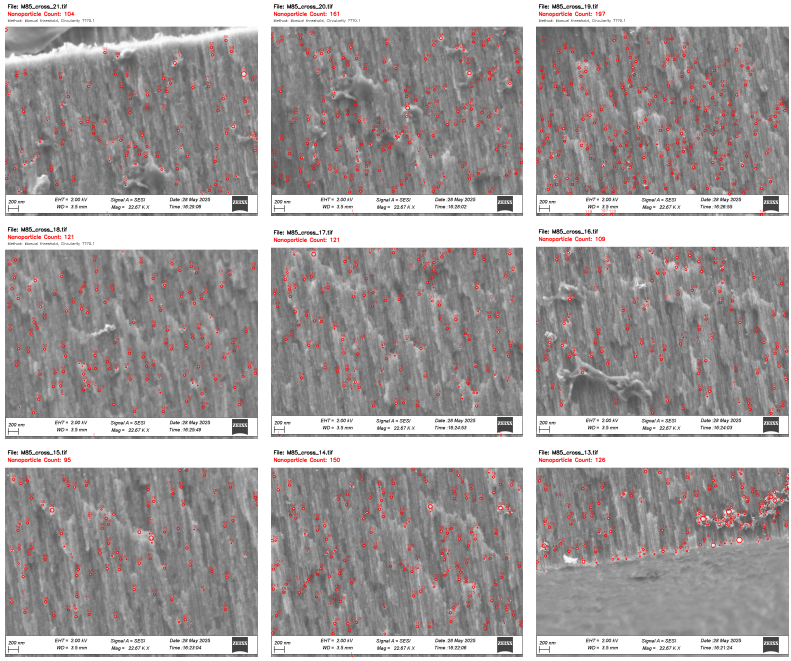


Fig. 3.6 SEM images through the whole decorated FSM with Au NPs where the red dots show the automatic detection by the Python code and count the amount of detected Au NPs.

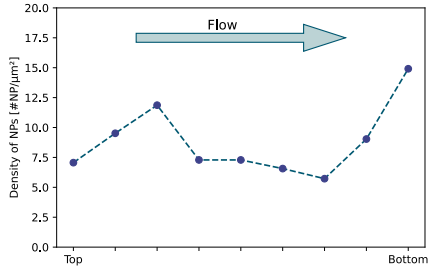


Fig. 3.7 Evolution of the density of the NPs through the whole thickness of the membrane, showing the direction of the flow of Au NPs. It can be concluded that the totality of the membrane is decorated.

By working with this microfluidic set-up instead of a drop-casting method,

we can show that the synthesized NPs are homogeneously dispersed inside the pores as it follows the flow through the pores and no coffee-ring effect is present. We also prepared a decorated FSM with the drop-casting method, for comparison purposes. In this case the drop casting method does not deposit the NPs uniformly on the FSM but follows a coffee-ring pattern, as shown in Fig. 3.8a. No particles are visible in the entire cross-section in Fig. 3.8b, only some clusters of NPs on top of the membrane that arrived there during the cleaving of the FSM for the image. No NPs were thus counted inside the thickness of the FSM and this has been validated by XPS measurement shown in Fig. 3.9, demonstrating the utility of the flow-through technique to decorate the membrane.

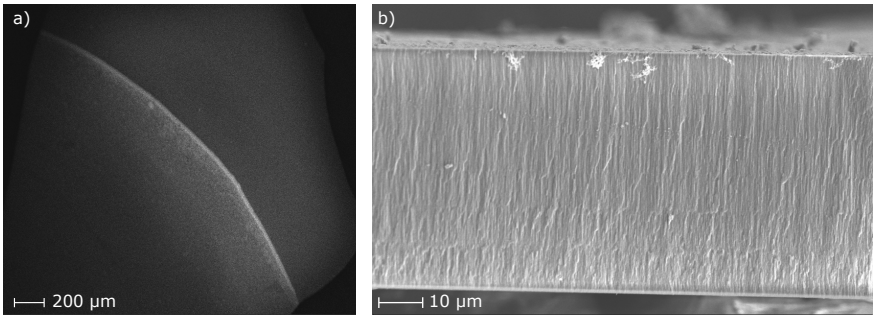


Fig. 3.8 SEM image of a) top view and b) sectional view of the FSM decorated by drop-casting.

Fig. 3.4 shows that gold (Au 4f) is well detected on the FSM decorated by flow-through while FSM decorated with the drop casting method do not exhibit Au 4f peaks in Fig. 3.9. This can be explained by the size of the analyzed area, which is only 100 µm, since the drop casting induces a deposition following a coffee-ring pattern as shown in Fig. 3.8a, we can say that the analysis spot was apparently not located exactly on the ring of the pattern. This proves once again that flow-through decoration is more homogeneous across the entire surface of the FSM.

3.3.4 Reflectance shift

The different structures described in section 2.3 (double layer FSM and Bragg mirror FSM) were decorated using the flow-through method outlined

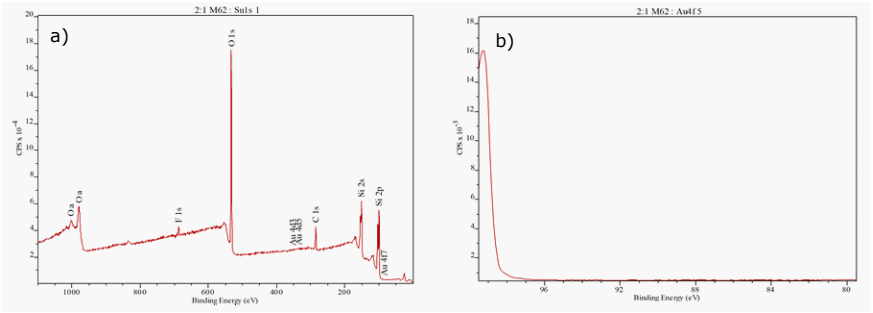


Fig. 3.9 XPS spectra of a) one FSM decorated by drop casting method and b) narrow scan of the Au 4f region.

above. Following the decoration, the reflectance spectrum of each structure exhibits a shift that depends on the type of decoration.

Double layer FSM - EOT shift

A reflectance measurement was performed on a decorated double layer membrane to evaluate the optical impact of Au NPs on the interference fringes and better understand the penetration of the NPs. As shown in Fig. 3.10a, the intensity of the reflected signal increases after decoration. This enhancement can be attributed to the mirror-like effect [179] of the Au NPs deposited on top of the FSM. In addition, a notable blueshift in the FFT of the reflectance is observed, as shown in Fig. 3.10b. The measured EOT shift of 796 nm indicates that Au NPs infiltrated the porous matrix.

This blueshift can be attributed to modifications of the PSi structure during the flow-through process. The silicon oxide can dissolve and reprecipitate in the aqueous solution, leading to a dynamic restructuring of the pore walls [201]. This process may also contribute to the retention of the NPs within the pores by promoting their mechanical anchoring.

The dissolution of SiO_2 reduces its contribution to the effective dielectric constant of the PSi layer, thereby decreasing its effective refractive index in eq. 2.1 and thus effective optical thickness This results in a blueshift of the optical response. The effect is particularly evident for the Bragg mirrors, whose stopband wavelength depends directly on the effective refractive index, as described by eq. 2.4. To verify this effect, a Bragg sample was subjected to 4 mL of PBS (pH 7) flowing through the microfluidic setup for

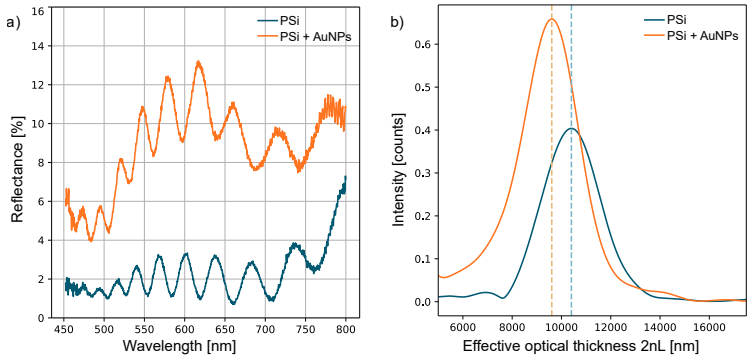


Fig. 3.10 a) Reflectance spectra of an oxidized FSM double layer, before (blue) and after (orange) decoration with Au NPs; b) corresponding Fourier transform spectra. The values of the effective optical thickness of the FFT peak for each spectrum are 10403 (PSi) nm and 9607 nm (PSi + Au NPs), showing the blueshift.

approximately 10 min. As shown in Fig. 3.11, the stopband exhibited a blueshift of 26 nm after the flow.

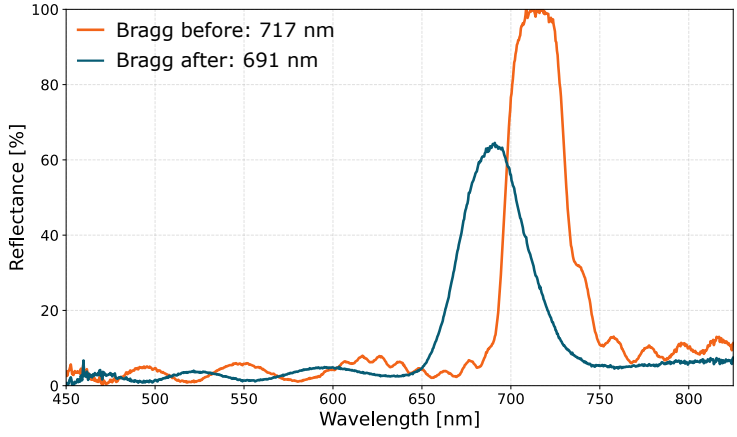


Fig. 3.11 Averaged reflectance spectra of an oxidized FSM Bragg, before (orange) and after (blue) flow of PBS.

RIFTS measurements were performed to evaluate the sensing performance of double layer FSMs with and without Au nanorods decoration. The EOT

was measured upon infiltration with liquids of different refractive indices (water, ethanol and isopropanol). The results are shown in Fig. 3.12 and demonstrate that the EOT shift is more pronounced for decorated membranes compared to undecorated ones, indicating an increased sensitivity of the sensor after nanoparticles infiltration. In addition, the standard deviation of the measurements is consistently reduced in the decorated samples, demonstrating improved reproducibility. This simultaneous enhancement in sensitivity and reduction in variability highlights the potential of decorated FSMs as promising platforms for plasmonic sensing applications.

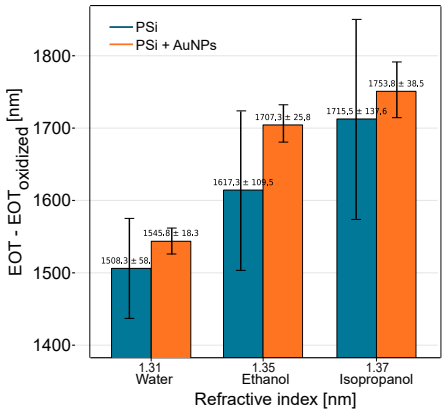


Fig. 3.12 Histogram showing the effective optical thickness (EOT) shift of oxidized PSi membranes with (orange) and without (blue) Au NPs as a function of the refractive index of the infiltrated liquid (water, ethanol, and isopropanol). The vertical bars show the standard deviation of each measure.

Bragg mirror FSM - mirror shift

The functionalization of the Bragg mirror structures was carried out using the flow-through methodology described above, in which a colloidal suspension of gold nanorods is driven through the porous membranes. As shown in Fig. 3.13, this process induces a pronounced blueshift of the stopband, which can be attributed to a modification of the effective refractive index of the porous matrix due to the dissolution of the porous silicon in aqueous solution.

The magnitude of the blueshift is primarily related to the duration of the membrane exposure to the flowing solution, as prolonged contact promotes further dissolution of the SiO_2 layer. At the same time, longer infiltration times may promote the capture of a larger number of nanoparticles within the porous structure. Therefore, although the nanoparticles themselves do not directly induce the blueshift, the shift can be used as an indirect indication of the amount of nanoparticles loaded into the membrane.

For most samples (1, 2, 3 and 5), the colloidal suspension was passed through the membrane three times to enhance nanoparticles loading, whereas sample 4 underwent only a single infiltration step. As a result, sample 4 exhibits a significantly smaller blueshift compared to sample 3, indicating a lower concentration of nanoparticles within the pores. Although the infiltration process is relatively reproducible, accurately predicting the exact spectral shift remains challenging due to the complexity of nanoparticles distribution within the porous network. Across the five samples investigated, blueshifts of 64, 70, 80, 8, and 37 nm were measured, in good agreement with the 85 nm blueshift reported in the literature [170] and with the blank test with PBS in Fig. 3.11.

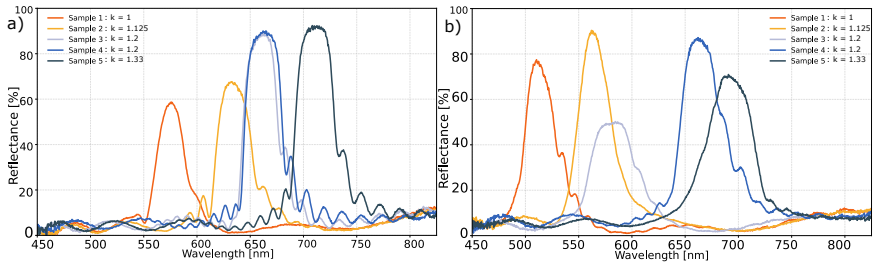


Fig. 3.13 Averaged reflectance spectra measured at normal incidence of 5 samples with scaling factor: 1 (orange), 1.125 (yellow), 1.2 (light blue and blue) and 1.33 (dark blue). a) Before the decoration and b) after the decoration.

In addition to the spectral shift, variations in reflectance intensity are also observed in Fig. 3.13. However, these changes are difficult to quantify due to competing effects. On one hand, increased light scattering induced by the intrinsic roughness of porous silicon tends to reduce the reflectance intensity [170]. On the other hand, partial metallization of the pore walls by gold

nanoparticles can enhance surface reflectivity, introducing a mirror-like contribution [179].

3.4 SERS measurement on PSi

Following the functionalization of the membranes with gold nanoparticles, SERS measurements were carried out to evaluate their performance. In a first step, the study focused on membranes with a double layer structure, consisting of a top porous layer designed for sensing and an underlying mechanically robust support layer. This configuration allows the assessment of SERS activity in a simplified architecture. In a second step, the measurements were extended to Bragg mirror FSMs in order to enhance the Raman signal and investigate the influence of photonic effects on Raman enhancement.

3.4.1 Instrumental characterization

SERS spectra were recorded using a LabRAM HR800 system coupled to a confocal microscope (Horiba Scientific). Excitation was provided by a 633 nm He–Ne laser. Spectra were collected using a 50× objective lens, a grating of 600 nm, with an acquisition of five seconds and three accumulations. For each sample five random measurements were performed.
Prior to data acquisition, the instrument was automatically calibrated by measuring the Raman response of a silicon wafer, ensuring correct peak positions and intensities at 0.0 cm^{-1} and 520.7 cm^{-1} . Baseline correction was subsequently performed using LabSpec 6 (Horiba Scientific) with a first-degree polynomial fitting procedure.

3.4.2 Sensing layer

The simplest architecture for analyte detection consists of a double layer porous silicon membrane [120]. In this configuration, the top layer, referred to as the sensing layer, is designed with relatively large pores to facilitate analyte infiltration and interaction, while the underlying layer,

with smaller pores, serves as a mechanically robust support layer. In the work of Vercauteren [9], the sensing layer thickness was reported to be 4 µm. However, it has been shown that excessively deep pores may lead to trapping of Raman-scattered photons, thereby reducing the detectable signal [195]. Based on this consideration, a thinner sensing layer of 1.8 µm with a porosity of 79% was employed in this study, combined with a support layer identical to that used in all FSMs (54 µm thickness and 55% porosity).

Following the synthesis protocol described above, the nanorods were functionalized with MGITC, a widely used Raman reporter dye that binds to gold nanoparticles through its isothiocyanate group. This was achieved by adding 50 µL of an MGITC solution (10^{-3} mol/L) to obtain a final concentration of 5×10^{-5} mol/L in a total volume of 1 mL. The corresponding SERS spectrum is shown in Fig. 3.14. The two most intense Raman bands of MGITC in the 800–1800 cm^{-1} region are observed at 1171 cm^{-1}, attributed to in-plane C–H bending, and at 1617 cm^{-1}, corresponding to phenyl–N and C–C stretching modes [202].

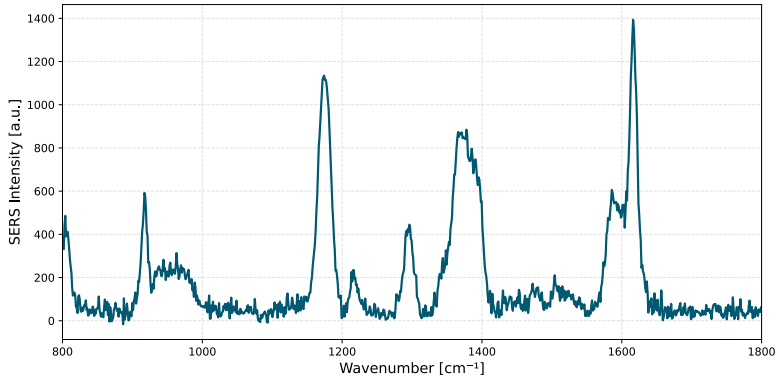


Fig. 3.14 SERS spectrum of MGITC (5×10^{-5} mol/L) measured on a sensing layer decorated with nanorods excited with a 633 nm laser source.

At the concentration used for Raman measurements (5×10^{-5} mol/L), the Raman signal of MGITC is not detectable in the absence of gold nanoparticles, confirming the necessity of plasmonic enhancement, this is shown in Fig. 3.15, where only the Raman signal of the porous silicon is visible.

This result demonstrates that the double layer FSM, once decorated with nanoparticles, provides an effective SERS-active substrate.

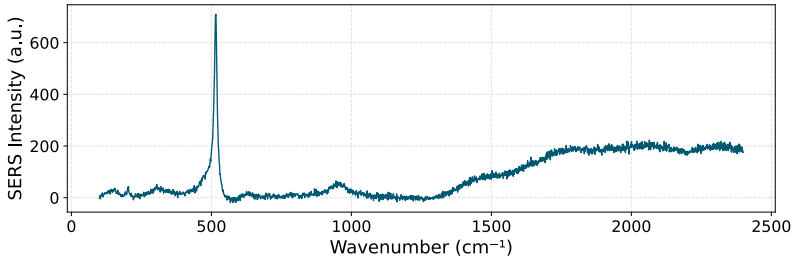


Fig. 3.15 SERS spectrum of MGITC (5×10^{-5} mol/L) measured on a sensing layer without nanorods excited with a 633 nm laser source.

3.4.3 Bragg mirror

The integration of PSi Bragg structures with plasmonic nanoparticles has attracted significant attention for SERS applications [203, 179, 204, 205, 206, 207]. By combining photonic and plasmonic effects, these hybrid systems enable enhanced light–matter interaction, leading to improved Raman signal amplification. In particular, SERS substrates based on Bragg PSi have been reported to exhibit Raman intensities 5 to 8 times higher than those obtained with single layer PSi or monocrystalline silicon substrates [203]. This enhancement translates into very low detection limits, with values reported down to 10^{-13} - 10^{-15} M for model analytes such as rhodamine 6G [203].

Effect of the sensing layer on Bragg mirror

Before investigating the influence of the Bragg mirror on the SERS response, the specific contribution of the sensing layer on the Bragg mirror is first evaluated. To this end, three samples were fabricated as explained in section 2.3 :

1. Sample 1: sensing layer + support layer
2. Sample 2: Bragg mirror (λ_s = 580 nm) + support layer
3. Sample 3: sensing layer + Bragg mirror (λ_s = 580 nm) + support layer

All these samples were decorated in the same way. The corresponding SERS intensities for these samples are presented in Fig. 3.16.

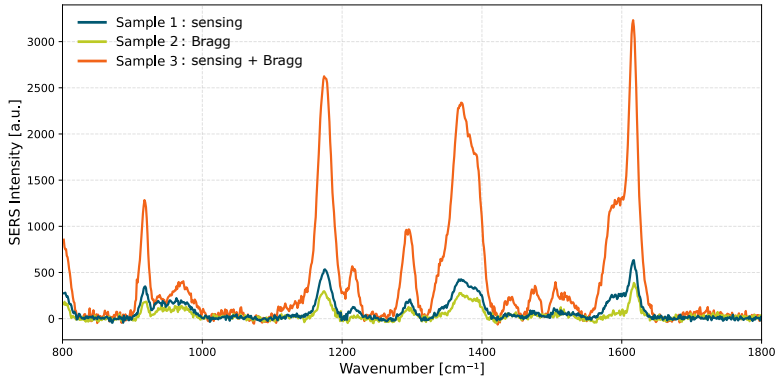


Fig. 3.16 Averaged SERS spectra of MGITC (5×10^{-5} mol/L) excited with a 633 nm laser source on decorated SERS substrate: blue) sensing FSM as in Fig. 3.14, green) Bragg FSM and orange) Bragg FSM with a sensing layer.

The results clearly show that the combination of both a sensing layer and a Bragg mirror yields the highest SERS intensity . It can be noticed that the sensing layer alone exhibits a higher signal than the Bragg mirror FSM alone. This behavior can be attributed to the role of this sensing layer in promoting the co-localization of analyte molecules and gold nanoparticles within a confined region, thereby increasing the density of electromagnetic hotspots and enhancing the probability of analyte detection [208]. In addition, the use of this identical sensing layer across all samples ensures a consistent pore size at the surface, which is critical for reliable comparison of SERS performance between different structures. These results therefore demonstrate the significant advantage of incorporating a sensing layer , both in terms of enhancing signal intensity and improving the reproducibility of the system.

The third sample, which corresponds to the reference structure (Fig. 2.23), is presented in Fig. 3.17, where the nanorod decoration can be observed. A magnified view of the support layer is also shown, in which the white dots correspond to the nanorods that flowed through the membrane and decorated the membrane homogeneously.

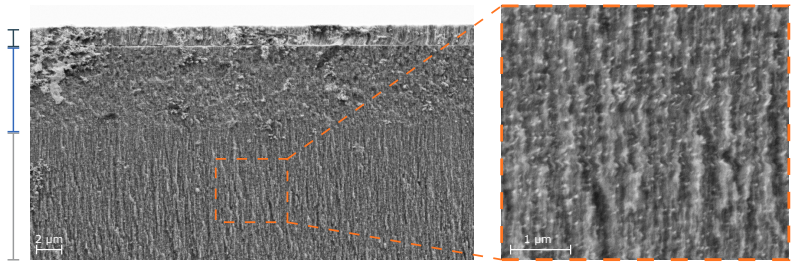


Fig. 3.17 SEM cross section of the decorated reference Bragg structure shown in Fig. 2.23. A magnified view of the support layer is presented, where the white dots correspond to the gold nanorods within the porous structure.

Influence of photonic stopband

The influence of the photonic stopband on SERS performance has been previously investigated in the literature [192, 209, 210, 208], where it has been shown that maximum signal enhancement is achieved when the excitation wavelength coincides with the stopband of the Bragg structure. Based on this principle, the SERS intensities of the five samples introduced in section 3.3.4 based on different time scaling factors, are presented in Fig. 3.18 , in order to evaluate the impact of stopband tuning on the Raman response.

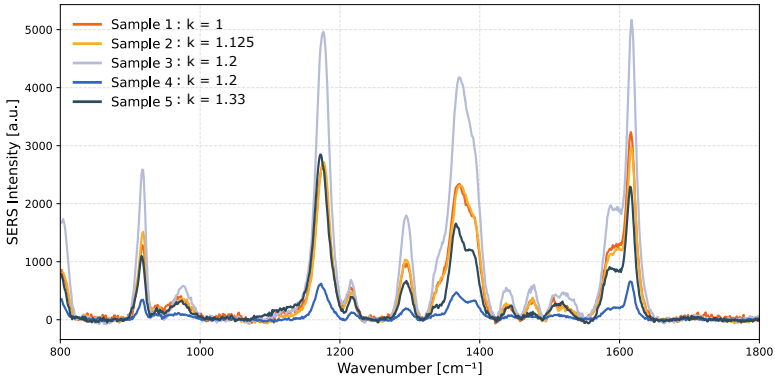


Fig. 3.18 Averaged SERS spectra of MGITC (5×10^{-5} mol/L) excited with a 633 nm laser source for 5 Bragg samples.

Fig. 3.19a presents the average SERS intensity of the Raman band at 1617

cm^{-1}. As expected, sample 3 (light blue in Fig. 3.18), whose stopband is close to the excitation wavelength of 633 nm, exhibits the highest SERS intensity. In contrast, sample 4 that had the same initial stopband as sample 3, does not follow this trend, which can be attributed to the lower gold nanoparticles loading, as the colloidal suspension was passed through the membrane only once.

To better account for variations in nanoparticles loading, the blueshift quantified above in Fig. 3.13 must be considered. The SERS intensity is plotted as a function of the observed blueshift in Fig. 3.19b, which serves as an indirect indicator of the amount of gold infiltrated into the porous structure. This representation reveals a linear relationship between increasing nanoparticles incorporation and enhanced SERS intensity.

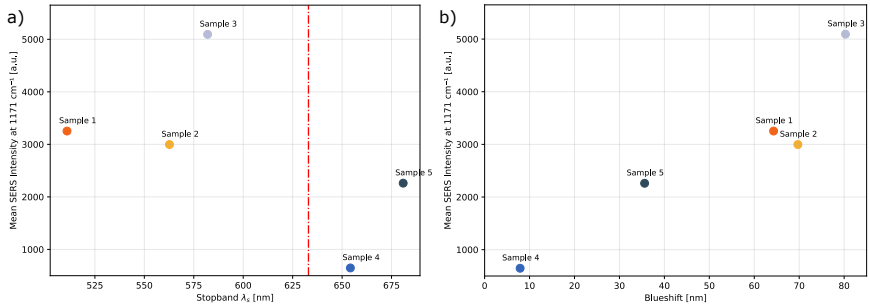


Fig. 3.19 Evolution of the mean value of the SERS intensity of the Raman band at 1617 cm^{-1} in function of a) the center of the stopband λ_s after the decoration with the red dashed line showing the excitation wavelength and b) the blueshift of the λ_s induced by the quantity of Au NPs inside the membrane.

These findings differ from other reports [211], where a decrease in Raman signal was observed with increasing deposition time, attributed to nanoparticles overgrowth and aggregation leading to a reduction in effective hotspot density. In the present work, the decoration is achieved by infiltration of pre-synthesized nanoparticles rather than through in situ growth. This approach minimizes the risk of particle coalescence or morphological changes that could reduce hotspot density. Moreover, unlike high-density deposition methods that may lead to pore clogging and reduced light penetration, as reported by Li *et al.* [156], the present method promotes a more homo-

geneous distribution of nanoparticles within the whole thickness of the porous membrane. This further highlights the advantage of the proposed functionalization strategy for achieving efficient and reproducible SERS substrates.

3.4.4 Discussion

The results reveal a clear relation between the SERS intensity and the observed blueshift, the latter being used here as an indicator of nanoparticles loading within the porous structure. As shown in Fig. 3.19b, the SERS signal increases approximately linearly with the blueshift, demonstrating that higher nanoparticles incorporation leads to a greater density of active plasmonic sites and, consequently, stronger Raman enhancement.

At the same time, the comparison between samples confirms that photonic tuning remains a critical parameter: the highest SERS intensity is obtained when the stopband is close to the excitation wavelength, in agreement with literature reports [192, 209, 210, 208].
In particular, the optimized Bragg structure exhibited an average SERS intensity of 5093 (sample 3 in Fig. 3.18), which is eight times higher than the average SERS intensity of 637 measured for the corresponding membrane without the Bragg stack (sample 1 in Fig. 3.16). This enhancement is comparable to the results reported by Wang *et al.* [203], who demonstrated that Bragg porous silicon substrates could outperform simpler porous architectures by a factor of approximately five.

These results therefore highlight a dual optimization strategy. On one hand, the stopband position should be tuned as close as possible to the excitation wavelength to maximize photonic enhancement. On the other hand, the membrane should be functionalized with the highest possible nanoparticles loading to maximize plasmonic hotspot density.

3.5 Key message

Let's sum up the important findings covered in this chapter.

Numerical simulations first highlight the **intrinsic advantage of nanoporous silicon compared to flat substrates**. An increase of 7.45 has been estimated, which correspond to the approximated factor of 5 calculated by Lu *et al.* [195], highlighting the critical role of the pore geometry on the electric field enhancement.

Building on these insights, a novel decoration approach was developed, enabling **the integration of pre-synthesized colloidal nanoparticles with controlled size and shape into freestanding porous silicon membranes**. This flow-through method ensures a homogeneous distribution of nanoparticles throughout the entire thickness of the membrane without clogging the pores. The approach is compatible with relatively low pressures and preserves the structural integrity of the membrane, which is embedded in a Kapton® holder for mechanical stability and easy integration into microfluidic systems. Importantly, this method offers a high degree of flexibility, allowing the use of nanoparticles with tailored properties, which is a key advantage for tuning plasmonic responses.

Reflectance measurements demonstrated that nanoparticles incorporation induces a measurable spectral blueshift, which can be used as an indicator of loading. In parallel, RIFTS measurements revealed an increase in sensitivity and improved reproducibility after decoration, highlighting the beneficial role of nanoparticles in enhancing the optical response of the system.

SERS measurements further confirmed the effectiveness of the decoration method. Even with relatively simple double-layer structures, a clear Raman signal was obtained, demonstrating that the sensing layer plays a crucial role in enabling efficient signal generation. Building on this baseline, the integration of Bragg mirror structures led to a significant additional enhancement. The results show that optimal SERS performance is achieved when the photonic stopband is tuned close to the excitation wavelength and when nanoparticles loading is sufficiently high. In particular, an increase

in nanoparticles incorporation, tracked via the blueshift of the reflectance spectrum, was directly correlated with stronger Raman signals, with enhancements of up to a factor of 8 observed. These findings are consistent with literature report [203] showing that Bragg porous silicon substrates can outperform simpler architectures by several-fold.

Overall, this work demonstrates that porous silicon offers a dual advantage for SERS applications: it provides a **favorable dielectric environment** for plasmonic resonance while simultaneously introducing **geometrical confinement** that enhances and spatially extends electromagnetic hotspots. When combined with photonic structures such as Bragg mirrors, this effect can be further amplified, leading to highly efficient hybrid photonic–plasmonic substrates.

Looking forward, several perspectives emerge from this work. The versatility of the flow-through decoration method opens the possibility of integrating different types of nanoparticles, potentially with controlled spatial distribution across the membrane thickness [103]. Further optimization of Bragg structures could enable even better matching with excitation conditions.
In addition, the platform could be explored for refractive-index sensing by removing the sensing layer and monitoring shifts in the Bragg resonance resulting from the infiltration of the pores by the analyte. The presence of gold nanoparticles could further enhance the sensitivity of this approach through their interaction with the optical field within the porous structure. Exploring thinner membranes may also allow signal detection from both sides, paving the way for filtering or directional sensing applications. Finally, the compatibility of these systems with flow-through configurations suggests strong potential for real-time and continuous sensing in microfluidic environments.

Conclusions and Perspectives

To conclude this thesis, we first summarize the main research questions that were addressed as well as the principal contributions brought by this work. We then compare the obtained results with the current state of the art in order to position this research within the broader context of porous silicon-based SERS substrates. Finally, the remaining challenges and future perspectives are discussed before concluding with some final remarks on the significance and outlook of this work.

⋆ Final contributions

SERS has gained increasing interest within the field of porous materials in recent years, as demonstrated throughout this thesis. In particular, PSi has recently emerged as a promising SERS substrate due to its intrinsically rough and highly developed surface morphology [176]. Compared to flat substrates, porous silicon offers a very high specific surface area, enabling efficient loading of both plasmonic nanoparticles and target analytes [189]. However, the design of an efficient porous silicon-based SERS substrate remains a complex challenge. Numerous strategies can be employed to decorate the porous structure, while plasmonic nanoparticles themselves can exhibit a wide variety of shapes, sizes, and optical properties. As a result, the development of a robust and sensitive porous silicon SERS substrate involves many interconnected parameters that must be carefully understood.

The objective of this work is therefore to design and study a porous silicon-based SERS substrate as a proof of concept. Through this approach, the aim is to establish a link between the morphology of porous silicon and the resulting SERS response, while identifying the key design parameters

influencing both signal sensitivity and reproducibility. Rather than focusing solely on achieving high performance metrics, this thesis aim to provide a deeper understanding of the mechanisms governing efficient and reliable porous silicon SERS substrates. To address this objective, four main research questions were investigated throughout this work:

RQ1: *How can a plasmonic nanoparticle be tuned to enhance the electromagnetic field?*

RQ2: *How can a porous substrate be fabricated to enable efficient decoration with plasmonic nanoparticles?*

RQ3: *How can porous silicon be decorated to enable the integration of various types of nanoparticles, and how are these nanoparticles distributed within the porous structure?*

RQ4: *What is the effect of the decorated porous substrate on the SERS signal?*

The first question was addressed in Chapter 1. In this chapter, we demonstrated the importance of distinguishing between measurements performed in liquid suspensions and those performed on dried substrates. In solid-state configurations, the formation of plasmonic hotspots between neighboring nanoparticles can significantly shift the resonance wavelength. In contrast, for colloidal suspensions, the nanoparticles themselves can induce extinction of both the excitation and Raman signals, making it essential to account for these effects when analyzing the optical response. Based on these observations, a numerical model was developed to predict both the resonance wavelength and the electromagnetic field enhancement of plasmonic nanoparticles, taking into account their size, shape, and surrounding environment. The results showed that the optimal nanoparticle design strongly depends on the targeted application and therefore needs to be evaluated on a case-by-case basis.

The second question was investigated in Chapter 2. We demonstrated that freestanding porous silicon membranes provide a rapid and efficient approach for membrane fabrication once the release step is properly understood and optimized. This fabrication method enabled the rapid exploration of various membrane architectures, showing that the release process is compatible with multiple structures ranging from simple porous layers to Bragg mirrors. These membranes were subsequently integrated into a microfluidic setup. Compared with the membranes previously developed by Roselien Vercauteren [9], the membranes fabricated in this work are thinner and

exhibit larger pore sizes, which significantly reduces the pressure required to achieve flow-through operation. As a result, the risk of mechanical failure during operation is greatly reduced.

The two final questions were addressed in Chapter 3. A simple and versatile decoration strategy was proposed, consisting of flowing a colloidal suspension of plasmonic nanoparticles through the porous membrane integrated within a microfluidic setup. This approach enabled homogeneous decoration throughout the entire membrane thickness for all investigated porous structures. The decoration process also modified the optical response of the membranes, notably through a blueshift of the EOT for double-layer structures and of the stopband position for Bragg mirrors.
Using these decorated substrates, SERS measurements were performed. The results showed that introducing a sensing layer capable of capturing gold nanoparticles at the membrane surface significantly increases the SERS signal. Furthermore, Bragg mirror structures were shown to further enhance the signal due to the improved reflection of Raman-scattered photons. The strongest enhancement was obtained when the Bragg mirror stopband was positioned close to the excitation wavelength, in agreement with previous reports from the literature. In addition, the blueshift induced by nanoparticle loading inside the membrane exhibited a linear relation with the measured SERS intensity. These observations highlight a dual optimization strategy: on the one hand, the stopband position should be tuned as close as possible to the excitation wavelength to maximize photonic enhancement; on the other hand, the membrane should incorporate the highest possible nanoparticle density in order to maximize the number of plasmonic hotspots.

Based on these findings, the ideal substrate would consist of a freestanding membrane incorporating a sensing layer at the surface, combined with a Bragg mirror positioned above a support layer. The Bragg mirror should be designed such that, after nanoparticle decoration, the stopband is centered near 633 nm. In addition, flowing the colloidal suspension through the membrane multiple times allowed to further increase the nanoparticle loading inside the pores and consequently improve the SERS enhancement. Besides optimizing the porous structure itself, the plasmonic nanoparticles also represent an important design parameter that can be tuned to further enhance the SERS response. A promising approach would consist in using gold nanorods with sufficiently small dimensions to enable efficient penetration inside the porous network. In addition, relatively small AR appear

particularly relevant for this application. Indeed, the formation of nanoparticle dimers was shown to induce an additional redshift of approximately 50 nm in the plasmonic resonance. Consequently, nanorods resonating around 580 nm before deposition would likely lead to resonances close to the 633 nm excitation wavelength once dimers are formed within the pores, corresponding to aspect ratios close to 2. Finally, it would also be highly interesting to compare the behavior of nanodumbbells and nanorods synthesized from the same seed solution once integrated inside porous silicon, in order to better understand the influence of nanoparticle geometry on both pore infiltration and SERS enhancement.

The main contributions of this thesis can be summarized as follows:

In Chapter 1, the main contribution was the combination of numerical simulations with the analytical model proposed by van Dijk *et al.* [74] in order to calculate the SERS enhancement factor in liquid suspensions. Prior to this work, the analytical model was limited to spheroidal nanoparticles. By coupling it with numerical simulations, the SERS enhancement could be evaluated for more complex geometries such as nanodumbbells, which was previously not possible.

In Chapter 2, a new fabrication approach for freestanding porous silicon membranes was proposed, enabling a rapid and simple process adaptable to a wide variety of porous structures. The membrane release was achieved through a short electropolishing step of only 3 seconds, whose parameters were optimized using numerical simulations ensuring mechanical preservation of the membrane.

In Chapter 3, a new decoration strategy was developed to enable homogeneous decoration of porous silicon membranes with various types of plasmonic nanoparticles throughout the entire membrane thickness. This approach was successfully demonstrated for several different porous structures, particularly the Bragg FSM.

Thanks to these contributions, the SERS response of porous silicon-based substrates could be systematically investigated, leading to a better understanding of the interplay between porous silicon morphology, nanoparticle distribution, and optical enhancement. This work therefore provides valuable guidelines for the design of efficient and reproducible PSi-based SERS

substrates.

⋆ Benchmarking

Benchmarking the performance of the proposed membranes with the literature is not straightforward, since the objective of this work was not solely focused on maximizing the SERS performance of the substrate, but also on understanding and analyzing the different building blocks involved in its fabrication and operation.

A first comparison can nevertheless be made with previous studies that investigated the decoration of freestanding porous silicon membranes. Most reported approaches rely on immersion plating methods to decorate the porous structure with metallic nanoparticles [143, 146, 132, 131]. Jin *et al.* [142] also demonstrated pore infiltration using a colloidal nanoparticle suspension. However, in their approach, the freestanding membranes were first fragmented into flakes through ultrasonication before being mixed with the nanoparticle suspension, thereby facilitating complete pore infiltration. In contrast, the method proposed in this work offers a novel alternative by enabling the integration of presynthesized colloidal nanoparticles with controlled size and shape directly into intact freestanding membranes through a flow-through microfluidic approach.

The numerical simulations performed in this thesis first highlighted the intrinsic advantage of nanoporous silicon compared with flat substrates. An electromagnetic field enhancement factor of approximately 7.45 was estimated, which is consistent with the enhancement factor close to 5 reported by Lu *et al.* [195]. These results emphasize the critical role played by the pore geometry in enhancing the local electromagnetic field. Although this effect was not measured experimentally in the present work, it represents an important aspect that deserves further investigation in future studies in order to better understand the contribution of the porous environment itself.

Experimentally, the average SERS signal obtained with the optimized Bragg structure was approximately eight times higher than the signal measured for the same structure without the Bragg mirror. These results are in good

agreement with several studies reported in the literature. Wang *et al.* [203] demonstrated that photonic crystal substrates produced SERS signals approximately five times higher than single-layer structures. Similarly, Zhong *et al.* [206] reported an enhancement factor 3.58 times larger for porous silicon photonic crystal substrates compared with single-layer porous silicon. Kumar *et al.* [212] observed a seven-fold increase of the SERS signal using optimized multilayer thin films compared with silver nanorod arrays. Much larger enhancement factors have also been reported in other photonic systems, such as the GaN distributed Bragg reflector substrate investigated by Wang *et al.* [213], where the SERS signal increased by nearly 75 times compared with a conventional GaN wafer.

Overall, the enhancement factors obtained in this work are therefore within the same order of magnitude as many porous and photonic SERS substrates reported in the literature. At the same time, the significantly larger enhancements demonstrated in some advanced photonic structures indicate that further optimization of the porous silicon architecture and nanoparticle configuration could still lead to substantial improvements in SERS performance.

Finally, it is also interesting to consider the overall fabrication and characterization time required for the complete process. Once all parameters had been optimized, the full workflow, including membrane fabrication, decoration with the colloidal nanoparticle solution, and Raman measurements, could be completed in less than one day. Although direct comparisons with the literature remain difficult, few studies provide detailed information regarding the total fabrication time of freestanding porous silicon membranes. To the best of our knowledge, Kan *et al.* [214] reported the fabrication of a freestanding membrane approximately 50 µm thick in less than two hours. In the present work, the membrane fabrication itself required only around 25 minutes, although the subsequent thermal oxidation step still required more than two hours.
Compared with the work of Vercauteren [9], where the complete fabrication process took over one week in an academic prototyping environment, the approach proposed in this work therefore represents a significant reduction in processing time. It should nevertheless be noted that the previous process enabled the simultaneous fabrication of an entire batch of devices on a single wafer, whereas in the present work only one membrane is fabricated at a time.

⋆ Challenges and perspectives

Several challenges remain related to this work, and multiple aspects could still be further investigated, opening the door to interesting future perspectives.

The first challenge concerns the **influence of nanoparticle geometry on the SERS response**. In this work, only gold nanorods were used to decorate the porous membranes, while many other plasmonic geometries could potentially be explored. In addition, the numerical simulations performed in this thesis mainly focused on spherical nanoparticles embedded within porous structures. However, more complex geometries are expected to generate stronger plasmonic hotspots and to significantly modify the resonance wavelength. Simulating such configurations therefore represents an important perspective for future work. This aspect has still not been extensively investigated, and only one article reporting the decoration of nanostars on porous silicon has been identified so far [215].
A natural continuation of this work would therefore consist in decorating the membranes with different nanoparticle geometries and even combining several shapes in order to further enhance the SERS signal. Preliminary experiments have already been performed using gold nanostars flowed through the membrane, as illustrated in Fig. 1.

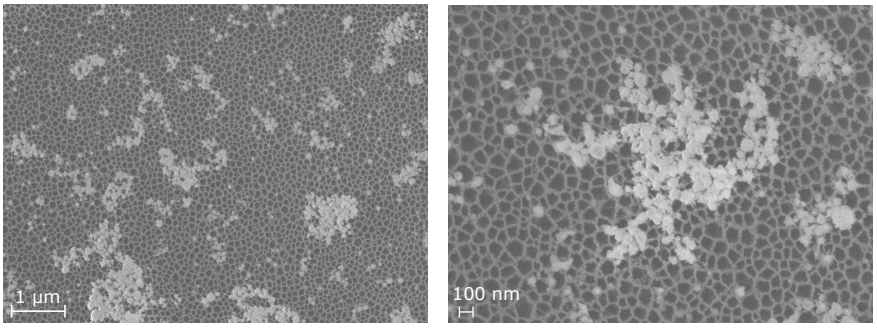


Fig. 1 SEM images of gold nanostars decorating a Bragg FSM after flow-through deposition.

Another important challenge is related to the **mechanical fragility** of the

FSM, which are relatively thin (≈ 50 µm) and can easily break if not handled carefully. The most critical step occurs during integration within the microfluidic cell. If the membrane is not perfectly aligned with the sealing joint, it frequently breaks when the pressure is released during cell opening. In practice, membrane failure occurred in nearly 80% of the experiments due to the difficulty of achieving proper alignment. While this was not critical for the present work, since SERS measurements could still be performed on partially broken membranes, it would be highly beneficial to redesign the Kapton holder or the microfluidic assembly to improve mechanical stability and allow membrane reuse after opening the cell.

Another challenge would be the fabrication of even **thinner freestanding membranes** in order to enable backside SERS measurements after analyte filtration through the membrane. Up to now, no measurable SERS signal has been obtained from the backside of the membranes. Preliminary experiments showed that the thinnest fully intact membrane that could still be manipulated reliably had a thickness of approximately 20 µm. Nevertheless, further optimization of the porosity and membrane architecture may make thinner and mechanically stable membranes achievable.

Another important challenge concerns the **repeatability** and statistical validation of the SERS measurements. In this work, the experiments were mainly performed as a proof of concept, and each membrane configuration was therefore investigated only once. Although the reported SERS signals correspond to averages obtained from multiple measurements performed at different locations on the same membrane, the full experiments themselves were not repeated on several independently fabricated samples. Future work should therefore focus on systematically repeating the experiments on multiple membranes and over several fabrication batches in order to validate the robustness, repeatability, and reliability of the proposed porous silicon-based SERS platform.

The final and perhaps most important challenge concerns the **biological aspect of the detection platform**, namely the measurement of the SERS signal originating from bacterial species or bacterial lysates. This aspect was not investigated in the present work but remains central for future biosensing applications. The use of bacterial lysates appears particularly promising, since bacteria can be selectively lysed using bacteriophages, after which the resulting lysate (composed of fragments typically smaller than

100 nm), could flow through the porous membrane [9]. However, the Raman properties of bacterial lysates still need to be thoroughly investigated. As discussed during a conference with Dr. Nathalie Lidgi-Guigui [216], biological SERS measurements remain extremely challenging because the measured signal depends on numerous parameters such as analyte orientation, zeta potential, local environment, and molecular interactions with the plasmonic surface. The complexity of the biological analyte itself therefore already represents a major limitation for the detection platform. Several studies have nevertheless demonstrated the potential of SERS for bacterial analysis [217, 218, 219]. An additional open question concerns whether the bacterial lysate should be attached onto the nanoparticles or instead simply flow through the already decorated membrane. This question is currently being investigated by Louise Lejeune using the Bragg membranes that exhibited the highest SERS enhancement in this work, and I sincerely expect that this challenge can successfully be addressed in the near future.

⋆ Final words

This work was not intended as a race toward achieving the lowest possible limit of detection. Instead, the main objective of this thesis was to better understand the porous silicon SERS substrate itself and to identify the different physical mechanisms governing the SERS response. Throughout this work, it became clear how complex such systems are, involving numerous interconnected parameters ranging from nanoparticle properties to porous structure morphology and optical interactions. In order to better understand these phenomena, the problem was intentionally divided into several building blocks, allowing each aspect of the platform to be investigated separately before combining them into a complete SERS substrate.

Through this progressive approach, the results obtained throughout this thesis suggest that the field remains highly promising. Over the past four years of this work, we could appreciate the increase of conference presentations/posters that focused on plasmonic nanoparticles and porous silicon structures, highlighting the growing interest in this research area and the potential of porous silicon for future SERS-based biosensing applications.

Beyond the scientific results themselves, perhaps the most important aspect of this thesis is the multidisciplinary nature of the work. The research combined nanoparticle characterization, porous material engineering, numerical simulations, microfabrication processes, microfluidic integration, and optical measurements, all ultimately directed toward biological sensing applications. Such a multidisciplinary approach would not have been possible without the collaboration with Louise Lejeune, whose expertise in plasmonic nanoparticles greatly contributed to this work. We hope that this modest contribution to the field of porous silicon biosensors will help open new perspectives and inspire future developments and challenges in the field.

Appendix

The codes developed during this work are publicly available on my GitHub repository: *[https://github.com/clementinegevers]*. The repository contains the following tools:

- **Count-NPs-in-PSi**: Python code for automatically counting the number of nanoparticles located within porous silicon from SEM images.
- **Carac-pore-size**: MATLAB code for analyzing pore sizes from SEM images acquired at different current densities.
- **SERS-analytical-calculation-in-colloidal-suspension**: Python scripts for comparing SERS signals calculated using the analytical model proposed by van Dijk et al. (DOI: 10.1021/jz4005043) with numerical simulations performed using COMSOL Multiphysics. Numerical simulation results for a gold nanosphere are provided in the repository, allowing the code to be run directly. The scripts can subsequently be adapted to other nanoparticle geometries by importing the corresponding COMSOL output files.
- **Keithley_command_PSi_fab**: MATLAB code for controlling a Keithley 2460 SourceMeter during the fabrication of porous silicon. The current-density profile can be adapted to fabricate porous silicon structures with different desired morphologies.

Bibliography

[1] "Antimicrobial resistance." [Online]. Available: https://www.who.int/europe/news-room/fact-sheets/item/antimicrobial-resistance

[2] C. J. L. Murray, "Global burden of bacterial antimicrobial resistance in 2019: a systematic analysis," *The Lancet*, vol. 399, no. 10325, pp. 629–655, Feb. 2022. [Online]. Available: https://www.thelancet.com/journals/lancet/article/PIIS0140-6736(21)02724-0/fulltext

[3] J. Nammi, R. Pasala, N. Andhe, R. Vasam, A. D. Poruri, and R. R. Sherikar, "Antibiotic Misuse: An In-Depth Examination of Its Global Consequences and Public Health Challenges," *Cureus*, vol. 17, no. 6, p. e85941, 2025. [Online]. Available: https://pmc.ncbi.nlm.nih.gov/articles/PMC12256094/

[4] M. U. Khan, M. M. Rahman, N. Zahan, M. K. Masud, S. Sarker, and M. H. Haque, "Electrochemical Biosensing for Antibiotic-Resistant Bacteria: Advances, Challenges, and Future Directions," *Micromachines*, vol. 16, no. 9, p. 986, Sep. 2025. [Online]. Available: https://www.mdpi.com/2072-666X/16/9/986

[5] M. Banakar, M. Hamidi, Z. Khurshid, M. S. Zafar, J. Sapkota, R. Azizian, and D. Rokaya, "Electrochemical Biosensors for Pathogen Detection: An Updated Review," *Biosensors*, vol. 12, no. 11, p. 927, Nov. 2022. [Online]. Available: https://www.mdpi.com/2079-6374/12/11/927

[6] M. Shahrashoob, M. Dehshiri, V. Yousefi, M. Moassesfar, H. Saberi, F. Molaabasi, Y. Zare, and K. Y. Rhee, "Optical and Electrochemical Biosensors for Detection of Pathogens Using Metal Nanoclusters: A Systematic Review," *Biosensors*, vol. 15, no. 7, p. 460, Jul. 2025. [Online]. Available: https://www.mdpi.com/2079-6374/15/7/460

[7] N. Couniot, "Highly-sensitive CMOS capacitive biosensors towards detection of single bacterial cell in electrolyte solutions," Ph.D. dissertation, UCLouvain, 2015.

[8] J. Rasson, "Stable porous silicon-based optical sensing platform towards detection of bacterial lysis," Ph.D. dissertation, UCLouvain, 2018.

[9] R. Vercauteren, "Porous silicon flow-through membrane: application to the optical detection of bacteria from their lysate," Ph.D. dissertation, UCLouvain, 2022.

[10] C. M. Buchanan, R. L. Wood, T. R. Hoj, M. Alizadeh, C. G. Bledsoe, M. E. Wood, D. S. McClellan, R. Blanco, C. L. Hickey, T. V. Ravsten, G. A. Husseini, R. A. Robison, and W. G. Pitt, "Rapid separation of very low concentrations of bacteria from blood," *Journal of Microbiological Methods*, vol. 139, pp. 48–53, Aug. 2017. [Online]. Available: https://nchr.elsevierpure.com/en/publications/rapid-separation-of-very-low-concentrations-of-bacteria-from-bloo/

[11] T.-H. Huang, Y.-L. Tzeng, and R. M. Dickson, "FAST: Rapid determinations of antibiotic susceptibility phenotypes using label-free cytometry," *Cytometry. Part A: The Journal of the International Society for Analytical Cytology*, vol. 93, no. 6, pp. 639–648, Jun. 2018.

[12] L. Samuel, "Direct Detection of Pathogens in Bloodstream During Sepsis: Are We There Yet?" *The Journal of Applied Laboratory Medicine*, vol. 3, no. 4, pp. 631–642, Jan. 2019. [Online]. Available: https://doi.org/10.1373/jalm.2018.028274

[13] Y. L. Naboka, A. R. Mavzyiutov, M. I. Kogan, I. A. Gudima, S. N. Ivanov, and K. G. Naber, "Does *Escherichia coli* have pathogenic potential at a low level of bacteriuria in recurrent, uncomplicated urinary tract infection?" *International Journal of Antimicrobial Agents*, vol. 56, no. 1, p. 105983, Jul. 2020. [Online]. Available: https://www.sciencedirect.com/science/article/pii/S0924857920301400

[14] N. Massad-Ivanir, G. Shtenberg, and E. Segal, "Optical Detection of E. coli Bacteria by Mesoporous Silicon Biosensors," *Journal of visualized experiments : JoVE*, Dec. 2013.

[15] K. Urmann, S. Arshavsky-Graham, J. G. Walter, T. Scheper, and E. Segal, "Whole-cell detection of live lactobacillus acidophilus on aptamer-decorated porous silicon biosensors," *Analyst*, vol. 141, no. 18, pp. 5432–5440, Aug. 2016. [Online]. Available: https://pubs.rsc.org/en/content/articlelanding/2016/an/c6an00810k

[16] E. Tenenbaum and E. Segal, "Optical biosensors for bacteria detection by a peptidomimetic antimicrobial compound," *Analyst*, vol. 140, no. 22, pp. 7726–7733, Oct. 2015. [Online]. Available: https://pubs.rsc.org/en/content/articlelanding/2015/an/c5an01717c

[17] K. Urmann, E. Tenenbaum, J. Walter, and E. Segal, "Porous Silicon Biosensors Employing Emerging Capture Probes," Jul. 2015, vol. 220, pp. 93–116.

[18] C. RoyChaudhuri, "A review on porous silicon based electrochemical biosensors: Beyond surface area enhancement factor," *Sensors and Actuators B: Chemical*, vol. 210, pp. 310–323, 2015.

[19] K. Guo, M. Alba, G. P. Chin, Z. Tong, B. Guan, M. J. Sailor, N. H. Voelcker, and B. Prieto-Simón, "Designing Electrochemical Biosensing Platforms Using Layered Carbon-Stabilized Porous Silicon Nanostructures," *ACS Applied Materials & Interfaces*, vol. 14, no. 13, pp. 15 565–15 575, Apr. 2022. [Online]. Available: https://doi.org/10.1021/acsami.2c02113

[20] R. Sánchez-Salcedo and N. H. Voelcker, "Porous silicon electrochemical biosensor for non-invasive monitoring of lactation biomarkers," *npj Biosensing*, vol. 3, no. 1, p. 25, May 2026. [Online]. Available: https://www.nature.com/articles/s44328-026-00085-y

[21] V. K. Chalka, K. Rangra, and S. Dhanekar, "Rapid and Sensitive Electrochemical Detection of Escherichia coli in Water Using Cr–Au IDE-Porous Silicon Sensor," *IEEE Sensors Letters*, vol. 9, no. 2, pp. 1–4, Feb. 2025. [Online]. Available: https://ieeexplore.ieee.org/document/10815630

[22] K. A. Gonchar, D. A. Nazarovskaia, P. A. Domnin, O. D. Gyuppenen, A. A. Erokhina, M. Wang, I. I. Tsiniaikin, A. A. Eliseev, S. A. Ermolaeva, and L. A. Osminkina, "AuAg-Modified Porous Silicon Nanowires for Dual-Mode Interferometric and SERS-Based Bacterial Detection," *ACS Applied Materials & Interfaces*,

vol. 17, no. 23, pp. 33 691–33 700, Jun. 2025. [Online]. Available: https://doi.org/10.1021/acsami.5c06953

[23] C.-C. Lu, H.-H. Hsu, I.-A. Lin, V. K. S. Hsiao, and C.-C. Chu, "Simultaneous Electrochemical Formation of Porous Silicon and Noble NPs for Au Nucleation Sites in SERS Substrates," *ACS Materials Au*, vol. 6, no. 2, pp. 364–378, Mar. 2026. [Online]. Available: https://doi.org/10.1021/acsmaterialsau.5c00169

[24] D. Muthukumar, M. Naim, D. N. Kumar, N. Massad-Ivanir, M. Shemesh, and G. Shtenberg, "Sensitive *Escherichia coli* detection using porous Si immunosensor coupled with rapid catalytic signal amplification," *Sensors and Actuators B: Chemical*, vol. 394, p. 134479, Nov. 2023. [Online]. Available: https://www.sciencedirect.com/science/article/pii/S0925400523011942

[25] D. Muthukumar and G. Shtenberg, "SERS-Based Immunosensor for E. coli Contaminants Detection in Milk Using Silver-Coated Nanoporous Silicon Substrates," Rochester, NY, Sep. 2022. [Online]. Available: https://papers.ssrn.com/abstract=4213467

[26] H. V. Bandarenka, "SERS Analysis with Porous Silicon," in *Handbook of Porous Silicon*. Springer, Cham, 2016, pp. 1–21. [Online]. Available: https://link.springer.com/rwe/10.1007/978-3-319-04508-5_107-1

[27] N. Khinevich, H. Bandarenka, S. Zavatski, K. Girel, A. Tamulevičienė, T. Tamulevičius, and S. Tamulevičius, "Porous silicon - A versatile platform for mass-production of ultrasensitive SERS-active substrates," *Microporous and Mesoporous Materials*, vol. 323, p. 111204, Aug. 2021. [Online]. Available: https://www.sciencedirect.com/science/article/pii/S1387181121003309

[28] Y. Hu, S. Jiang, S. Du, Z. He, M. Zhu, Y. Shen, W. Gong, and Z. Huang, "Three-dimensional liquid freestanding membranes for reproducible and robust SERS detection," *Microchemical Journal*, vol. 224, p. 117571, May 2026. [Online]. Available: https://www.sciencedirect.com/science/article/pii/S0026265X26007733

[29] F. Xu, M. Xuan, Z. Ben, W. Shang, and G. Ma, "Surface enhanced Raman scattering analysis with filter-based enhancement substrates: A mini review," *Reviews in Analytical Chemistry*, vol. 40, no. 1, pp. 75–92, Jan. 2021. [Online]. Available: https://www.degruyterbrill.c

om/document/doi/10.1515/revac-2021-0126/html?srsltid=AfmBOortpWWgrwalRd2GiXIdusMfOqs5074RiWo4qrU47Wq4mv6F9EGg&lang=de

[30] E. C. Le Ru and P. G. Etchegoin, *Principles of surface-enhanced Raman spectroscopy: and related plasmonic effects*, 1st ed. Amsterdam ; Boston: Elsevier, 2009.

[31] A. Verdin, "Development of SERS nanotags for the detection of cancer-related markers in cells and tissues," Sep. 2023. [Online]. Available: https://orbi.uliege.be/handle/2268/306444

[32] C. V. Raman and K. S. Krishnan, "A New Type of Secondary Radiation," *Nature*, vol. 121, no. 3048, pp. 501–502, Mar. 1928. [Online]. Available: https://www.nature.com/articles/121501c0

[33] P. Platzman and P. Wolff, "Waves and interactions in solid state plasmas," 1973. [Online]. Available: https://www.semanticscholar.org/paper/Waves-and-interactions-in-solid-state-plasmas-Platzman-Wolff/eead1733105ba7eb7e5c639cc7199e12231fe71c

[34] M. N. Polyanskiy, "Refractiveindex.info database of optical constants," *Scientific Data*, vol. 11, no. 1, p. 94, Jan. 2024. [Online]. Available: https://www.nature.com/articles/s41597-023-02898-2

[35] J. W. Jr, "A New Radiation: C.V. Raman and the Dawn of Quantum Spectroscopy, Part I | Spectroscopy Online," May 2026. [Online]. Available: https://www.spectroscopyonline.com/view/a-new-radiation-c-v-raman-and-the-dawn-of-quantum-spectroscopy-part-i

[36] E. C. Le Ru and P. G. Etchegoin, "Rigorous justification of the $|E|^4$ enhancement factor in Surface Enhanced Raman Spectroscopy," *Chemical Physics Letters*, vol. 423, no. 1, pp. 63–66, May 2006. [Online]. Available: https://www.sciencedirect.com/science/article/pii/S0009261406003642

[37] Z. Starowicz, R. Wojnarowska-Nowak, P. Ozga, and E. M. Sheregii, "The tuning of the plasmon resonance of the metal nanoparticles in terms of the SERS effect," *Colloid and Polymer Science*, vol. 296, no. 6, pp. 1029–1037, Jun. 2018. [Online]. Available: https://doi.org/10.1007/s00396-018-4308-9

[38] E. Ringe, M. R. Langille, K. Sohn, J. Zhang, J. Huang, C. A. Mirkin, R. P. Van Duyne, and L. D. Marks, "Plasmon Length: A Universal Parameter to Describe Size Effects in Gold Nanoparticles," *The Journal of Physical Chemistry Letters*, vol. 3, no. 11, pp. 1479–1483, Jun. 2012. [Online]. Available: https://doi.org/10.1021/jz300426p

[39] J. J. Mock, M. Barbic, D. R. Smith, D. A. Schultz, and A. Et., "Shape effects in plasmon resonance of individual colloidal silver nanoparticles," *The Journal of Chemical Physics*, 2002. [Online]. Available: https://sci-hub.st/10.1063/1.1462610

[40] Y. Hang, A. Wang, and N. Wu, "Plasmonic silver and gold nanoparticles: shape- and structure-modulated plasmonic functionality for point-of-caring sensing, bio-imaging and medical therapy," *Chemical Society Reviews*, vol. 53, no. 6, pp. 2932–2971, Mar. 2024. [Online]. Available: https://pubs.rsc.org/en/content/articlelanding/2024/cs/d3cs00793f

[41] A. Agrawal, I. Kriegel, and D. J. Milliron, "Shape-Dependent Field Enhancement and Plasmon Resonance of Oxide Nanocrystals," *The Journal of Physical Chemistry C*, vol. 119, no. 11, pp. 6227–6238, Mar. 2015. [Online]. Available: https://doi.org/10.1021/acs.jpcc.5b01648

[42] T. Bulavinets, V. Rokhiv, V. Akopian, B. Bulavinets, M. Hladun, and I. Yaremchuk, "Impact of shape on plasmon resonance in single silver nanoparticles: theoretical study," *Molecular Crystals and Liquid Crystals*, vol. 769, no. 15-18, pp. 1360–1371, Nov. 2025. [Online]. Available: https://doi.org/10.1080/15421406.2025.2521883

[43] C. J. Murphy, T. K. Sau, A. M. Gole, C. J. Orendorff, J. Gao, L. Gou, S. E. Hunyadi, and T. Li, "Anisotropic Metal Nanoparticles: Synthesis, Assembly, and Optical Applications," *The Journal of Physical Chemistry B*, vol. 109, no. 29, pp. 13 857–13 870, Jul. 2005. [Online]. Available: https://doi.org/10.1021/jp0516846

[44] N. Li, P. Zhao, and D. Astruc, "Anisotropic Gold Nanoparticles: Synthesis, Properties, Applications, and Toxicity," *Angewandte Chemie International Edition*, vol. 53, no. 7, pp. 1756–1789, 2014. [Online]. Available: https://onlinelibrary.wiley.com/doi/abs/10.1002/anie.201300441

[45] K. R. Zürbes, E. Mani, and S. Bandyopadhyay, "Synthesis of anisotropic gold nanoparticles in binary surfactant mixtures: a review on mechanisms of particle formation," *RSC Advances*, vol. 15, no. 6, pp. 4377–4407, Feb. 2025. [Online]. Available: https://pubs.rsc.org/en/content/articlelanding/2025/ra/d4ra06358a

[46] L. Boselli, H. Lopez, W. Zhang, Q. Cai, V. A. Giannone, J. Li, A. Moura, J. M. de Araujo, J. Cookman, V. Castagnola, Y. Yan, and K. A. Dawson, "Classification and biological identity of complex nano shapes," *Communications Materials*, vol. 1, no. 1, p. 35, Jun. 2020. [Online]. Available: https://www.nature.com/articles/s43246-020-0033-2

[47] H. Zhang, R. Wang, D. Sikdar, L. Wu, J. Sun, N. Gu, and Y. Chen, "Plasmonic Superlattice Membranes Based on Bimetallic Nano-Sea Urchins as High-Performance Label-Free Surface-Enhanced Raman Spectroscopy Platforms," *ACS Sensors*, vol. 7, no. 2, pp. 622–631, Feb. 2022. [Online]. Available: https://doi.org/10.1021/acssensors.1c02556

[48] S. Das, K. Saxena, J.-C. Tinguely, A. Pal, N. L. Wickramasinghe, A. Khezri, V. Dubey, A. Ahmad, V. Perumal, R. Ahmad, D. N. Wadduwage, B. S. Ahluwalia, and D. S. Mehta, "SERS Nanowire Chip and Machine Learning-Enabled Classification of Wild-Type and Antibiotic-Resistant Bacteria at Species and Strain Levels," *ACS Applied Materials & Interfaces*, vol. 15, no. 20, pp. 24 047–24 058, May 2023. [Online]. Available: https://doi.org/10.1021/acsami.3c00612

[49] T. V. Tsoulos and L. Fabris, "Interface and Bulk Standing Waves Drive the Coupling of Plasmonic Nanostar Antennas," *The Journal of Physical Chemistry C*, vol. 122, no. 50, pp. 28 949–28 957, Dec. 2018. [Online]. Available: https://pubs.acs.org/doi/10.1021/acs.jpcc.8b09263

[50] L. V. Melendez, S. J. Barrow, A. Liu, T. U. Connell, and D. E. Gómez, "Breaking plasmonic symmetry through the asymmetric growth of gold nanorods," *Optica*, vol. 7, no. 12, p. 1666, Dec. 2020. [Online]. Available: https://opg.optica.org/abstract.cfm?URI=optica-7-12-1666

[51] D. M. Solís, J. M. Taboada, F. Obelleiro, L. M. Liz-Marzán, and F. J. García de Abajo, "Optimization of Nanoparticle-Based SERS Substrates through Large-Scale Realistic Simulations," *ACS*

Photonics, vol. 4, no. 2, pp. 329–337, Feb. 2017. [Online]. Available: https://doi.org/10.1021/acsphotonics.6b00786

[52] A. Chícharo, A. Teixeira, D. Moreira, M. S. Relvas, M. Aranda, T. Douglas, J. Borme, J. B. Nieder, L. Diéguez, and S. Abalde-Cela, "Precision-Engineered Plasmonic Nanostar Arrays for High-Performance SERS Sensing," *Advanced Optical Materials*, vol. 13, no. 34, p. e01275, 2025. [Online]. Available: https://onlinelibrary.wiley.com/doi/abs/10.1002/adom.202501275

[53] K. Wang and J. Li, "Reliable SERS detection of pesticides with a large-scale self-assembled Au@4-MBA@Ag nanoparticle array," *Spectrochimica Acta Part A: Molecular and Biomolecular Spectroscopy*, vol. 263, p. 120218, Dec. 2021. [Online]. Available: https://www.sciencedirect.com/science/article/pii/S1386142521007952

[54] M. P. Mcoyi, K. T. Mpofu, M. Sekhwama, and P. Mthunzi-Kufa, "Developments in Localized Surface Plasmon Resonance," *Plasmonics*, vol. 20, no. 7, pp. 5481–5520, Jul. 2025. [Online]. Available: https://doi.org/10.1007/s11468-024-02620-x

[55] R. K. Saini, A. Kumar, V. Goyal, A. Agarwal, and R. Prajesh, "Evaluating EM-field enhancement of different shapes of metallic nanoparticles using COMSOL multiphysics for SERS-based sensors," *Materials Today: Proceedings*, vol. 76, pp. 383–387, Jan. 2023. [Online]. Available: https://www.sciencedirect.com/science/article/pii/S2214785322072765

[56] R. K. Saini, A. K. Sharma, A. Agarwal, and R. Prajesh, "Near field FEM simulations of plasmonic gold nanoparticle based SERS substrate with experimental validation," *Materials Chemistry and Physics*, vol. 287, p. 126288, Aug. 2022. [Online]. Available: https://www.sciencedirect.com/science/article/pii/S0254058422005946

[57] R. Pilot, R. Signorini, C. Durante, L. Orian, M. Bhamidipati, and L. Fabris, "A Review on Surface-Enhanced Raman Scattering," *Biosensors*, vol. 9, no. 2, p. 57, Apr. 2019. [Online]. Available: https://www.mdpi.com/2079-6374/9/2/57

[58] Y. S. Yamamoto, Y. Ozaki, and T. Itoh, "Recent progress and frontiers in the electromagnetic mechanism of surface-enhanced Raman scattering," *Journal of Photochemistry and Photobiology C: Photochemistry*

Reviews, 2014. [Online]. Available: https://sci-hub.st/10.1016/j.jphotochemrev.2014.10.001

[59] B. J. Sumlin, W. R. Heinson, and R. K. Chakrabarty, "Retrieving the aerosol complex refractive index using PyMieScatt: A Mie computational package with visualization capabilities," *Journal of Quantitative Spectroscopy and Radiative Transfer*, vol. 205, pp. 127–134, Jan. 2018. [Online]. Available: https://www.sciencedirect.com/science/article/pii/S0022407317305836

[60] C. Bohren and D. Huffman, "Absorption and Scattering of Light by Small Particles | Wiley Online Books," 1998. [Online]. Available: https://onlinelibrary.wiley.com/doi/book/10.1002/9783527618156

[61] G. Mie, "Contributions to the Optics of Turbid Media, Particularly of Colloidal Metal solutions. Annalen der Physik, 25, 377-445. - References - Scientific Research Publishing," 1908. [Online]. Available: https://www.scirp.org/reference/referencespapers?referenceid=2124153

[62] S. Asano and G. Yamamoto, "Light Scattering by a Spheroidal Particle," *Applied Optics*, 1975. [Online]. Available: https://sci-hub.st/10.1364/ao.14.000029

[63] A. F. Oskooi, D. Roundy, M. Ibanescu, P. Bermel, J. D. Joannopoulos, and S. G. Johnson, "Meep: A flexible free-software package for electromagnetic simulations by the FDTD method," *Computer Physics Communications*, vol. 181, no. 3, pp. 687–702, Mar. 2010. [Online]. Available: https://www.sciencedirect.com/science/article/pii/S001046550900383X

[64] [Online]. Available: https://www.astro.princeton.edu/~draine/DDSCAT.6.1.html

[65] [Online]. Available: https://github.com/adda-team/adda

[66] J. Grand and E. C. Le Ru, "Practical Implementation of Accurate Finite-Element Calculations for Electromagnetic Scattering by Nanoparticles," vol. 15, no. 1, pp. 109–121. [Online]. Available: http://link.springer.com/10.1007/s11468-019-01014-8

[67] P. B. Johnson and R. W. Christy, "Optical Constants of the Noble Metals," vol. 6, no. 12, pp. 4370–4379. [Online]. Available: https://link.aps.org/doi/10.1103/PhysRevB.6.4370

[68] X. Huang, S. Neretina, and M. A. El-Sayed, "Gold Nanorods: From Synthesis and Properties to Biological and Biomedical Applications," *Advanced Materials*, 2009. [Online]. Available: https://sci-hub.box/10.1002/adma.200802789

[69] R. Gans, "Über die Form ultramikroskopischer Goldteilchen," *Annalen der Physik*, vol. 342, no. 5, pp. 881–900, 1912. [Online]. Available: https://onlinelibrary.wiley.com/doi/abs/10.1002/andp.19123420503

[70] A. Engel, F. Drault, S. M. Demoustier-Champagne, and S. Hermans, "High Yield Au Nanorods Synthesis: Investigation of the Synthesis Parameters Tunability by Statistical Methods," *Langmuir*, vol. 41, no. 25, pp. 15 805–15 818, Jul. 2025. [Online]. Available: https://doi.org/10.1021/acs.langmuir.5c00326

[71] Yu, S.-S. Chang, C.-L. Lee, and C. Wang, "Gold Nanorods: Electrochemical Synthesis and Properties and Optical Properties," *The Journal of Physical Chemistry B*, vol. 101, no. 34, pp. 6661–6664, 1997. [Online]. Available: https://doi.org/10.1021/jp971656q

[72] K. Park, S. Biswas, S. Kanel, D. Nepal, and R. A. Vaia, "Engineering the Optical Properties of Gold Nanorods: Independent Tuning of Surface Plasmon Energy, Extinction Coefficient, and Scattering Cross Section," *The Journal of Physical Chemistry C*, vol. 118, no. 11, pp. 5918–5926, Mar. 2014. [Online]. Available: https://doi.org/10.1021/jp5013279

[73] K.-S. Lee and M. A. El-Sayed, "Dependence of the Enhanced Optical Scattering Efficiency Relative to That of Absorption for Gold Metal Nanorods on Aspect Ratio, Size, End-Cap Shape, and Medium Refractive Index," *The Journal of Physical Chemistry B*, 2005. [Online]. Available: https://sci-hub.st/10.1021/jp054385p

[74] T. van Dijk, S. T. Sivapalan, B. M. DeVetter, T. K. Yang, M. V. Schulmerich, C. J. Murphy, R. Bhargava, and P. S. Carney, "Competition Between Extinction and Enhancement in Surface-Enhanced Raman Spectroscopy," vol. 4, no. 7, pp. 1193–1196. [Online]. Available: https://doi.org/10.1021/jz4005043

[75] M. N'Gom, S. Li, G. Schatz, R. Erni, A. Agarwal, N. Kotov, and T. B. Norris, "Electron-beam mapping of plasmon resonances in electromagnetically interacting gold nanorods," *Physical Review B*, vol. 80, no. 11, p. 113411, Sep. 2009. [Online]. Available: https://link.aps.org/doi/10.1103/PhysRevB.80.113411

[76] I. Alber, W. Sigle, S. Müller, R. Neumann, O. Picht, M. Rauber, P. A. van Aken, and M. E. Toimil-Molares, "Visualization of Multipolar Longitudinal and Transversal Surface Plasmon Modes in Nanowire Dimers," *ACS Nano*, vol. 5, no. 12, pp. 9845–9853, Dec. 2011. [Online]. Available: https://doi.org/10.1021/nn2035044

[77] J. Grand, B. Auguié, and E. C. Le Ru, "Combined Extinction and Absorption UV–Visible Spectroscopy as a Method for Revealing Shape Imperfections of Metallic Nanoparticles," *Analytical Chemistry*, vol. 91, no. 22, pp. 14 639–14 648, Nov. 2019. [Online]. Available: https://doi.org/10.1021/acs.analchem.9b03798

[78] H. Guo, F. Ruan, L. Lu, J. Hu, J. Pan, Z. Yang, and B. Ren, "Correlating the Shape, Surface Plasmon Resonance, and Surface-Enhanced Raman Scattering of Gold Nanorods," *The Journal of Physical Chemistry C*, vol. 113, no. 24, pp. 10 459–10 464, Jun. 2009. [Online]. Available: https://doi.org/10.1021/jp9019427

[79] T. Tan, C. Tian, Z. Ren, J. Yang, Y. Chen, L. Sun, Z. Li, A. Wu, J. Yin, and H. Fu, "LSPR-dependent SERS performance of silver nanoplates with highly stable and broad tunable LSPRs prepared through an improved seed-mediated strategy," *Physical Chemistry Chemical Physics*, vol. 15, no. 48, pp. 21 034–21 042, Nov. 2013. [Online]. Available: https://pubs.rsc.org/en/content/articlelanding/2013/cp/c3cp52236a

[80] J. Zhao, J. A. Dieringer, X. Zhang, G. C. Schatz, and R. P. Van Duyne, "Wavelength-Scanned Surface-Enhanced Resonance Raman Excitation Spectroscopy," *The Journal of Physical Chemistry C*, vol. 112, no. 49, pp. 19 302–19 310, Dec. 2008. [Online]. Available: https://doi.org/10.1021/jp807837t

[81] C. L. Haynes and R. P. Van Duyne, "Plasmon-sampled surface-enhanced Raman excitation spectroscopy," *Journal of Physical Chemistry B*, vol. 107, no. 30, pp. 7426–7433, Jul. 2003. [Online]. Available: https://www.scopus.com/pages/publications/0041696760

[82] S. T. Sivapalan, B. M. DeVetter, T. K. Yang, T. van Dijk, and A. Et., "Off-Resonance Surface-Enhanced Raman Spectroscopy from Gold Nanorod Suspensions as a Function of Aspect Ratio: Not What We Thought," *ACS Nano*, 2013. [Online]. Available: https://sci-hub.st/10.1021/nn305710k

[83] G. Su, H. Jiang, H. Zhu, J.-J. Lv, G. Yang, B. Yan, and J.-J. Zhu, "Controlled deposition of palladium nanodendrites on the tips of gold nanorods and their enhanced catalytic activity," *Nanoscale*, vol. 9, no. 34, pp. 12 494–12 502, Aug. 2017. [Online]. Available: https://pubs.rsc.org/en/content/articlelanding/2017/nr/c7nr04046f

[84] R. X. He, R. Liang, P. Peng, and Y. Norman Zhou, "Effect of the size of silver nanoparticles on SERS signal enhancement," *Journal of Nanoparticle Research*, vol. 19, no. 8, p. 267, Jul. 2017. [Online]. Available: https://doi.org/10.1007/s11051-017-3953-0

[85] E. Magee, "The Properties and Applications of Silica-Coated Gold Nanoparticles," Nov. 2023. [Online]. Available: https://www.azonano.com/article.aspx?ArticleID=6624

[86] J. Ye, Z. Chen, W. Chen, Y. Zhao, C. Ding, and Y. Huang, "Gold Nanoparticles Coated with Silica Shells as High-Performance Fluorescence Nanoprobe," *ACS Applied Nano Materials*, vol. 7, no. 5, pp. 5543–5553, Mar. 2024. [Online]. Available: https://doi.org/10.1021/acsanm.4c00243

[87] B.-H. Jun, G. Kim, S. Jeong, M. S. Noh, X.-H. Pham, H. Kang, M.-H. Cho, J.-H. Kim, Y.-S. Lee, and D. H. Jeong, "Silica Core-based Surface-enhanced Raman Scattering (SERS) Tag: Advances in Multifunctional SERS Nanoprobes for Bioimaging and Targeting of Biomarkers#," *Bulletin of the Korean Chemical Society*, vol. 36, no. 3, pp. 963–978, 2015. [Online]. Available: https://onlinelibrary.wiley.com/doi/abs/10.1002/bkcs.10179

[88] M. M. Miller and A. A. Lazarides, "Sensitivity of Metal Nanoparticle Surface Plasmon Resonance to the Dielectric Environment," *The Journal of Physical Chemistry B*, vol. 109, no. 46, pp. 21 556–21 565, Nov. 2005. [Online]. Available: https://doi.org/10.1021/jp054227y

[89] M. A. Correa-Duarte, I. B. Becerril-Castro, and R. A. Alvarez-Puebla, "The Role of Porosity in SERS," *Advanced Optical Materials*,

vol. 13, no. 34, p. e01376, Dec. 2025. [Online]. Available: https://advanced.onlinelibrary.wiley.com/doi/10.1002/adom.202501376

[90] A. Uhlir Jr., "Electrolytic Shaping of Germanium and Silicon," *Bell System Technical Journal*, vol. 35, no. 2, pp. 333–347, 1956. [Online]. Available: https://onlinelibrary.wiley.com/doi/abs/10.1002/j.1538-7305.1956.tb02385.x

[91] L. T. Canham, "Silicon quantum wire array fabrication by electrochemical and chemical dissolution of wafers," *Applied Physics Letters*, vol. 57, no. 10, pp. 1046–1048, Sep. 1990. [Online]. Available: https://doi.org/10.1063/1.103561

[92] V. Lehmann and U. Gösele, "Porous silicon formation: A quantum wire effect," *Applied Physics Letters*, vol. 58, no. 8, pp. 856–858, Feb. 1991. [Online]. Available: https://doi.org/10.1063/1.104512

[93] G. Kittilsland, G. Stemme, and B. Nordén, "A sub-micron particle filter in silicon," *Sensors and Actuators A: Physical*, vol. 23, no. 1, pp. 904–907, Apr. 1990. [Online]. Available: https://www.sciencedirect.com/science/article/pii/092442479087056O

[94] D. L. Kendall, "A new theory for the anisotropic etching of silicon and some underdeveloped chemical micromachining concepts," *Journal of Vacuum Science & Technology A*, vol. 8, no. 4, pp. 3598–3605, Jul. 1990. [Online]. Available: https://doi.org/10.1116/1.576513

[95] A. Esmeraldo Paiva, M. S. Gerlt, N. F. Läubli, N. Prochukhan, J. F. Baez Vasquez, G. S. Kaminski Schierle, and M. A. Morris, "High Aspect Ratio Nanoscale Pores through BCP-Based Metal Oxide Masks and Advanced Dry Etching," *ACS Applied Materials & Interfaces*, vol. 15, no. 50, pp. 57 960–57 969, Dec. 2023. [Online]. Available: https://doi.org/10.1021/acsami.3c09863

[96] L. Canham, Ed., *Handbook of Porous Silicon*. Cham: Springer International Publishing, 2018. [Online]. Available: https://link.springer.com/10.1007/978-3-319-71381-6

[97] Z. Huang, N. Geyer, P. Werner, J. de Boor, and U. Gösele, "Metal-Assisted Chemical Etching of Silicon: A Review," *Advanced Materials*, vol. 23, no. 2, pp. 285–308, 2011. [Online]. Available: https://onlinelibrary.wiley.com/doi/abs/10.1002/adma.201001784

[98] M. J. Sailor, "Porous Silicon in Practice," 2011.

[99] S. Dhanekar and S. Jain, "Porous silicon biosensor: Current status," *Biosensors and Bioelectronics*, vol. 41, pp. 54–64, Mar. 2013. [Online]. Available: https://www.sciencedirect.com/science/article/pii/S0956566312006513

[100] J. Rouquerol, D. Avnir, C. W. Fairbridge, D. H. Everett, J. M. Haynes, N. Pernicone, J. D. F. Ramsay, K. S. W. Sing, and K. K. Unger, "Recommendations for the characterization of porous solids (Technical Report)," *Pure and Applied Chemistry*, vol. 66, no. 8, pp. 1739–1758, 1994. [Online]. Available: https://doi.org/10.1351/pac199466081739

[101] X. G. Zhang, "Morphology and Formation Mechanisms of Porous Silicon," *Journal of The Electrochemical Society*, vol. 151, no. 1, p. C69, Dec. 2003. [Online]. Available: https://iopscience.iop.org/article/10.1149/1.1632477

[102] A. Janshoff, K.-P. S. Dancil, C. Steinem, D. P. Greiner, V. S.-Y. Lin, C. Gurtner, K. Motesharei, M. J. Sailor, and M. R. Ghadiri, "Macroporous p-Type Silicon FabryPerot Layers. Fabrication, Characterization, and Applications in Biosensing," *Journal of the American Chemical Society*, vol. 120, no. 46, pp. 12 108–12 116, Nov. 1998. [Online]. Available: https://doi.org/10.1021/ja9826237

[103] M. M. Orosco, C. Pacholski, and M. J. Sailor, "Real-time monitoring of enzyme activity in a mesoporous silicon double layer," *Nature Nanotechnology*, vol. 4, no. 4, pp. 255–258, Apr. 2009. [Online]. Available: https://www.nature.com/articles/nnano.2009.11

[104] M. B. Gongalsky, A. A. Koval, S. N. Schevchenko, K. P. Tamarov, and L. A. Osminkina, "Double Etched Porous Silicon Films for Improved Optical Sensing of Bacteria," *Journal of The Electrochemical Society*, vol. 164, no. 12, p. B581, Sep. 2017. [Online]. Available: https://iopscience.iop.org/article/10.1149/2.1821712jes

[105] R. T. Elafandy, J.-H. Kang, C. Mi, T. K. Kim, J. S. Kwak, and J. Han, "Study and Application of Birefringent Nanoporous GaN in the Polarization Control of Blue Vertical-Cavity Surface-Emitting Lasers," *ACS Photonics*, vol. 8, no. 4, pp. 1041–1047, Apr. 2021. [Online]. Available: https://doi.org/10.1021/acsphotonics.1c00211

[106] Y. Watanabe, Y. Arita, T. Yokoyama, and Y. Igarashi, "Formation and Properties of Porous Silicon and Its Application," *Journal of The Electrochemical Society*, vol. 122, Oct. 1975. [Online]. Available: https://oamonitor.ireland.openaire.eu/national//search/publication?pid=10.1149%2F1.2134015

[107] T. UNAGAMI, "Formation mechanism of porous silicon layer by anodization in HF solution," 1980.

[108] X. G. Zhang, "Mechanism of Pore Formation on n-Type Silicon," *Journal of The Electrochemical Society*, vol. 138, no. 12, p. 3750, Dec. 1991. [Online]. Available: https://doi.org/10.1149/1.2085494

[109] S. Mariani, L. Pino, L. M. Strambini, L. Tedeschi, and G. Barillaro, "10 000-Fold Improvement in Protein Detection Using Nanostructured Porous Silicon Interferometric Aptasensors," *ACS Sensors*, vol. 1, no. 12, pp. 1471–1479, Dec. 2016. [Online]. Available: https://doi.org/10.1021/acssensors.6b00634

[110] E. Pinna, M. Mehrabanian, E. Redolfi Riva, E. Cara, G. Aprile, L. Boarino, and G. Mula, "Electrochemical Nanolithography on Silicon: An Easy and Scalable Method to Control Pore Formation at the Nanoscale," *Materials*, vol. 12, no. 18, 2019. [Online]. Available: https://www.mdpi.com/1996-1944/12/18/2891

[111] H. Looyenga, "Dielectric constants of heterogeneous mixtures," *Physica*, vol. 31, no. 3, pp. 401–406, Mar. 1965. [Online]. Available: https://www.sciencedirect.com/science/article/pii/0031891465900455

[112] D. A. G. Bruggeman, "Berechnung verschiedener physikalischer Konstanten von heterogenen Substanzen. I. Dielektrizitätskonstanten und Leitfähigkeiten der Mischkörper aus isotropen Substanzen," *Annalen der Physik*, vol. 416, no. 7, pp. 636–664, Jan. 1935. [Online]. Available: https://onlinelibrary.wiley.com/doi/10.1002/andp.19354160705

[113] A. M. Ruminski, G. Barillaro, C. Chaffin, and M. J. Sailor, "Internally Referenced Remote Sensors for HF and Cl2 Using Reactive Porous Silicon Photonic Crystals," *Advanced Functional Materials*, vol. 21, no. 8, pp. 1511–1525, 2011. [Online]. Available: https://onlinelibrary.wiley.com/doi/abs/10.1002/adfm.201002037

[114] W. Theiss, *SCOUT 3: Optical Spectrum Simulation — Technical Manual*, W. Theiss Hard- and Software for Optical Spectroscopy, Aachen, Germany, 2012. [Online]. Available: https://www.wtheiss.com/download/scout3.pdf

[115] E. Astrova and V. Tolmachev, "Effective refractive index and composition of oxidized porous silicon films," *Materials Science and Engineering: B*, vol. 69-70, pp. 142–148, Jan. 2000. [Online]. Available: https://linkinghub.elsevier.com/retrieve/pii/S0921510799002366

[116] G. Lérondel, R. Romestain, and S. Barret, "Roughness of the porous silicon dissolution interface," *Journal of Applied Physics*, vol. 81, no. 9, pp. 6171–6178, May 1997. [Online]. Available: https://doi.org/10.1063/1.364400

[117] M. Karim, R. Martini, H. S. Radhakrishnan, K. van Nieuwenhuysen, V. Depauw, W. Ramadan, I. Gordon, and J. Poortmans, "Tuning of strain and surface roughness of porous silicon layers for higher-quality seeds for epitaxial growth," *Nanoscale Research Letters*, vol. 9, no. 1, p. 348, 2014.

[118] C. Guo, M. Kong, W. Gao, and B. Li, "Simultaneous determination of optical constants, thickness, and surface roughness of thin film from spectrophotometric measurements," *Optics Letters*, vol. 38, no. 1, pp. 40–42, Jan. 2013. [Online]. Available: https://opg.optica.org/ol/abstract.cfm?uri=ol-38-1-40

[119] C. F. Ramirez-Gutierrez, J. D. Castaño-Yepes, and M. E. Rodriguez-Garcia, "Porosity and roughness determination of porous silicon thin films by genetic algorithms," *Optik*, vol. 173, pp. 271–278, Nov. 2018. [Online]. Available: https://www.sciencedirect.com/science/article/pii/S0030402618311380

[120] R. Vercauteren, G. Scheen, J.-P. Raskin, and L. A. Francis, "Porous silicon membranes and their applications: Recent advances," *Sensors and Actuators A: Physical*, vol. 318, p. 112486, Feb. 2021. [Online]. Available: https://www.sciencedirect.com/science/article/pii/S092442472031801X

[121] B. Bardet, S. Desplobain, J. Billoué, L. Ventura, and G. Gautier, "Integration of low-loss inductors on thin porous silicon membranes," *Microelectronic Engineering*, vol. 194, pp. 96–99, Jul. 2018. [Online].

Available: https://linkinghub.elsevier.com/retrieve/pii/S0167931718301321

[122] J. Ji, S. Park, H. Do, and H. S. Kum, "A review on recent advances in fabricating freestanding single-crystalline complex-oxide membranes and its applications," *Physica Scripta*, vol. 98, no. 5, p. 052002, May 2023. [Online]. Available: https://iopscience.iop.org/article/10.1088/1402-4896/acccb4

[123] R. Mentek, D. Hippo, B. Gelloz, and N. Koshida, "Photovoltaic effect with high open circuit voltage observed in electrochemically prepared nanocrystalline silicon membranes," *Materials Science and Engineering: B*, vol. 190, pp. 33–40, Dec. 2014. [Online]. Available: https://linkinghub.elsevier.com/retrieve/pii/S0921510714001937

[124] M. Corsi, A. Paghi, S. Mariani, G. Golinelli, A. Debrassi, G. Egri, G. Leo, E. Vandini, A. Vilella, L. Dähne, D. Giuliani, and G. Barillaro, "Bioresorbable Nanostructured Chemical Sensor for Monitoring of pH Level In Vivo," *Advanced Science*, vol. 9, no. 22, p. 2202062, Aug. 2022. [Online]. Available: https://onlinelibrary.wiley.com/doi/10.1002/advs.202202062

[125] C. S. Solanki, R. R. Bilyalov, J. Poortmans, J.-P. Celis, J. Nijs, and R. Mertens, "Self-Standing Porous Silicon Films by One-Step Anodizing," *Journal of The Electrochemical Society*, vol. 151, no. 5, p. C307, 2004. [Online]. Available: https://iopscience.iop.org/article/10.1149/1.1688797

[126] I.-T. Chen, D. A. Sessoms, Z. Sherman, E. Choi, O. Vincent, and A. D. Stroock, "Stability Limit of Water by Metastable Vapor–Liquid Equilibrium with Nanoporous Silicon Membranes," *The Journal of Physical Chemistry B*, vol. 120, no. 23, pp. 5209–5222, Jun. 2016. [Online]. Available: https://pubs.acs.org/doi/10.1021/acs.jpcb.6b01618

[127] D. N. Goryachev, L. V. Belyakov, and O. M. Sreseli, "Free-standing luminescent layers of porous silicon," *Semiconductors*, vol. 44, no. 12, pp. 1588–1591, Dec. 2010. [Online]. Available: http://link.springer.com/10.1134/S1063782610120092

[128] M. Thakur, R. B. Pernites, N. Nitta, M. Isaacson, S. L. Sinsabaugh, M. S. Wong, and S. L. Biswal, "Freestanding Macroporous Silicon and Pyrolyzed Polyacrylonitrile As a Composite Anode for Lithium Ion

Batteries," *Chemistry of Materials*, vol. 24, no. 15, pp. 2998–3003, Aug. 2012. [Online]. Available: https://pubs.acs.org/doi/10.1021/cm301376t

[129] H. Ning, N. A. Krueger, X. Sheng, H. Keum, C. Zhang, K. D. Choquette, X. Li, S. Kim, J. A. Rogers, and P. V. Braun, "Transfer-Printing of Tunable Porous Silicon Microcavities with Embedded Emitters," *ACS Photonics*, vol. 1, no. 11, pp. 1144–1150, Nov. 2014. [Online]. Available: https://pubs.acs.org/doi/10.1021/ph500230j

[130] A. Chiadò, C. Novara, A. Lamberti, F. Geobaldo, F. Giorgis, and P. Rivolo, "Immobilization of Oligonucleotides on Metal-Dielectric Nanostructures for miRNA Detection," *Analytical Chemistry*, vol. 88, no. 19, pp. 9554–9563, Oct. 2016. [Online]. Available: https://pubs.acs.org/doi/10.1021/acs.analchem.6b02186

[131] C. Novara, A. Lamberti, A. Chiadò, A. Virga, P. Rivolo, F. Geobaldo, and F. Giorgis, "Surface-enhanced Raman spectroscopy on porous silicon membranes decorated with Ag nanoparticles integrated in elastomeric microfluidic chips," *RSC Advances*, vol. 6, no. 26, pp. 21 865–21 870, Feb. 2016. [Online]. Available: https://pubs.rsc.org/en/content/articlelanding/2016/ra/c5ra26746c

[132] C. Novara, A. Chiadò, N. Paccotti, S. Catuogno, C. L. Esposito, G. Condorelli, V. De Franciscis, F. Geobaldo, P. Rivolo, and F. Giorgis, "SERS-active metal-dielectric nanostructures integrated in microfluidic devices for label-free quantitative detection of miRNA," *Faraday Discussions*, vol. 205, pp. 271–289, 2017. [Online]. Available: https://xlink.rsc.org/?DOI=C7FD00140A

[133] D. Martin-Sanchez, S. Ponce-Alcantara, and J. Garcia-Ruperez, "Sensitivity Comparison of a Self-Standing Porous Silicon Membrane Under Flow-Through and Flow-Over Conditions," *IEEE Sensors Journal*, vol. 19, no. 9, pp. 3276–3281, May 2019. [Online]. Available: https://ieeexplore.ieee.org/document/8620315/

[134] Y. Wan, N. A. Krueger, C. R. Ocier, P. Su, P. V. Braun, and B. T. Cunningham, "Resonant Mode Engineering of Photonic Crystal Sensors Clad with Ultralow Refractive Index Porous Silicon Dioxide," *Advanced Optical Materials*, vol. 5, no. 21, p. 1700605, Nov. 2017. [Online]. Available: https://onlinelibrary.wiley.com/doi/10.1002/adom.201700605

[135] Y. Zhao, G. Gaur, S. T. Retterer, P. E. Laibinis, and S. M. Weiss, "Flow-Through Porous Silicon Membranes for Real-Time Label-Free Biosensing," *Analytical Chemistry*, vol. 88, no. 22, pp. 10 940–10 948, Nov. 2016. [Online]. Available: https://pubs.acs.org/doi/10.1021/acs.analchem.6b02521

[136] S. O. Meade and M. J. Sailor, "Microfabrication of freestanding porous silicon particles containing spectral barcodes," *physica status solidi (RRL) – Rapid Research Letters*, vol. 1, no. 2, Mar. 2007. [Online]. Available: https://onlinelibrary.wiley.com/doi/10.1002/pssr.200600077

[137] B. Terheiden, J. Hensen, A. Wolf, R. Horbelt, H. Plagwitz, and R. Brendel, "Layer Transfer from Chemically Etched 150 mm Porous Si Substrates," *Materials*, vol. 4, no. 5, pp. 941–951, May 2011. [Online]. Available: https://www.mdpi.com/1996-1944/4/5/941

[138] D. J. Jubgang Fandio, S. Sauze, A. Boucherif, R. Arès, and D. Morris, "Structural, optical and terahertz properties of graphene-mesoporous silicon nanocomposites," *Nanoscale Advances*, vol. 2, no. 1, pp. 340–346, 2020. [Online]. Available: https://xlink.rsc.org/?DOI=C9NA00502A

[139] R. Liu, T. A. Schmedake, Y. Y. Li, M. J. Sailor, and Y. Fainman, "Novel porous silicon vapor sensor based on polarization interferometry," *Sensors and Actuators B: Chemical*, vol. 87, no. 1, pp. 58–62, Nov. 2002. [Online]. Available: https://linkinghub.elsevier.com/retrieve/pii/S0925400502002174

[140] S. De La Luz-Merino, M. E. Calixto, and A. Méndez-Blas, "Nanostructured CuInSe2 by electrodeposition with the assistance of porous silicon templates," *Materials Chemistry and Physics*, vol. 163, pp. 362–368, Aug. 2015. [Online]. Available: https://linkinghub.elsevier.com/retrieve/pii/S0254058415302443

[141] L. Velleman, C. J. Shearer, A. V. Ellis, D. Losic, N. H. Voelcker, and J. G. Shapter, "Fabrication of self-supporting porous silicon membranes and tuning transport properties by surface functionalization," *Nanoscale*, vol. 2, no. 9, p. 1756, 2010. [Online]. Available: https://xlink.rsc.org/?DOI=c0nr00284d

[142] Y. Jin, Y. Yang, W. Duan, X. Qu, and J. Wu, "Synergistic and On-Demand Release of Ag-AMPs Loaded on Porous Silicon Nanocarriers

for Antibacteria and Wound Healing," *ACS Applied Materials & Interfaces*, vol. 13, no. 14, pp. 16 127–16 141, Apr. 2021. [Online]. Available: https://pubs.acs.org/doi/10.1021/acsami.1c02161

[143] Y. Bu, G. Zhu, S. Li, R. Qi, G. Bhave, D. Zhang, R. Han, D. Sun, X. Liu, Z. Hu, and X. Liu, "Silver-Nanoparticle-Embedded Porous Silicon Disks Enabled SERS Signal Amplification for Selective Glutathione Detection," *ACS Applied Nano Materials*, vol. 1, no. 1, pp. 410–417, Jan. 2018. [Online]. Available: https://pubs.acs.org/doi/10.1021/acsanm.7b00290

[144] L. G. Cencha, C. Antonio Hernández, L. Forzani, R. Urteaga, and R. R. Koropecki, "Optical performance of hybrid porous silicon–porous alumina multilayers," *Journal of Applied Physics*, vol. 123, no. 18, p. 183101, May 2018. [Online]. Available: https://pubs.aip.org/jap/article/123/18/183101/154903/Optical-performance-of-hybrid-porous-silicon

[145] Y. Pei, S. H. Shahoei, Y. Li, P. J. Reece, E. R. Nelson, J. J. Gooding, and K. A. Kilian, "Vertical Integration of Cell-Laden Hydrogels with Bioinspired Photonic Crystal Membranes," *Advanced Materials Interfaces*, vol. 5, no. 23, p. 1801233, Dec. 2018. [Online]. Available: https://advanced.onlinelibrary.wiley.com/doi/10.1002/admi.201801233

[146] V. S. Vendamani, R. Beeram, S. V. S. Nageswara Rao, A. P. Pathak, and V. R. Soma, "Trace level detection of explosives and pesticides using robust, low-cost, free-standing silver nanoparticles decorated porous silicon," *Optics Express*, vol. 29, no. 19, p. 30045, Sep. 2021. [Online]. Available: https://opg.optica.org/abstract.cfm?URI=oe-29-19-30045

[147] A. Ivanov, U. Mescheder, and P. Woias, "Finite-Elements Simulation of Etch Front Propagation in Silicon Electropolishing Process," *ECS Transactions*, vol. 58, no. 46, pp. 15–24, Apr. 2014. [Online]. Available: https://iopscience.iop.org/article/10.1149/05846.0015ecst

[148] A. Ivanov, *Silicon Anodization as a Structuring Technique*. Wiesbaden: Springer Fachmedien Wiesbaden, 2018. [Online]. Available: http://link.springer.com/10.1007/978-3-658-19238-9

[149] G. V. Li, E. V. Astrova, N. E. Preobrazhenskii, A. M. Rumyantsev, S. I. Pavlov, and E. V. Beregulin, "Negative Electrodes for Lithium-Ion

Batteries Obtained by Photoanodization of Solar-Grade Silicon," *Technical Physics*, vol. 64, no. 5, pp. 660–665, May 2019. [Online]. Available: http://link.springer.com/10.1134/S1063784219050141

[150] V. Lysenko, J. Vitiello, B. Remaki, and D. Barbier, "Gas permeability of porous silicon nanostructures," *Physical Review E*, vol. 70, no. 1, p. 017301, Jul. 2004. [Online]. Available: https://link.aps.org/doi/10.1103/PhysRevE.70.017301

[151] J. Liu, Y. Yu, X. Yang, R. Chen, C. Luan, F. Jiang, and H. Xiao, "Preparation of large-area, high quality, free-standing GaN distributed Bragg reflectors," *Materials Letters*, vol. 311, p. 131621, Mar. 2022. [Online]. Available: https://linkinghub.elsevier.com/retrieve/pii/S0167577X2102320X

[152] P. Dardano, A. Caliò, J. Politi, I. Rea, I. Rendina, and L. De Stefano, "Optically monitored drug delivery patch based on porous silicon and polymer microneedles," *Biomedical Optics Express*, vol. 7, no. 5, p. 1645, May 2016. [Online]. Available: https://opg.optica.org/abstract.cfm?URI=boe-7-5-1645

[153] M. Ghulinyan, C. J. Oton, G. Bonetti, Z. Gaburro, and L. Pavesi, "Free-standing porous silicon single and multiple optical cavities," *Journal of Applied Physics*, vol. 93, no. 12, pp. 9724–9729, Jun. 2003. [Online]. Available: https://pubs.aip.org/jap/article/93/12/9724/484087/Free-standing-porous-silicon-single-and-multiple

[154] N. Kumar, E. Froner, R. Guider, M. Scarpa, and P. Bettotti, "Investigation of non-specific signals in nanoporous flow-through and flow-over based sensors," *The Analyst*, vol. 139, no. 6, p. 1345, 2014. [Online]. Available: https://xlink.rsc.org/?DOI=c3an01996a

[155] V. Castillo-Gallardo, L. E. Puente-Díaz, W. L. Mochán Backal, and V. Agarwal, "Porous silica based controllable reversible freestanding Bragg structures: From omnidirectional mirrors to transparency," *Ceramics International*, vol. 51, no. 3, pp. 3170–3175, Jan. 2025. [Online]. Available: https://linkinghub.elsevier.com/retrieve/pii/S0272884224053902

[156] H. Li, X. Yue, R. Gao, W. Peng, X.-M. Guo, H. Cheng, H. Jiang, F. Zhong, J.-S. Lin, J. Tang, Y.-J. Zhang, and J.-F. Li, "Gold Nanoparticles/Porous Silicon Photonic Crystal with

Tunable Bandgap for Wavelength-Matching, Ultrasensitive, and Background-Free Surface-Enhanced Raman Scattering Bioanalysis," *ACS Nano*, vol. 20, no. 3, pp. 3008–3018, Jan. 2026. [Online]. Available: https://pubs.acs.org/doi/10.1021/acsnano.5c19208

[157] S.-Y. Huang, H.-H. Hsu, A. Muhammed Musthafa, I.-A. Lin, C.-M. Chou, and V. K. S. Hsiao, "Tuning Multi-Wavelength Reflection Properties of Porous Silicon Bragg Reflectors Using Silver-Nanoparticle-Assisted Electrochemical Etching," *Micromachines*, vol. 16, no. 11, p. 1198, Oct. 2025. [Online]. Available: https://www.mdpi.com/2072-666X/16/11/1198

[158] L.-Y. Liang, Y.-H. Kung, V. K. S. Hsiao, and C.-C. Chu, "Reduction of Nitroaromatics by Gold Nanoparticles on Porous Silicon Fabricated Using Metal-Assisted Chemical Etching," *Nanomaterials*, vol. 13, no. 11, p. 1805, Jun. 2023. [Online]. Available: https://www.mdpi.com/2079-4991/13/11/1805

[159] M. De La Mora, J. Bornacelli, R. Nava, R. Zanella, and J. Reyes-Esqueda, "Porous silicon photoluminescence modification by colloidal gold nanoparticles: Plasmonic, surface and porosity roles," *Journal of Luminescence*, vol. 146, pp. 247–255, Feb. 2014. [Online]. Available: https://linkinghub.elsevier.com/retrieve/pii/S0022231313006170

[160] D. Ge, Z. Fang, C. Zhao, J. Shi, and L. Zhang, "Preparation and anti-reflection performance of porous silicon/gold nanocomposite structures," *The European Physical Journal D*, vol. 77, no. 6, p. 108, Jun. 2023. [Online]. Available: https://link.springer.com/10.1140/epjd/s10053-023-00674-w

[161] M. Khalifa, M. Jaduaa, and A. Abd, "Quantum dots gold nanoparticle /porous silicon/silicon for solar cell applications," *Journal of Nanostructures*, vol. 10, no. 4, Oct. 2020. [Online]. Available: https://doi.org/10.22052/JNS.2020.04.019

[162] A. Ciemięga, K. Maresz, M. Romaszewski, P. Głomb, P. Krupska-Wolas, and K. Prusik, "Hyperspectral Imaging as a Facile and Non-Destructive Method for Size Analysis of Gold Nanoparticles Deposited on Porous Materials," *Particle & Particle Systems Characterization*, vol. 41, no. 2, p. 2200204, 2024. [Online]. Available: https://onlinelibrary.wiley.com/doi/abs/10.1002/ppsc.202200204

[163] A. B. Dheyab, A. M. Alwan, and M. Q. Zayer, "Optimizing of Gold Nanoparticles on Porous Silicon Morphologies for a Sensitive Carbon Monoxide Gas Sensor Device," *Plasmonics*, vol. 14, no. 2, pp. 501–509, Apr. 2019. [Online]. Available: http://link.springer.com/10.1007/s11468-018-0828-x

[164] R. Ramadan and R. J. Martín-Palma, "The Infiltration of Silver Nanoparticles into Porous Silicon for Improving the Performance of Photonic Devices," *Nanomaterials*, vol. 12, no. 2, p. 271, Jan. 2022. [Online]. Available: https://www.mdpi.com/2079-4991/12/2/271

[165] A. M. Hmmoodi, U. M. Nayef, and M. Rasheed, "Nano-gold via laser ablation in liquid at different laser energies on porous silicon for photodetector application," *Journal of Optics*, May 2024. [Online]. Available: https://link.springer.com/10.1007/s12596-024-01844-8

[166] F. Severiano, V. L. Gayou, G. García, J. A. Luna-López, H. M. Gutiérrez, J. A. A. Adame, and M. Rojas-López, "Morphological and Optical Characterization of Gold Nanoparticles Decorated Porous Silicon," *Journal of Nanoscience and Nanotechnology*, vol. 19, no. 6, pp. 3604–3609, Jun. 2019. [Online]. Available: https://www.ingentaconnect.com/content/10.1166/jnn.2019.16094

[167] A. M. Alwan and I. A. Naseef, "Optimization of photoluminescence properties of Porous silicon by adding gold nanoparticles," *Iraqi Journal of Science*, vol. 58, 2017.

[168] S. Escobar, R. Nava, and J. A. Reyes-Esqueda, "Plasmonic-enhanced photoluminescence in porous silicon with pore- embedded gold nanoparticles fabricated by direct reduction of chloroauric acid."

[169] E. M. Lee, J. Lee, Y. Kim, K. S. Yi, J. Cho, J. Kim, J. M. An, D. Lee, S. J. Kim, E. An, Y. J. Hong, H. Jo, S. H. Lee, Y. Jung, C.-H. Choi, J. S. Kang, J. Hur, and D. Kim, "Hybrid Composite of Silver Nanoparticle–Porous Silicon Microparticles as an Image-Guided Localization Agent for Computed Tomography Scan of the Lungs," *ACS Biomaterials Science & Engineering*, vol. 6, no. 8, pp. 4390–4396, Aug. 2020. [Online]. Available: https://pubs.acs.org/doi/10.1021/acsbiomaterials.0c00611

[170] Y. Jiao, D. S. Koktysh, N. Phambu, and S. M. Weiss, "Dual-mode sensing platform based on colloidal gold functionalized porous

silicon," *Applied Physics Letters*, vol. 97, no. 15, p. 153125, Oct. 2010. [Online]. Available: https://doi.org/10.1063/1.3503608

[171] H. V. Bandarenka, K. V. Girel, S. A. Zavatski, A. Panarin, and S. N. Terekhov, "Progress in the Development of SERS-Active Substrates Based on Metal-Coated Porous Silicon," *Materials*, vol. 11, no. 5, p. 852, May 2018. [Online]. Available: https://www.mdpi.com/1996-1944/11/5/852

[172] Chan, Selena, Berlin, Andrew A., and Yamakawa, Mineo, "Metal coated nanocrystalline silicon as an active surface enhanced Raman spectroscopy (SERS) substrate," U.S. Patent US6 970 239 B2, Nov., 2005.

[173] L. Zeiri, K. Rechav, Z. Porat, and Y. Zeiri, "Silver Nanoparticles Deposited on Porous Silicon as a Surface-Enhanced Raman Scattering (SERS) Active Substrate," *Applied Spectroscopy*, vol. 66, no. 3, pp. 294–299, Mar. 2012. [Online]. Available: https://journals.sagepub.com/doi/10.1366/11-06476

[174] N. F. Ismail, K. Y. Lee, N. S. Mohd Hadis, L. N. Ismail, A. F. Abdul Rahim, M. H. Abdullah, and A. R. M. Radzol, "Nano Silver-Coated Porous Silicon-Based Surface-Enhanced Raman Spectroscopy Substrate for Low-Concentration Dengue NS1 Protein Detection," *Journal of Applied Spectroscopy*, vol. 91, no. 2, pp. 480–488, May 2024. [Online]. Available: https://link.springer.com/10.1007/s10812-024-01744-6

[175] V.-T. Vo, Y. Gwon, V.-D. Phung, Y.-D. Son, J.-H. Kim, and S.-W. Lee, "Ag-Deposited Porous Silicon as a SERS-Active Substrate for the Sensitive Detection of Catecholamine Neurotransmitters," *Electronic Materials Letters*, vol. 17, no. 3, pp. 292–298, May 2021. [Online]. Available: https://doi.org/10.1007/s13391-021-00281-0

[176] X. Ma, H. Cheng, J. Hou, Z. Jia, G. Wu, X. Lü, H. Li, X. Zheng, and C. Chen, "Detection of breast cancer based on novel porous silicon Bragg reflector surface-enhanced Raman spectroscopy-active structure," *Chinese Optics Letters*, vol. 18, no. 5, p. 051701, 2020. [Online]. Available: https://www.researching.cn/ArticlePdf/m00005/2020/18/5/051701.pdf

[177] H. Li, Q. Wang, N. Gao, J. Fu, X. Yue, X. Lv, F. Zhong, J. Tang, and T. Wang, "Facile synthesis of magnetic ionic liquids/gold nanoparticles/porous silicon composite SERS substrate for ultra-sensitive detection of arsenic," *Applied Surface Science*, vol. 545, p. 148992, Apr. 2021. [Online]. Available: https://linkinghub.elsevier.com/retrieve/pii/S0169433221000684

[178] M. Škrabić, M. Krajačić, M. Gotić, N. Baran, L. Mikac, T. Jurkin, N. Šegedin, M. Ivanda, and O. Gamulin, "Gold-coated porous silicon as a SERS substrate for near-infrared excitation: Off- and on-resonant conditions," *Applied Surface Science*, vol. 644, p. 158820, Jan. 2024. [Online]. Available: https://linkinghub.elsevier.com/retrieve/pii/S016943322302500X

[179] S. Mariani, A. Paghi, A. A. La Mattina, A. Debrassi, L. Dähne, and G. Barillaro, "Decoration of Porous Silicon with Gold Nanoparticles via Layer-by-Layer Nanoassembly for Interferometric and Hybrid Photonic/Plasmonic (Bio)sensing," *ACS Applied Materials & Interfaces*, vol. 11, no. 46, pp. 43 731–43 740, Nov. 2019. [Online]. Available: https://doi.org/10.1021/acsami.9b15737

[180] M. A. Rashed, F. A. Harraz, M. Faisal, A. M. El-Toni, M. Alsaiari, and M. Al-Assiri, "Gold nanoparticles plated porous silicon nanopowder for nonenzymatic voltammetric detection of hydrogen peroxide," *Analytical Biochemistry*, vol. 615, p. 114065, Feb. 2021. [Online]. Available: https://linkinghub.elsevier.com/retrieve/pii/S0003269720305972

[181] M. H. Jasim, U. M. Nayef, and H. T. Hussien, "Study of Spectral Responsivity of Au@In2O3 Nanoparticles via Laser Ablation Deposited on Porous Silicon," *Plasmonics*, vol. 19, no. 2, pp. 933–941, Apr. 2024. [Online]. Available: https://link.springer.com/10.1007/s11468-023-02041-2

[182] J. Peng, Y. Song, Y. Lin, and Z. Huang, "Introduction and Development of Surface-Enhanced Raman Scattering (SERS) Substrates: A Review," *Nanomaterials*, vol. 14, no. 20, p. 1648, Oct. 2024.

[183] M. Y. Tsvetkov, B. N. Khlebtsov, V. A. Khanadeev, V. N. Bagratashvili, P. S. Timashev, M. I. Samoylovich, and N. G. Khlebtsov, "SERS substrates formed by gold nanorods deposited on colloidal silica

films," *Nanoscale Research Letters*, vol. 8, no. 1, p. 250, May 2013. [Online]. Available: https://doi.org/10.1186/1556-276X-8-250

[184] K. Srivastava, H. Le-The, J. J. A. Lozeman, A. van den Berg, W. van der Stam, and M. Odijk, "Prospects of nano-lithographic tools for the fabrication of surface-enhanced Raman spectroscopy (SERS) substrates," *Micro and Nano Engineering*, vol. 23, p. 100267, Jun. 2024. [Online]. Available: https://www.sciencedirect.com/science/article/pii/S2590007224000303

[185] G. M. Das, S. Managò, M. Mangini, and A. C. De Luca, "Biosensing Using SERS Active Gold Nanostructures," *Nanomaterials*, vol. 11, no. 10, p. 2679, Oct. 2021. [Online]. Available: https://www.mdpi.com/2079-4991/11/10/2679

[186] C. Kim, S. Baek, Y. Ryu, Y. Kim, D. Shin, C.-W. Lee, W. Park, A. M. Urbas, G. Kang, and K. Kim, "Large-scale nanoporous metal-coated silica aerogels for high SERS effect improvement," *Scientific Reports*, vol. 8, no. 1, p. 15144, Oct. 2018. [Online]. Available: https://www.nature.com/articles/s41598-018-33539-z

[187] S. N. Erkızan, F. Idikut, O. Demirtas, A. Goodarzi, A. K. Demir, M. Borra, I. Pavlov, and A. Bek, "LIPSS for SERS: Metal Coated Direct Laser Written Periodic Nanostructures for Surface Enhanced Raman Spectroscopy," *Advanced Optical Materials*, vol. 10, no. 22, p. 2200233, 2022. [Online]. Available: https://onlinelibrary.wiley.com/doi/abs/10.1002/adom.202200233

[188] W. Wang, W. Mao, H. Sun, F. Hou, W. Wang, W. Liu, Z. Shi, G. Lin, M. Wang, G. Fang, Y. Y. Cheng, and C. Xu, "Microfluidic SERS biosensor based on Au-semicoated photonic crystals for melanoma diagnosis," *Biosensors and Bioelectronics*, vol. 271, p. 116983, Mar. 2025. [Online]. Available: https://linkinghub.elsevier.com/retrieve/pii/S0956566324009904

[189] X. Zhao, C. Chen, J. Hou, Z. Jia, C. Chen, and X. Lv, "Graphitic carbon @ silver nanoparticle @ porous silicon Bragg mirror composite SERS substrate for gallic acid detection," *Spectrochimica Acta Part A: Molecular and Biomolecular Spectroscopy*, vol. 323, p. 124861, Dec. 2024. [Online]. Available: https://linkinghub.elsevier.com/retrieve/pii/S1386142524010278

[190] W. Li, S. Dai, X. Li, Q. Li, and J. Li, "Highly sensitive SERS detection of melamine based on 3D Ag@porous silicon photonic crystal," *Talanta*, vol. 280, p. 126789, Dec. 2024. [Online]. Available: https://linkinghub.elsevier.com/retrieve/pii/S0039914024011688

[191] S. Han, C. Chen, C. Chen, L. Wu, X. Wu, C. Lu, X. Zhang, P. Chao, X. Lv, Z. Jia, and J. Hou, "Coupling annealed silver nanoparticles with a porous silicon Bragg mirror SERS substrate and machine learning for rapid non-invasive disease diagnosis," *Analytica Chimica Acta*, vol. 1254, p. 341116, May 2023. [Online]. Available: https://linkinghub.elsevier.com/retrieve/pii/S0003267023003379

[192] G. Chen, K. Zhang, B. Luo, W. Hong, J. Chen, and X. Chen, "Plasmonic-3D photonic crystals microchip for surface enhanced Raman spectroscopy," *Biosensors and Bioelectronics*, vol. 143, p. 111596, Oct. 2019. [Online]. Available: https://linkinghub.elsevier.com/retrieve/pii/S095656631930675X

[193] M. Lv, X. Wu, W. Wang, D. Han, S. Chen, Y. Hu, Q. Zhang, Q. Wang, and R. Wei, "Single-Molecule Detection via Pore Nanoconfinement of Covalent Organic Frameworks for Surface-Enhanced Raman Scattering," *ACS Sensors*, vol. 10, no. 3, pp. 1778–1787, Mar. 2025. [Online]. Available: https://doi.org/10.1021/acssensors.4c02391

[194] C.-A. Ku, C.-H. Chiu, C.-Y. Yu, C.-Y. Yang, and C.-K. Chung, "A High-Regularity Porous SERS Substrate Prepared by Two-Step Mild and Hard Anodization for Sorbic Acid Detection," *Sensors*, vol. 26, no. 1, p. 156, Jan. 2026. [Online]. Available: https://www.mdpi.com/1424-8220/26/1/156

[195] G. Lu, G. Wang, and H. Li, "Effect of nanostructured silicon on surface enhanced Raman scattering," *RSC Advances*, vol. 8, no. 12, pp. 6629–6633, Feb. 2018. [Online]. Available: https://pubs.rsc.org/en/content/articlelanding/2018/ra/c8ra00014j

[196] "Scatterer on Substrate." [Online]. Available: https://www.comsol.com/model/scatterer-on-substrate-14699

[197] G. Vuye, S. Fisson, V. Nguyen Van, Y. Wang, J. Rivory, and F. Abelès, "Temperature dependence of the dielectric function of silicon using in situ spectroscopic ellipsometry," *Thin Solid Films*,

vol. 233, no. 1, pp. 166–170, Oct. 1993. [Online]. Available: https://www.sciencedirect.com/science/article/pii/004060909390082Z

[198] L. Vigderman and E. R. Zubarev, "High-Yield Synthesis of Gold Nanorods with Longitudinal SPR Peak Greater than 1200 nm Using Hydroquinone as a Reducing Agent," *Chemistry of Materials*, vol. 25, no. 8, pp. 1450–1457, Apr. 2013. [Online]. Available: https://doi.org/10.1021/cm303661d

[199] H. Chen, L. Shao, Q. Li, and J. Wang, "Gold nanorods and their plasmonic properties," *Chemical Society Reviews*, vol. 42, no. 7, pp. 2679–2724, Mar. 2013. [Online]. Available: https://pubs.rsc.org/en/content/articlelanding/2013/cs/c2cs35367a

[200] B. Sun, P. Li, S. Yu, X. Huang, and L. Ma, "AgNPs/CuNPs/Bragg-PSi substrate subjected to thermal annealing in high-sensitivity detection on crystal violets and diphenyl phthalate," *RSC Advances*, vol. 15, no. 1, pp. 388–397, 2025. [Online]. Available: https://xlink.rsc.org/?DOI=D4RA04726E

[201] J. Joo, J. F. Cruz, S. Vijayakumar, J. Grondek, and M. J. Sailor, "Photoluminescence: Photoluminescent Porous Si/SiO_2 Core/Shell Nanoparticles Prepared by Borate Oxidation (Adv. Funct. Mater. 36/2014)." [Online]. Available: https://advanced.onlinelibrary.wiley.com/doi/10.1002/adfm.201470240

[202] M. Li, S. K. Cushing, J. Zhang, J. Lankford, Z. P. Aguilar, D. Ma, and N. Wu, "Shape-dependent surface-enhanced Raman scattering in gold–Raman-probe–silica sandwiched nanoparticles for biocompatible applications," *Nanotechnology*, vol. 23, no. 11, p. 115501, Mar. 2012. [Online]. Available: https://doi.org/10.1088/0957-4484/23/11/115501

[203] J. Wang, Z. Jia, and Y. Liu, "Improvement of SERS by the Optical Modulation of Photonic Crystal," *IEEE Sensors Journal*, vol. 19, no. 23, pp. 11 221–11 227, Dec. 2019. [Online]. Available: https://ieeexplore.ieee.org/document/8811573/

[204] J. Wang and Z. Jia, "Metal Nanoparticles/Porous Silicon Microcavity Enhanced Surface Plasmon Resonance Fluorescence for the Detection of DNA," *Sensors*, vol. 18, no. 2, p. 661, Feb. 2018. [Online]. Available: https://www.mdpi.com/1424-8220/18/2/661

[205] M. Škrabić, M. Kosović, M. Gotić, L. Mikac, M. Ivanda, and O. Gamulin, "Near-Infrared Surface-Enhanced Raman Scattering on Silver-Coated Porous Silicon Photonic Crystals," *Nanomaterials*, vol. 9, no. 3, p. 421, Mar. 2019. [Online]. Available: https://www.mdpi.com/2079-4991/9/3/421

[206] F. Zhong, Z. Wu, J. Guo, and D. Jia, "Porous Silicon Photonic Crystals Coated with Ag Nanoparticles as Efficient Substrates for Detecting Trace Explosives Using SERS," *Nanomaterials*, vol. 8, no. 11, p. 872, Nov. 2018. [Online]. Available: https://www.mdpi.com/2079-4991/8/11/872

[207] X. Yue, H. Li, X. Lv, and J. Tang, "Porous silicon photonic crystal/silver composite produced by microwave-assisted reduction: Applications to surface-enhanced Raman scattering," *Optical Materials: X*, vol. 2, p. 100027, May 2019. [Online]. Available: https://linkinghub.elsevier.com/retrieve/pii/S2590147819300257

[208] M. Ashurov, A. Baranchikov, and S. Klimonsky, "Photonic crystal enhancement of Raman scattering," *Physical Chemistry Chemical Physics*, vol. 22, no. 17, pp. 9630–9636, May 2020. [Online]. Available: https://pubs.rsc.org/en/content/articlelanding/2020/cp/d0cp00781a

[209] L. D. Tuyen, A. C. Liu, C.-C. Huang, P.-C. Tsai, J. H. Lin, C.-W. Wu, L.-K. Chau, T. S. Yang, L. Q. Minh, H.-C. Kan, and C. C. Hsu, "Doubly resonant surface-enhanced Raman scattering on gold nanorod decorated inverse opal photonic crystals," *Optics Express*, vol. 20, no. 28, p. 29266, Dec. 2012. [Online]. Available: https://opg.optica.org/oe/abstract.cfm?uri=oe-20-28-29266

[210] L. D. Palmer, J. L. Brooks, and R. R. Frontiera, "Probing the coupling of butterfly wing photonic crystals to plasmon resonances with surface-enhanced Raman spectroscopy," *Journal of Materials Chemistry C*, vol. 7, no. 44, pp. 13 887–13 895, 2019. [Online]. Available: https://xlink.rsc.org/?DOI=C9TC02629K

[211] M. T. Hoang, H. Bui, T. H. C. Hoang, V. H. Pham, N. T. Loan, L. V. Le, T. B. Pham, C. V. Duc, T. C. Do, T. J. Kim, V. H. Pham, and T. V. Nguyen, "Silver Nanoparticles-Decorated Porous Silicon Microcavity as a High-Performance SERS

Substrate for Ultrasensitive Detection of Trace-Level Molecules," *Nanomaterials*, vol. 15, no. 13, p. 1007, Jun. 2025. [Online]. Available: https://www.mdpi.com/2079-4991/15/13/1007

[212] S. Kumar, M. Kanagawa, K. Namura, T. Fukuoka, and M. Suzuki, "Multilayer thin-film flake dispersion gel for surface-enhanced Raman spectroscopy," *Applied Nanoscience*, vol. 13, no. 1, pp. 155–163, Jan. 2023. [Online]. Available: https://doi.org/10.1007/s13204-020-01562-0

[213] Y. Wang, Z. Xiao, X. Feng, S. Shi, D. Liu, R. Li, F. Jiang, and J. Liu, "Highly sensitive SERS platform using sub-10-nm Ag nanoparticles on GaN distributed Bragg reflector for detecting organic pollutants," *Sensors and Actuators B: Chemical*, vol. 405, p. 135343, Apr. 2024. [Online]. Available: https://www.sciencedirect.com/science/article/pii/S0925400524000728

[214] P. Y. Y. Kan and T. G. Finstad, "One-step etch-through porous silicon membrane with an open cavity and pore size tuning," *physica status solidi (a)*, vol. 203, no. 15, pp. 3743–3747, 2006. [Online]. Available: https://onlinelibrary.wiley.com/doi/abs/10.1002/pssa.200622208

[215] K. K, J. R, V. S, P. P, N. S, and V. S, "Gold nanostars on porous silicon for sensing picric acid, malachite green using SERS," vol. 11869, p. 1186904, Sep. 2021. [Online]. Available: https://www.spiedigitallibrary.org/conference-proceedings-of-spie/11869/1186904/Gold-nanostars-on-porous-silicon-for-sensing-picric-acid-malachite/10.1117/12.2599916.full

[216] "Nathalie Lidgi-Guigui | nathalie." [Online]. Available: https://nlidgi.guigui.fr/en/bio-english/

[217] H. Chen, R. Zhao, X. Bi, N. Shen, X. Mo, Y. Tao, Z. Chen, and J. Ye, "Bacterial identification by metabolite-level interpretable surface-enhanced Raman spectroscopy," *Advanced Photonics*, vol. 7, no. 4, p. 046007, Jun. 2025. [Online]. Available: https://www.spiedigitallibrary.org/journals/advanced-photonics/volume-7/issue-4/046007/Bacterial-identification-by-metabolite-level-interpretable-surface-enhanced-Raman-spectroscopy/10.1117/1.AP.7.4.046007.full

[218] Y. Liu, M. Ji, X. Ren, Z. Dong, T. Wen, Q. Dong, H.-p. Ho, L. Cui, Y. Lu, and G. Wang, "Deep Learning-Assisted Rapid

Bacterial Classification Based on Raman Spectroscopy of Bacteria Lysed by Acoustically Driven Fiber-Tip Vibration," *Advanced Science*, vol. 12, no. 32, p. e07724, 2025. [Online]. Available: https://onlinelibrary.wiley.com/doi/abs/10.1002/advs.202507724

[219] M. Hassoun, I. W.Schie, T. Tolstik, S. E. Stanca, C. Krafft, and J. Popp, "Surface-enhanced Raman spectroscopy of cell lysates mixed with silver nanoparticles for tumor classification," *Beilstein Journal of Nanotechnology*, vol. 8, pp. 1183–1190, Jun. 2017. [Online]. Available: https://pmc.ncbi.nlm.nih.gov/articles/PMC5480329/

Artificial intelligence tools were used during the preparation of this manuscript to assist with language correction, text reformulation, and improvement of readability.